



CHALMERS
UNIVERSITY OF TECHNOLOGY



Application of an Extended Inverse Method for the Determination of Ice-induced Loads on Ships

Master thesis in Nordic Master in Maritime Engineering

Jillian M. Adams

Department of Mechanics and Maritime Sciences
CHALMERS UNIVERSITY OF TECHNOLOGY
Gothenburg, Sweden 2018

MASTER THESIS 2018:63

Application of an Extended Inverse Method for the Determination of Ice-induced Loads on Ships

Jillian M. Adams



CHALMERS
UNIVERSITY OF TECHNOLOGY

Department of Mechanics and Maritime Sciences
Division of Naval Architecture and Ocean Engineering
CHALMERS UNIVERSITY OF TECHNOLOGY
Gothenburg, Sweden 2018

Application of an Extended Inverse Method for the Determination of Ice-induced
Loads on Ships

JILLIAN M. ADAMS

© Jillian M. Adams, 2018.

Supervisor 1: Pentti Kujala, PhD., Aalto University, Finland

Supervisor 2: Ville Valtonen, MSc., Aker Arctic Technology Inc., Finland

Examiner: Per Hogström, PhD., Department of Mechanics and Maritime Sciences

Master's Thesis 2018:63

Department of Mechanics and Maritime Sciences

Division of Naval Architecture and Ocean Engineering

Chalmers University of Technology

SE-412 96 Gothenburg

Telephone +46 31 772 1000

Cover: Icebreaking Multipurpose Emergency and Rescue Vessel *Baltika* during ice
trials © Aker Arctic Technology Oy

Typeset in L^AT_EX

Application of an Extended Inverse Method for the Determination of Ice-induced Loads on Ships

JILLIAN M. ADAMS

Department of Mechanics and Maritime Sciences
Chalmers University of Technology

Abstract

With the opening of more Arctic shipping routes, the motivation to design safe and efficient ice-going ships has increased. Recently, knowledge of ship-ice interactions and the mechanics of icebreaking processes has improved through numerous full-scale studies; however, the understanding of precise ice-induced pressures and load heights requires refinement to improve design methods.

This thesis aims to further the development of an inverse engineering method to determine the nature of ice loads experienced by ships. The method uses full-scale strain measurements to estimate local pressures on the ship's structures. The data studied in this thesis was collected on the oblique icebreaker *Baltika* while operating in the Russian Arctic over a two-year period.

The inverse method uses an influence coefficient matrix to relate the measured strain to the input pressure load. Using FEM, strain response functions are fitted at each sensor to generate the terms of the influence coefficient matrix. An optimisation routine is used to solve the inverse force-strain relationship and predict the load patch shape and pressure induced by the ice impact.

The hourly maximum strain measurements are identified and analysed to estimate the applied load and contact area during ice impact events. A general analysis of 250 significant impact events reveals that the applied pressure is on the order of 10-25 MPa and the load height is on the order of 1-3 cm. The detailed analysis of 98 individual impact events demonstrates that the load height during impact remains markedly constant for the duration of the contact. Furthermore, the pressure distribution between load carrying structures is investigated. Based on the results, the pressure distribution between structural members is random and independent of the supporting structure.

Keywords: ship-ice interaction, ice-induced load, inverse method, full-scale strain measurements, icebreaker, Arctic

Preface and Acknowledgements

This thesis work can be seen as the culmination of 7 years of engineering education across four countries. While it is based in the field of ship design, it required fundamental knowledge in structural engineering, mathematics, ice mechanics and programming. It was always a challenge and it was always interesting.

This thesis was completed in partnership with Aker Arctic Technology Inc. and was sponsored by them through the Foundation for Aalto University Science and Technology.

It is not possible to acknowledge on a single page the numerous people who have impacted my life in a way that put me on the path that resulted in this thesis. I would, however, like to express my gratitude and appreciation to the following people:

To my examiners, Pentti Kujala and Per Hogström, thank you for your guidance, knowledge and patience. The discussions and advice were integral to the completion of this work.

To Ville Valtonen, thank you for the advice throughout the entire process of my thesis. You constantly encouraged me to dig further into the data and the method to better the science surrounding ship-ice interactions.

To my friends in Canada, Finland, Sweden and elsewhere, thank you for listening to me talk endlessly about boats and ice. Thank you for keeping me sane over the past two years.

To my family, your constant support and encouragement made it possible for me to move 6750 km from home to pursue my dreams. Thank you for everything. And to my mum, a special thank you for reading and editing my thesis.



Jillian M. Adams

6 August 2018
Espoo, Finland

Table of Contents

| | |
|--|-----------|
| Abstract | v |
| Preface and Acknowledgements | vii |
| Table of Contents | ix |
| List of Figures | xi |
| List of Tables | xii |
| List of Abbreviations | xiii |
| List of Variables | xiv |
| 1 Introduction | 1 |
| 1.1 Motivation | 1 |
| 1.2 Project Objective | 3 |
| 1.3 Limitations | 3 |
| 2 Background | 5 |
| 2.1 The Inverse Problem | 5 |
| 2.1.1 Regularisation Methods | 5 |
| 2.1.2 Inverse Crime | 7 |
| 2.1.3 Influence Coefficient Matrix | 7 |
| 2.2 Ice Loads on Ships | 8 |
| 2.2.1 Ship-ice Interactions | 8 |
| 2.2.2 Icebreaking Process | 9 |
| 2.2.3 Pressure-Area Curve | 10 |
| 2.2.4 Peak Ice Loads | 11 |
| 2.3 Classification Rules for Ice-going Ships | 15 |
| 2.3.1 Polar Class Rules | 15 |
| 2.3.2 Russian Maritime Register of Shipping Rules | 16 |
| 2.3.3 Finnish-Swedish Ice Class Rules | 17 |
| 2.4 Icebreaker Baltika | 18 |
| 2.4.1 Oblique Angle of Attack | 20 |
| 2.5 Ice Load Measurement (ILM) Systems | 21 |
| 2.5.1 Instrumentation On Board the <i>IB Baltika</i> | 21 |
| 2.5.2 System Functionality Verification | 23 |
| 3 Measurement Data Processing | 25 |
| 3.1 Environmental Study | 25 |
| 3.1.1 Ice Type | 27 |
| 3.2 Strain Measurement Pre-Processing | 27 |
| 3.2.1 Shear Strains | 27 |
| 3.2.2 Normal Strains | 28 |
| 3.3 Event Selection | 30 |
| 4 Methodology | 33 |
| 4.1 Discretisation of the Measurement Area | 34 |
| 4.2 Influence Coefficient Matrix Determination | 37 |
| 4.2.1 System Response Functions | 37 |

| | | |
|----------|---|-----------|
| 4.3 | Finite Element Model | 39 |
| 4.3.1 | Geometry | 40 |
| 4.3.2 | Loads and Boundary Conditions | 40 |
| 4.3.3 | Mesh | 41 |
| 4.4 | Optimisation Algorithm | 43 |
| 4.5 | Method Verification | 45 |
| 4.5.1 | Optimisation Properties and Input | 45 |
| 4.5.2 | Selection of FE Mesh Density | 47 |
| 4.5.3 | Discretisation 1 Trial Loads | 47 |
| 4.5.4 | Discretisation 2 Trial Loads | 48 |
| 5 | Results and Discussion | 51 |
| 5.1 | General Event Analysis | 51 |
| 5.1.1 | Load Location Distribution | 52 |
| 5.1.2 | Peak Pressure Distribution | 54 |
| 5.1.3 | Load Height Distribution | 54 |
| 5.1.4 | Pressure-Area Curve | 55 |
| 5.2 | Detailed Event Analysis | 56 |
| 5.2.1 | Sample Cases | 57 |
| 5.2.2 | Load Patch Location | 61 |
| 5.2.3 | Load Height | 61 |
| 5.2.4 | Pressure Development | 62 |
| 5.2.5 | Line Load | 62 |
| 5.3 | Load Bearing Structures | 64 |
| 6 | Conclusions | 67 |
| 7 | Recommendations | 69 |
| | References | 71 |
| | Appendix 1: Method Verification Trial Cases | |
| | Appendix 2: Additional Sample Loading Events | |
| | Appendix 3: Additional Line Load Comparisons | |

List of Figures

| | | |
|--------------|--|----|
| Figure 2.1: | Visual representation of forward and inverse engineering problems | 5 |
| Figure 2.2: | ICM procedure using FEM | 8 |
| Figure 2.3: | Stochastic nature of ice loads measured on a structural frame . . | 9 |
| Figure 2.4: | Idealised icebreaking process by shear and bending failure | 9 |
| Figure 2.5: | Stages of the icebreaking process | 10 |
| Figure 2.6: | Local pressure design curve | 11 |
| Figure 2.7: | Peak ice loads identified through the Rayleigh Separation method | 12 |
| Figure 2.8: | Maximum pressures identified by the Event Maximum method . . | 12 |
| Figure 2.9: | Comparison of probability distributions of extreme ice loads . . . | 14 |
| Figure 2.10: | Example Gumbel I probability distribution functions | 14 |
| Figure 2.11: | Historical development of ice load design heights | 18 |
| Figure 2.12: | FSICR pressure distribution between plates and transverse frames | 18 |
| Figure 2.13: | The icebreaking Multipurpose Emergency and Rescue Vessel <i>Baltika</i> | 19 |
| Figure 2.14: | Plan view of the <i>IB Baltika</i> | 19 |
| Figure 2.15: | Section view of instrumented area | 20 |
| Figure 2.16: | Definition of the oblique angle, α | 20 |
| Figure 2.17: | Position and names of strain gauges | 22 |
| Figure 3.1: | Route history of <i>IB Baltika</i> between May 2015 and May 2017 . . | 26 |
| Figure 3.2: | Sample ice chart from 14 February 2017 | 26 |
| Figure 3.3: | Time history of hourly maximum shear differences for FR13_14 . | 28 |
| Figure 3.4: | Sample raw time histories of normal strain measurements | 29 |
| Figure 3.5: | Normal strain adjustment on sensor PL7 for December 2016 . . . | 30 |
| Figure 4.1: | Flow chart of the ice-induced load determination process | 33 |
| Figure 4.2: | Discretisation 1 plan | 35 |
| Figure 4.3: | Discretisation 2 plan | 36 |
| Figure 4.4: | Definition of the direction of p_{unit} for varying load heights | 38 |
| Figure 4.5: | Strain response curves for the variable $h_{1,up}$ for the normal strain sensors in the upper plate field | 39 |
| Figure 4.6: | Full geometry used in the FE model | 40 |
| Figure 4.7: | Rigid boundary conditions and a sample load of the FE model . . | 41 |
| Figure 4.8: | Comparison of mesh densities | 42 |
| Figure 4.9: | Shear strain response between sensors FR13 and FR14 for varying mesh densities | 43 |
| Figure 4.10: | Normal strain response at sensor PL5 for varying mesh densities . | 43 |
| Figure 4.11: | Flow chart of the solution process | 44 |
| Figure 5.1: | Distribution of measurement locations of maximum normal strains events for the general analysis | 52 |
| Figure 5.2: | Impact load location distributions | 53 |
| Figure 5.3: | Distribution of peak pressures | 54 |
| Figure 5.4: | Load height at impact distribution | 55 |
| Figure 5.5: | Pressure-area curve for ice-induced loads on the <i>IB Baltika</i> | 55 |

| | |
|--|----|
| Figure 5.6: Distribution of shear strain peaks identified for the detailed event analysis | 56 |
| Figure 5.7: Distribution of normal strain peaks identified for the detailed event analysis | 57 |
| Figure 5.8: Sample load patches for Loading Event 1 | 58 |
| Figure 5.9: Relevant time histories for Loading Event 1 | 58 |
| Figure 5.10: Sample load patches for Loading Event 9 | 59 |
| Figure 5.11: Relevant time histories for Loading Event 9 | 59 |
| Figure 5.12: Sample load patches for Loading Event 54 | 60 |
| Figure 5.13: Relevant time histories for Loading Event 54 | 60 |
| Figure 5.14: Comparison of line load estimation techniques | 63 |
| Figure 5.15: Distribution of frame/plate pressure ratios | 65 |
| Figure 5.16: Simplified distribution of frame/plate pressure ratios | 65 |

List of Tables

| | |
|--|----|
| Table 2.1: Main particulars of the <i>IB Baltika</i> | 19 |
| Table 2.2: Summary of measurement channel properties | 22 |
| Table 3.1: Ice conditions in the Gulf of Ob between 4 May 2015 and 3 May 2017 | 27 |
| Table 4.1: Global bounds of the discretisation variables | 35 |
| Table 4.2: Summary of the different mesh properties | 42 |
| Table 4.3: Optimisation input and tolerances | 45 |
| Table 4.4: Results of the optimisation properties investigation | 46 |
| Table 4.5: Results of the ICM selection investigation | 47 |
| Table 4.6: Results of selected trial cases for Discretisation 1 | 48 |
| Table 4.7: Results of the optimisation properties investigation for Discretisation 2 | 49 |
| Table 5.1: Details of sample loading events | 57 |
| Table 5.2: Summary of results for the investigation of load bearing structures . | 64 |

List of Abbreviations

| Abbreviation | – | Description |
|--------------|---|---|
| # | – | Frame number |
| AARI | – | State Scientific Center of the Russian Federation: Arctic and Antarctic Research Institute |
| DWL | - | Design Waterline |
| EM | – | Electromagnetic-inductive |
| Fbl | – | From baseline |
| FE | – | Finite Element |
| FEM | – | Finite Element Method |
| FR | – | Frame Shear Strain Sensor |
| FSICR | – | Finnish-Swedish Ice Class Rules |
| IACS | – | International Association of Classification Societies |
| IB | – | Icebreaker |
| ICM | – | Influence Coefficient Matrix |
| ILM | – | Ice Load Measurement |
| KV | – | Norwegian Coast Guard Vessel |
| MT | – | Motor Tanker |
| MV | – | Motor Vessel |
| PC | – | Polar Class |
| PL | – | Plate Normal Strain Sensor |
| PSRV | – | Polar Supply and Research Vessel |
| RMRS | – | Russian Maritime Register of Shipping |
| STR | – | Stringer Shear Strain Sensor |
| SVD | – | Singular Value Decomposition |
| UCR | – | Up-crossing Rate |
| USCGC | – | United Stated Coast Guard Cutter |
| WL | – | Waterline |

List of Variables

| Variable | [Unit] | Description |
|--------------|-------------------|---|
| α | [deg] | Oblique Angle of Attack |
| β_n | [deg] | Frame Normal Angle |
| ϵ | [-] | Strain Vector |
| ϵ_i | [-] | Strain Response at Sensor i |
| θ_C | [deg] | Ship Course |
| θ_H | [deg] | Ship Heading |
| λ | [-] | Tikhonov Regularisation Parameter |
| AR | [-] | Aspect Ratio (PC Rules) |
| a | [m ²] | Area |
| b | [m] | Load Patch Height (PC Rules) |
| CF_c | [-] | Crushing Failure Class Factor (PC Rules) |
| CF_d | [-] | Load Patch Dimension Class Factor (PC Rules) |
| c_a | [-] | Load Length Factor (FSICR) |
| $c_{i,j,k}$ | [-] | Strain Response Curve Coefficients |
| c_d | [-] | Ship Size Factor (FSICR) |
| c_p | [-] | Ship Region Factor (FSICR) |
| D | [tonne] | Displacement |
| F | [MN] | Force |
| $F_{\#59}$ | [kN] | Force on Frame 59 |
| $F_{\#59,5}$ | [kN] | Force on Frame 59.5 |
| \mathbf{f} | [Pa] | Load Vector |
| f_a | [-] | Shape Coefficient (PC Rules) |
| \mathbf{H} | [-] | Weighted Scaling Matrix |
| h | [m] | Load Height (FSICR) |
| h_j | [m] | Load Height for Discretisation Variable j |
| $h_{j,up}$ | [m] | Upper Height Bound for Discretisation Variable j |
| $h_{j,low}$ | [m] | Lower Height Bound for Discretisation Variable j |
| i | [-] | Sensor Number |
| j | [-] | Discretisation Variable Number |
| k | [-] | Upper or Lower Designation |
| l_a | [-] | Load Length (FSICR) |
| m | [-] | Polynomial Order |
| n | [-] | Solution Area Number |
| P | [MPa] | Pressure |
| P_0 | [MPa] | Nominal Ice Pressure (FSICR) |
| P_{avg} | [MPa] | Average Design Pressure (PC Rules) |
| p | [MPa] | Design Pressure (FSICR) |
| \bar{p} | [MPa] | Average Pressure (FSICR) |
| p_n | [MPa] | Applied Pressure in Solution Area n |
| $p_{n,\#59}$ | [MPa] | Applied Pressure on #59 in Solution Area n |
| $p_{n,pl}$ | [MPa] | Applied Pressure on the center plate in Solution Area n |

| Variable | [Unit] | Description |
|----------------|--------|--|
| $p_{n,\#59.5}$ | [MPa] | Applied Pressure on #59.5 in Solution Area n |
| p_{av} | [MPa] | Average Design Pressure (FSICR) |
| p_{fr} | [MPa] | Average Pressure Applied to Frames |
| p_{pl} | [MPa] | Average Pressure Applied to Plate |
| $p_{unit,j}$ | [MPa] | Applied Unit Pressure on Discretisation Variable j |
| PPF | [-] | Peak Pressure Factor (PC Rules) |
| Q | [MN/m] | Line Load (PC Rules) |
| q | [kN/m] | Line Load (FSICR) |
| R | [-] | Pressure Ratio |
| t | [s] | Time |
| t_0 | [s] | Initial Time |
| w | [m] | Load Patch Width (PC Rules) |
| Y | [-] | Global Coordinate Axis |
| y_1 | [-] | Local Coordinate Axis in Solution Area 1 |
| y_2 | [-] | Local Coordinate Axis in Solution Area 2 |
| \mathbf{Z} | [1/Pa] | Influence Coefficient Matrix |
| $Z_{i,j}$ | [1/Pa] | Element of the Influence Coefficient Matrix |

1 Introduction

Ice is a unique material that has fascinated researchers for many years. It is challenging to work with and understand, and becomes even more interesting when considering interactions between the ice and various structures, particularly moving ships.

As the polar ice caps melt and more passages open through Arctic regions, the shipping industry benefits from a reduction in transit times between Europe and Asia [1]. Although there is less ice on the Arctic routes, ships must still be designed to withstand encounters with ice features to be able to take advantage of the new routes. The opening of the polar passages has increased the motivation of the scientific community to gain a better understanding of how ships react to ice-induced loads and how to design more efficient ice-going vessels.

One question that has plagued researchers for many years is the shape of the contact area between an ice floe and the hull during impact. While the line load the structures experience is known with some confidence from the many full-scale measurement programs on ice-going vessels [2], many other parameters are not known with the same level of certainty [3]. There are still many unknowns in the icebreaking process, for example the nature of the load height and the precise ice pressure.

1.1 Motivation

The first purpose-built icebreaking ships were introduced in the Canadian Great Lakes in the mid-19th century to aid merchant ships [3]. As more ships began to operate in ice-infested waters, it became evident that specific rules and regulations were necessary to ensure the safety of the ships and their crews. The first winter navigation rules for ice-going ships were developed in the late 19th century [3]. The early rules were based primarily on damage statistics and outlined the equipment requirements for ships operating in ice-infested waters.

Throughout the 20th century, the rule sets were constantly improved as more damage statistics were collected and as technology advanced [3]. It was evident, however, that to improve designs more information concerning ship-ice interactions and ice-induced loads was required. The study of ice-induced stresses in the hull plating of the icebreaker (IB) *Urho* marked the beginning of modern studies of ship-ice interactions [4].

Since the 1970s, many full-scale studies have been carried out in various locations around the globe to measure the properties of ship-ice interactions [2, 5, 6, 7, 8, 9, 10, 11]. In the Arctic, data collected on the Norwegian *KV Svalbard* provided

insight into the relationship between ice-induced forces measured on the hull and the ice thickness [12]. There have also been studies of ships transiting the Arctic and ramming icebergs in an attempt to understand the maximum ice-induced loads [5, 9, 13, 14, 15]. In Antarctica, strain measurements gathered on the *PSRV S.A. Agulhas II* have been used to study the influence of load length on the magnitude of the load [16] and the effects of the extent of installed instrumentation [17]. The studies have contributed to a better understanding of ship-ice interactions and the icebreaking processes.

The primary use of the results of ship-ice interactions studies is to improve the safety and efficiency of ice-going ships through the development of design and classification rules. As an example, the Finnish-Swedish Ice Class Rules (FSICR) have existed, in some form, since 1890 [3]. Between 1890 and 1965, the most significant change in the FSICR was the introduction of different ice classes for varying ice conditions [3]. Extensive damage surveys in the 1960s, which for the first time gave an indication of the ice-induced pressures on a ship, lead to the publication of 1971 Rules [3]. Further full-scale studies on board ships in the Baltic Sea in the 1970s and 80s lead to the next revision of the FSICR for hull design of ice-going ships in 1985 [3, 18].

One of the most significant changes in the design principles of the 1985 FSICR revision was a reduction of the height of the ice load assumed to be acting on the hull. The change was based on extensive studies on board the Finnish *IB Sisu* [18] and other merchant vessels operating in the Baltic Sea [3]. The load height was reduced from being the same as the ice thickness to being approximately 20-40% of the design ice thickness. Finally, although not implemented in the rules, laboratory tests and full-scale measurements on board *IB Sampo* conducted in the 1990s observed that the ice-contact is more line-like that previously assumed by the 1985 FSICR Revision [19]. Line-like contacts imply more highly concentrated ice-induced loads than assumed in the current rules and could be included in future revisions [3].

Despite the numerous studies of ship-ice interactions, including both laboratory tests and full-scale measurements, the current understanding of ice-induced loads does not stem from first principles. Ice load estimation methods rely heavily on full-scale trials and damage statistics from ice-going ships. However, until the nature of ice is better understood, it is important to continue to gather as much full-scale data as possible from all ice-infested areas and to develop methods to accurately estimate loads based on the collected data.

Of particular interest is the study by Teemu Ikonen published in 2013. He used an inverse method to estimate the ice-induced loads on board *PSRV S.A. Agulhas II* [20]. The measured strain data were used to estimate the magnitude of the ice-induced loads and the load height through inverse engineering and influence coefficient matrices. The results of the study demonstrate that the ice-contacts were line-like; however, the pressure distribution between the plate fields and the frames was not examined.

When the icebreaking multipurpose emergency and rescue vessel *Baltika* was built in 2014, the hull was fitted with strain gauges to measure the strains induced on its asymmetric hull during icebreaking operations. The installed ice load measurement (ILM) system has been continuously recording ice-induced strains since May 2015. The system provides an extensive data set that will, hopefully, enhance the understanding ice-induced loads. Furthermore, the *IB Baltika* has been operating in the Russian Arctic where there are fewer full-scale measurement studies that are publicly available compared to other ice-infested areas.

1.2 Project Objective

The primary objective of this thesis is to further develop an inverse method used to predict the nature of ship-ice interactions. The basic inverse method for the determination of ice-induced loads was developed by T. Ikonen. The aim is to modify the original method to suit the measurement data available for analysis and to estimate the pressure and load patch of the applied load. Furthermore, new pressure variables will be introduced to the discretisation with the aim of allowing more flexibility in the predicted pressure distributions.

The secondary aim is to use the inverse method to study the nature of significant impact events that were recorded by the measurement system on board the *IB Baltika*. Properties of both the individual impact events, such as load development, load height and load location, and the statistical properties of a wider range of peak impacts will be investigated.

1.3 Limitations

The main limitations of this project are:

1. **Confidentiality:** The data collected by the measurement system is confidential and the release of the full data set is undesirable. Only a subsection of representative loads is presented in the final results.
2. **Ice Chart Data:** The lack of on board measurements of ice thickness, ice concentration or ice features is a major challenge. Observations of the prevalent ice conditions are not available for the measurement period, and thus, any knowledge of the ice conditions must be done using ice charts archives.

It is possible to find ice charts for the Russian Arctic; however, they are only published on a weekly basis and do not have sufficient resolution to distinguish specifics, such as thickness or concentration, for the exact position of the ship. A study of the available ice chart data has been conducted, but no attempt has been made to find a relationship between ice conditions and the load predictions.

3. **Regularisation Methods:** The focus of this thesis will not be on regularisation methods used in inverse engineering. The coarse nature of the discretisation pattern is assumed to provide sufficient regularisation. This is further discussed in Section 2.1.
4. **Ship Operations:** Similar to the lack of information concerning the ice conditions, the details of the ship's operations are not known. Some operational data, such as speed and engine power, have been recorded; however, the exact operations, such as level-ice breaking, turning manoeuvres or ramming events, are not known with confidence. Therefore, no conclusions have been drawn to link specific operations with the loading events.
5. **Discretisation Areas:** The discretisation areas are limited to a minimum of 0.05 m from the waterline stringer that divides the span of the instrumentation. The stringer is considerably stiffer than the surrounding frame and plate structures, and therefore, it creates a discontinuity in the strain response of the overall structural system. The discontinuity introduces many mathematical challenges when solving the optimisation algorithm and, at this point, the inverse method is unable to correctly identify the load height and magnitude when the area surrounding the stringer is included in the analysis. Therefore, the area from the waterline stringer to ± 0.05 m has been neglected from the study.

2 Background

The concept of inverse engineering and the methods to solve inverse force determination problems are introduced. Overviews of ship-ice interactions, ice mechanics, peak ice-induced loads and the rules used to design ice-going vessels are given. Finally, the details of the *IB Baltika*, which was instrumented for full-scale strain measurements, are described in this chapter.

2.1 The Inverse Problem

In general, engineering problems can be divided into two types: forward problems and inverse problems. In forward engineering problems, the input and boundary conditions of the system are known and the governing equations are solved to find the system's response. The forward problem governing the force-strain relationship in this study is given in Equation (2.1). The unknown strain, $\boldsymbol{\varepsilon}$, is found by multiplying the known load vector, \boldsymbol{f} , by the known system matrix, \boldsymbol{Z} .

$$\boldsymbol{\varepsilon} = \boldsymbol{Z}\boldsymbol{f} \quad (2.1)$$

In inverse problems, the system's response is known and the inputs to the system must be determined. Only strain data are gathered from the ice load measurement system on board the *IB Baltika*. The strain is the material response to an applied load and, since the load that caused the strain is unknown, the problem is classified as an inverse problem. Figure 2.1 provides a visual representation of the differences between forward and inverse problems.

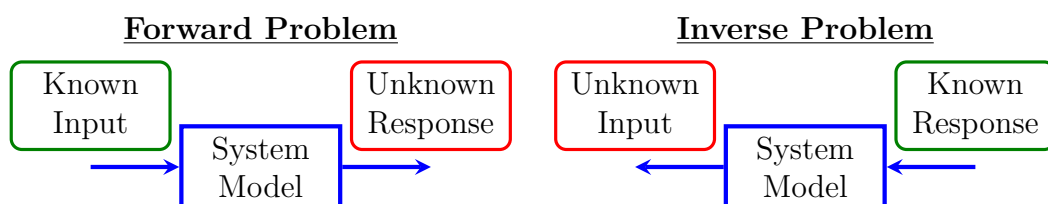


Figure 2.1: Visual representation of forward and inverse engineering problems

2.1.1 Regularisation Methods

One of the most common issues when solving inverse problems is that they are often ill-posed. The problem arises because not all the boundary conditions and initial conditions are known for the system. A well-posed problem is defined as having a

unique solution that exists for all reasonable data and depends continuously on the given data. The issue of ill-posedness is often solved using regularisation methods to transform the problem into a well-posed one. [21]

To transform an ill-posed problem into a well-posed problem various regularisation methods can be used. Uhl describes five regularisation methods that can be used in inverse contact-force determinations [21]:

- Generalised cross-validation,
- Singular value decomposition (SVD),
- Iterative method,
- Data filtering approach, and
- Tikhonov regularisation.

The cross-validation method consists of removing one data point from the set and estimating the system solution using the remaining data points. The methods allows the unknown parameters of the system to be estimated using only the data itself. The error of the estimation can then be calculated by comparing the values of the removed data point, that is considered to be an independent observation, to its value estimated using the other data points [21].

In the SVD method, the system matrix is decomposed using a singular value and singular vector. The stability of the inverse problem solution is improved by removing the parts corresponding to the smallest singular values [20].

Generally, iterative regularisation methods are those which make use of numerical methods designed to solve simple linear matrix equations. While these numerical methods may not have been intended to be used as regularisation methods, they are useful when data signals are corrupted by noise [22].

Data filtering regularisation methods are often using in frequency-domain analysis. In this method, the high frequency contents are filtered out to limit the ill-posedness of the problem as the high frequency components are often the cause of non-unique solutions [21].

Finally, the Tikhonov regularisation is one of the most common and effective methods used to transform ill-posed problems [23]. The inverse method has been previously used in two contact-force determination studies similar to the current study [20, 24]. In the Tikhonov regularisation method, a regularisation parameter and a weighted smoothing matrix are used to minimise the system equation. The Tikhonov regularisation method is presented in its simplified form in Equation (2.2) [25].

$$\operatorname{argmin}_f \{ \|\mathbf{Z}\mathbf{f} - \boldsymbol{\varepsilon}\|^2 + \lambda \|\mathbf{H}\mathbf{f}\|^2 \} \quad (2.2)$$

In Equation (2.2), \mathbf{Z} is the matrix of influence coefficients that describes the effect each input has on the system's output, λ is the regularisation parameter, \mathbf{H} is a smoothing matrix that estimated the relation between the outputs, and $\|\cdot\|$ denotes the Euclidean norm. \mathbf{f} and $\boldsymbol{\varepsilon}$ are the input and output vectors, respectively, which, in this case, correspond to the force and measured strain vectors. The regularisation

parameter, λ , must be selected judiciously since values that are too small will lead to instability in the solution and values that are too large will lead to large errors in the results [25].

2.1.1.1 Discussion of Regularisation Methods

While many studies have been conducted in the area of inverse engineering, the use of regularisation methods in applications of impact force estimation has been questioned [20, 24], particularly for systems with coarse discretisations of the loaded panels. In the study of a line-load determination on rotating rolls, Romppanen concluded that the regularisation techniques increased the error of the norm when compared to simpler inverse equations [24]. Similarly, Ikonen concluded that when using coarse discretisations, the stability of the solution was not compromised when the regularisation was removed [20]. As such, the use of regularisation techniques will not be the focus of this study. Care will be taken to ensure the discretisation of the loaded area is coarse enough to provide the necessary regularisation that will result in a stable solution.

2.1.2 Inverse Crime

An important concept in the field of inverse engineering is inverse crime. The crime occurs during the verification process of the inverse model. It is likely to occur if the numerical data used to verify the model have been generated using the same model utilised to invert the data or if the same discretisation pattern has been used [26]. To avoid committing inverse crime, efforts should be made to verify the inverse method with a separate data set whenever possible.

2.1.3 Influence Coefficient Matrix

As shown in Equation (2.1) and (2.2), force and strain are related by a system matrix, known as the influence coefficient matrix (ICM), \mathbf{Z} . The ICM links the inputs and the outputs of the system. The ICM is similar to the stiffness matrix in finite element methods (FEM); however, the ICM method is more versatile than FEM since it does not require an idealised model which is often necessary for FEM [24]. The ICM can relate any two quantities, regardless of imperfections that might arise from full-scale data.

As described by J.-A. Romppanen [24] and T. Ikonen [20], FEM can be a useful tool in the determination of the ICM elements. The general process is to apply unit loads at strategic locations on the structures and to measure the response at the location of the sensors. The strain responses can then be used as the elements of the i -by- j ICM where i is the number of sensors and j is the number of discretisation variables. Figure 2.2 summarises the work flow.

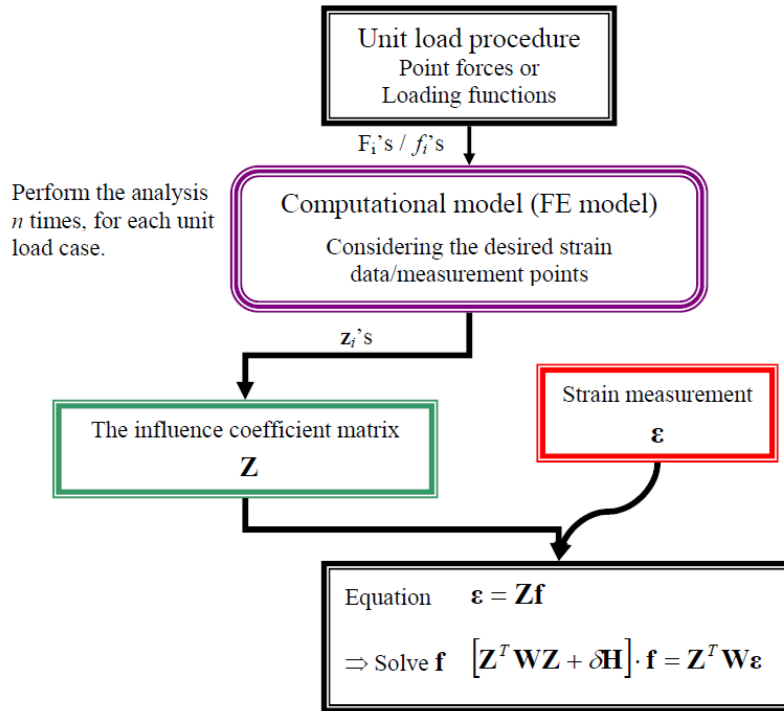


Figure 2.2: ICM procedure using FEM [24]

2.2 Ice Loads on Ships

Sea ice is a particular material in that it is generally found at a temperature relatively close to its melting temperature resulting in unpredictable mechanical properties. Many variables, such as temperature, salinity, and age, can have a large effect on the mechanical properties of the ice, and thus, the resulting loads on the structures the ice interacts with. This thesis work will focus only on ice-induced loads caused by the interaction between ice and mobile objects, such as ships. The study will not consider the interaction between ice and stationary objects, such as bridge pillars.

Many advances in the understanding of ice-induced loads on ships have been possible in recent years as the Arctic passages become more accessible. Of particular interest, is the research concerning design loads, load patch height, and distribution of forces on the hull structures.

2.2.1 Ship-ice Interactions

When a ship encounters an ice feature, a complex interaction between the two objects occurs. The complexity is due to the relative motion of the ship and the ice, the different failure modes of ice and the flow of the ice once it has broken. Some common ship-ice interactions scenarios are:

- Continuous level-ice breaking,
- A ship stuck in compressive ice,
- A ship hitting a thick ice floe straight ahead,

- A ship hitting ice edge at an angle when turning in a channel,
- A ship navigating in brash ice, and
- A ship ramming an ice ridge.

In each scenario, the ice will create an impact load on the ship's hull. The magnitude of the impact will depend on the ice properties, the failure process of the ice and the impact scenario. The result is that ice-induced loads on ships are stochastic in nature [27]. Figure 2.3 provides a sample time history that illustrates the randomness of ice-induced loads over time.

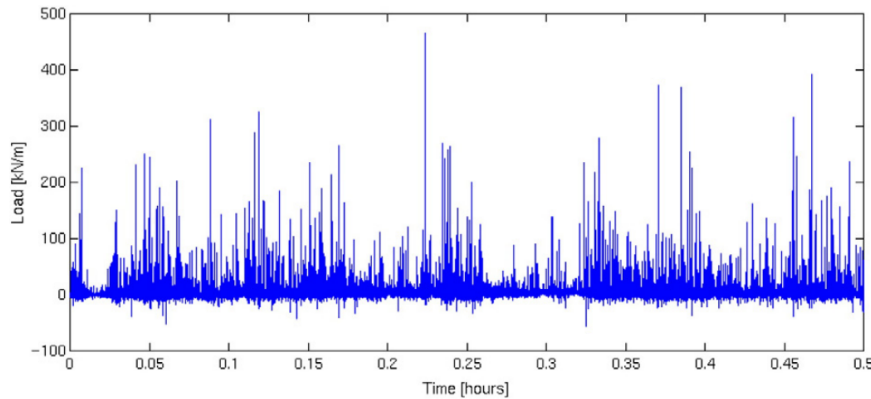


Figure 2.3: Stochastic nature of ice loads measured on a structural frame [28]

2.2.2 Icebreaking Process

There are several stages of the icebreaking process that must be considered. In an idealised breaking process, when a ship first encounters an ice feature, the ice edge begins to fail due to crushing [29]. Crushing failure will continue until the force created by the ship is large enough to break the ice by shearing or bending failure [29]. When the final failure occurs, the ice-induced force is at the maximum. Figure 2.4 provides a sectional view through the thickness of an ice sheet to illustrate the different idealised failure modes of ice. The failure mode is also dependent on the shape of the hull and its normal frame angle, β_n .

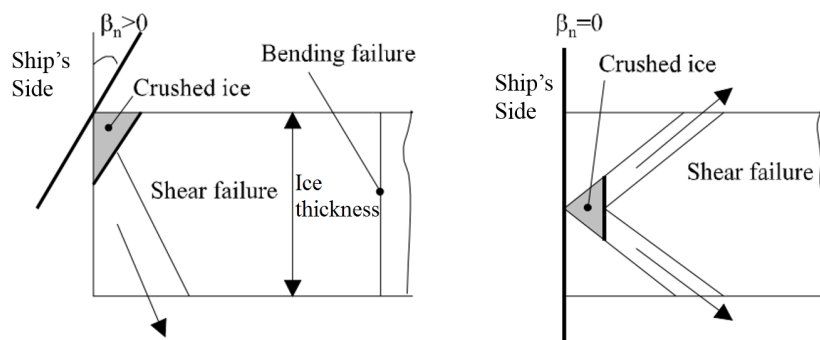


Figure 2.4: Idealised icebreaking process by shear and bending failure [29]

Individual ice-induced loads are almost instantaneous and the duration of the loading event is generally one second or less. Despite the short duration, the individual loads can be divided into three sections: the approaching stage, the crushing stage and the disengaging stage. Figure 2.5 illustrates the increase in force during the approaching and crushing stages until the maximum force occurs when the ice sheet breaks. The maximum load is then followed by a period of decreasing force as the load disengages. All three stages occur in only 0.4 seconds in the example load shown in Figure 2.5.

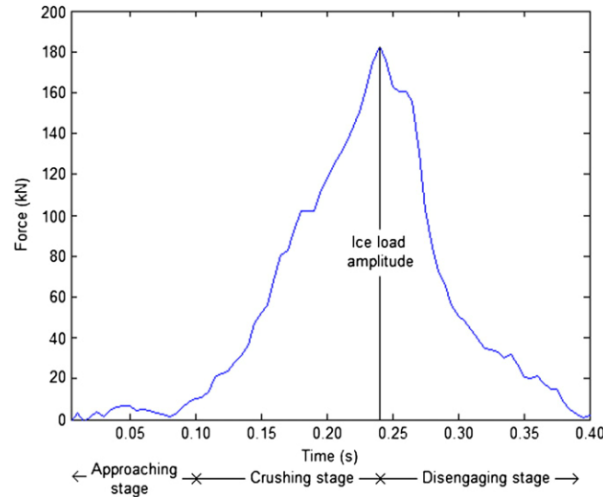


Figure 2.5: Stages of the icebreaking process [30]

2.2.3 Pressure-Area Curve

One well-known tool used in the field of ice mechanics is the pressure-area curve. The curve illustrates the relationship between the ice pressure experienced by a structure and the area over which the pressure acts. One of the initial studies in this area was conducted by T. Sanderson and found a distinct trend of decreasing ice pressure as the contact area between the ice and the structure increased [31]. While the study focused on offshore structures, the same trend has been observed in many studies on board ships [14, 32, 33, 34]. From a study of the pressure measurements gathered on board the *USCGC Polar Sea* and *MV Canmar Kigoriak*, I. J. Jordaan *et al.* proposed a pressure-area curve that could be used when selecting the design pressure for local ship structures [32]. Figure 2.6 presents the design curve.

The design curve is an important tool because it is a simple approach to estimating design loads. With only the knowledge of the layout of structural members and an estimated load height, it is possible to select a design load with which the structures can be dimensioned. While studies of different full-scale pressure estimates have concluded that the design pressure-area curve (Figure 2.6) acts well as an upper boundary for a wide range of measured ice pressures, the pressure-area curves based on varying ice conditions can follow drastically different curves [14, 33, 35, 36]. Relying solely on the design pressure-area curve to select design pressures can often over estimate the design pressure if a ship is operating in lighter ice conditions than ramming icebergs in the high Arctic.

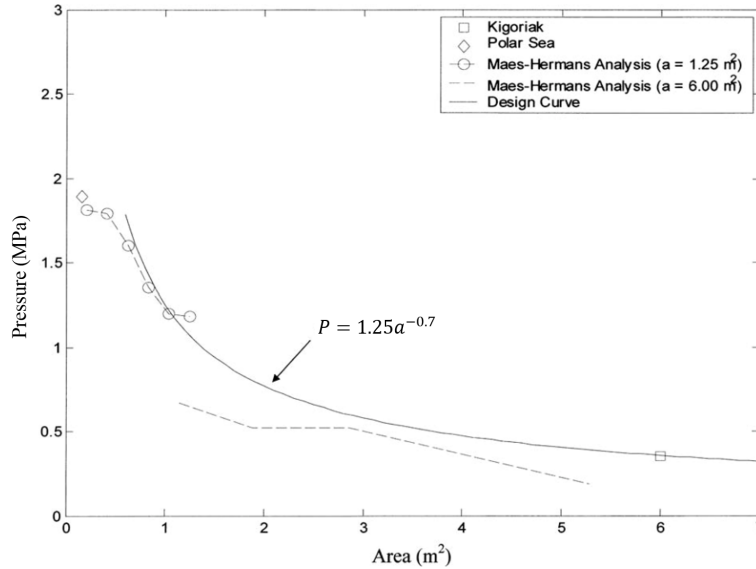


Figure 2.6: Local pressure design curve [32]

2.2.4 Peak Ice Loads

When processing full-scale measurements to determine the history of the ice loads, the unique ice-loading events must be distinguished from the noise of the sensors. Many methods exist to isolate the peak ice loads. The Rayleigh Separation method has been described by Kujala *et al.* in their analysis of ice loads in the Baltic Sea [37]. The Maximum Event method has been used by Ralph *et al.* to determine peak loads during ice ramming events [15, 35]. Finally, the Up-Crossing Rate method, developed by Li *et al.*, identifies peak loads for continuous icebreaking events [15, 34]. Once the ice-induced load peaks are identified, statistical distributions can be fitted to the data to be used in long-term ice-induced load predictions.

2.2.4.1 Rayleigh Separation Method

On the basis of a comparison between ice load measurements over a specified period of time, the Rayleigh Separation method makes use of a threshold value and a separator value to identify the peak ice loads. Figure 2.7 shows a sample time history with the maximum values identified through Rayleigh Separation with a separation value of 0.5.

The threshold value is used to identify the minimum load that is considered to be induced by ice, as opposed to the load induced by open-water waves or system noise [37]. The separator value is used to distinguish between consecutive peaks in the measurement history. It is defined as a percentage of the previous peak's magnitude, below which the signal must fall before the next peak of the load spectrum can be identified. An example of the use of the separation value to identify consecutive peaks can be seen between Peak 3 and 4 in Figure 2.7. The signal drops below 50% of the magnitude of Peak 3 before increasing again to create another peak and, therefore, Peak 4 is considered as a unique peak. In contrast, the large load after Peak 6 is not considered a unique peak since the force only falls to approximately 70%

of the magnitude of Peak 6 before increasing in magnitude again. If a higher load is identified before the signal falls below separation value, it replaces the previous load as the peak load magnitude as seen near Peak 5 in Figure 2.7.

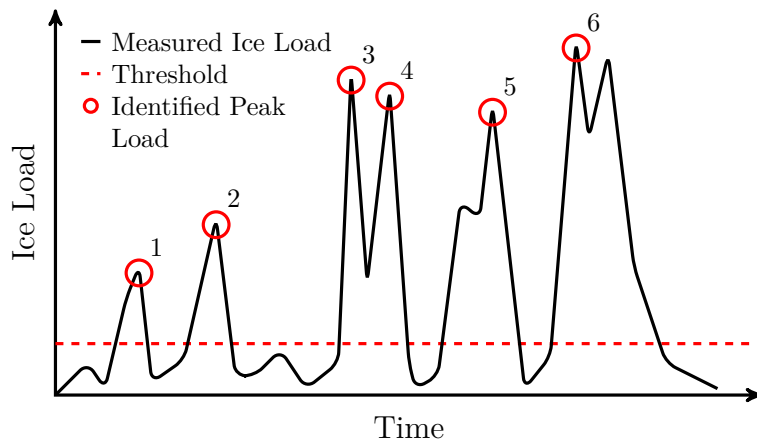


Figure 2.7: Peak ice loads identified through the Rayleigh Separation method [38]

2.2.4.2 Event Maximum Method

The Event Maximum method is used to identify maximum ice-induced loads during discrete ship-ice interactions. The most common definition of an event in this method is the action of a ship ramming into an ice feature where each ram within a series is considered a unique event [14]. For example, this method was used to analyse the data collected during an Arctic expedition where ramming icebergs was the predominant form of ship-ice interaction [35]. Another interpretation of an event is simply a discrete amount of time.

In this method, only the maximum measured load for each event is recorded, regardless of its magnitude relative to other events in the series. The major disadvantage of the event maximum method is that one event might have multiple peaks that are larger than the maximum load of the second event, as illustrated in Figure 2.8 [34]. The secondary peak loads in the first event are lost when implementing the method despite being larger than the load identified for the second event.

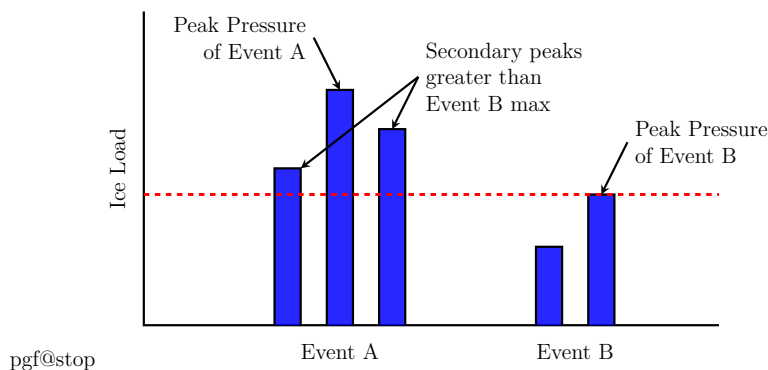


Figure 2.8: Maximum pressures identified by the Event Maximum method [15]

2.2.4.3 Up-Crossing Rate Method

Similar to the Rayleigh Separation method, the Up-crossing Rate (UCR) method for the determination of peak loads records all maxima from the time history. In the UCR method, the maximum ice-induced loads are identified at the points where the signal crosses a threshold value in the upward direction. The number of up-crossings is calculated for varying threshold values. An exponential distribution can be fitted to the resulting distribution of UCRs as a function of the threshold. Finally, the probability of exceeding a given load in a specific time period can be modelled using an exponential distribution [15].

2.2.4.4 Discussion of Peak Identification Methods

Each peak identification method has proven to be useful in the study of ice-induced loads. An important consideration in the selection of the peak identification method is the available data. The Rayleigh method and UCR method are both beneficial when studying continuous interactions while the Event Maximum method is more beneficial when analysing discrete impact events. The Event Maximum method can also be beneficial for finding the peak load in a given time frame.

While the data collected from the *IB Baltika* can be considered as a long continuous interaction between the ship and ice, the length of the measurement period reduces the benefits of using the Rayleigh Separation or UCR methods. Generally, both methods identify considerably more peak events during a given time period than the Event Maximum method. As such, to keep the number of analysis points manageable, the Event Maximum method is used in this study to determine the peak load for each hour during the measurement period. Hourly peaks were chosen to enable the analysis of the entire two-year measurement period while capturing sufficient detail. If further details of a shorter time period, for example an hour, are necessary, the Rayleigh separation method will be used identify the all peak loads during that time frame.

2.2.4.5 Extreme Value Distributions

Due to the stochastic nature of ice loads, the most effective way to describe peak ice-induced loads, or to predict the magnitude of future loads, is to study the statistical properties of the loads. For design purposes, often the statistical study consists of examining the probabilities associated with the extreme values of the measurements. Extreme values follow their own probability distributions that can be estimated either based on the initial probability distribution, if known, or by using approximate methods [39].

For long measurement periods with a large number of recorded ice load peaks, extreme ice loads fit well to probability distributions with exponentially decaying tails. The Weibull distribution [40] and the log-normal distribution [41] can be used to describe extreme ice loads after the careful selection of statistical parameters. Figure 2.9 provides an example of three probability distributions fitted to measured ice-induced loads from a study comparing the effects of load length on maximum loads [16]. The initial probability distribution can only be known with confidence if multi-winter measurements are available; however, the long ice load measurements periods

have only been recorded on a limited number of ships. For shorter measurement periods, approximate methods are used more commonly.

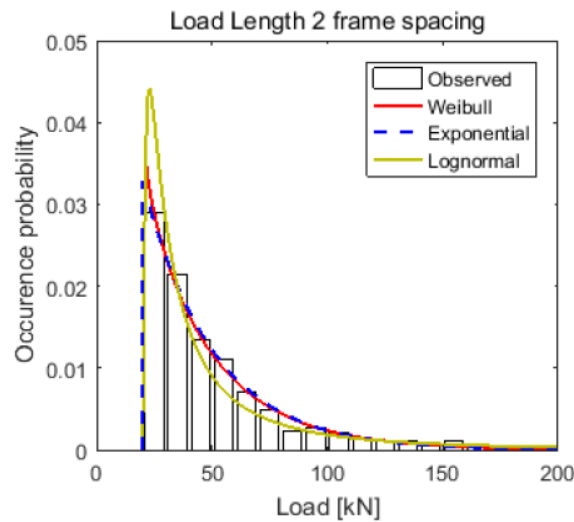


Figure 2.9: Comparison of probability distributions of extreme ice loads [2]

One of the most common approximate methods used in the study of extreme ice loads is the Gumbel I probability distribution [3, 16, 27, 37, 42]. The Gumbel I is an asymptotic distribution that is best suited for fitting a probability distribution to maximum values measured over a repeating time period. For example, it can be used to predict ice pressures on the basis of maximum pressures measured over 1-hour or 12-hour periods [16]. Figure 2.10 presents the general shape of the Gumbel I probability density function.

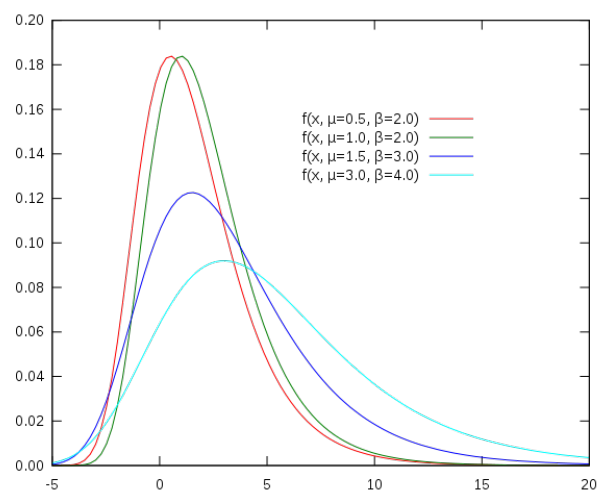


Figure 2.10: Example Gumbel I probability distribution functions [43]

The important link between the different probability functions used to describe extreme ice loads is the exponentially decaying tail of the distributions. The probability of occurrence decreases rapidly as the magnitude of the load increases.

2.3 Classification Rules for Ice-going Ships

In the design of an ice-going vessel, the design load must be carefully selected to ensure the hull is adequately strengthened to avoid excessive damage due to ice impacts. The design load must take into consideration the area of operation of the ship and the corresponding ice conditions, the ship's ice class and the ship's operational profile and practices. Once these variables are known, appropriate design standards can be followed to estimate the magnitude of the design load.

There have been many different rule sets used to design ice-going vessels. Typically, each classification society had their own set of rules by which ships were designed. However, with the publication of the Polar Class (PC) Rules [44] many of the older rules sets have been disregarded in favour of the newer unified rules. As the name implies, these rules were created for ships navigating in the polar waters of the Arctic and Antarctic where they are likely to encounter stronger multi-year ice. In addition to the PC Rules, the Russian Maritime Register of Shipping (RMRS) Rules [45] are also important to consider in this study as they are the rules by which the *IB Baltika* was classified. For ships navigating outside the polar region, the Finnish-Swedish Ice Class Rules [46] are considered to be the best rules to follow when designing merchant vessels for first-year ice conditions which are the ice conditions the *IB Baltika* encounters most frequently.

The following sections will briefly discuss the design principles of the PC Rules, the RMRS Rules and the FSICR.

2.3.1 Polar Class Rules

In 2007, the International Association of Classification Societies' (IACS) Polar Class Rules came into effect. The rules were the result of detailed studies and many years of discussion between many stakeholders [47]. While an attempt was made to be more transparent in the physics corresponding to the rule formulations, many factors used throughout the rules are based entirely on empirical formulas derived from statistics of a limited number of polar vessels [47]. Nonetheless, the PC Rules are now the design standard for ships according to IACS members' rules.

The basic design scenario assumed in the PC rules is a glancing impact between the ship and an ice floe [48]. This scenario was selected from 70 ship-ice interactions and deemed the most damaging of the scenarios that were unavoidable [47]. During a glancing impact, the kinetic energy of the ship is assumed to be spent entirely in crushing the ice it encounters. The energy-based model of ship-ice interaction was derived from the work of Popov *et al.* [49] and Daley [50]. The design point used to define the maximum capacity is based on the formation of plastic hinges [47].

The maximum force for the design scenario is calculated using Equation (2.3), which includes three factors that take into account the ship's shape, fa , crushing factor, CF_c , and displacement, D . The force, F , is then used to calculate both the line load, Q , acting on the hull and the pressure, P , acting on the design patch as shown in Equations (2.4) and (2.5), respectively. Both equations make use of an aspect ratio, AR , which is a function of the ship's hull angles and a load patch factor determined

by the class of the vessel, CF_d . Generally, the design pressure is calculated for the bow area of the ice-going vessel and scaled based on the ships displacement for the midship and stern areas. The area factors were developed from damage statistics [47].

$$F = fa \cdot CF_c \cdot D^{0.64} \quad [\text{MN}] \quad (2.3)$$

$$Q = \frac{F^{0.61} \cdot CF_d}{AR^{0.35}} \quad [\text{MN/m}] \quad (2.4)$$

$$P = F^{0.22} \cdot CF_d^2 \cdot AR^{0.3} \quad [\text{MPa}] \quad (2.5)$$

The load patch height, b , (Equation (2.6)) and width, w , (Equation (2.7)) are calculated using the pressure and line load. The estimated force is assumed to be applied evenly throughout the design patch and the average design pressure, P_{avg} , is calculated. However, within the design patch, there exists areas of higher, concentrated pressure which are acknowledged through the Peak Pressure Factors, PPF , determined from the spacing of the frames.

$$b = Q/P \quad [\text{m}] \quad (2.6)$$

$$w = F/Q \quad [\text{m}] \quad (2.7)$$

$$P_{avg} = F/(b \cdot w) \quad [\text{MPa}] \quad (2.8)$$

One important limitation of the PC Rules is that they do not provide guidance for the design of larger structural members [47]. Structures, such as webframes, stringers, bulkheads and decks, are assumed to be able to carry larger loads than a typical frame to avoid collapse. However, the PC rules do not give clear instructions on the capacity of the larger structures to withstand the load. The capacity calculation for larger structures is advised to be done with "direct calculation" methods [44]. Furthermore, the pressure-area curve indicates that the local pressure acting on these structures should be low due to the increased area of the larger structures [14].

2.3.2 Russian Maritime Register of Shipping Rules

The RMRS Rules are much less transparent than the FSICR or the PC Rules. The exact design scenario used in their development is not clear. The rules rely more heavily on past designs and the designer's experience with past ships [48].

The general design scenario is based on the Kurdyumov and Kheisin hydrodynamic model that was developed through the study of an impact scenario between a ship and an ice floe with rounded edges [51]. The theoretical ice loads are based on

Popov's energy methods where the ship's kinetic energy is spent in the action of crushing the ice [49]. The difference between the ice load estimation methods in the RMRS rules and the PC rules is the inclusion of an intermediate layer of viscous, crushed ice between the hull of the ship and the ice floe.

Another important difference in the RMRS Rules compared to other rules is how they consider the pressure distribution in the load patch. The RMRS Rules assume that the pressure varies over the contact area and the highest pressure is the in the centre of the contact area [51].

2.3.3 Finnish-Swedish Ice Class Rules

The design point in the FSICR is an impact event where the ship collides with a channel edge in the worst design ice conditions [3]. The nominal ice pressure is assumed to be constant regardless of the ship's ice class since the ice conditions are relatively constant in the Baltic Sea in comparison to multi-year ice encountered in the polar regions. The ice thickness and load patch height, however, vary proportionally according to the design ice thickness of the ice class [46]. Equation (2.9) is used to calculate the design pressure of the vessel, and takes into account the ship's size, c_d , the region of the ship, c_p , the load length based on the spacing of the structural element under consideration, c_a , and a nominal ice pressure of 5.6 MPa, P_0 . The three constants are used to reduce the nominal pressure.

$$p = c_d \cdot c_p \cdot c_a \cdot p_0 \quad [\text{MPa}] \quad (2.9)$$

$$q = p \cdot h \quad [\text{kN/m}] \quad (2.10)$$

The design line-load used to dimension the scantlings is estimated by multiplying the design pressure, p , by the load height, h , as seen in Equation (2.10). The design load heights for each class have been reduced since the first publication of the FSICR in 1971. Originally, the load height was assumed to be approximately the same as the ice thickness. In 1985, the FSICR were revised and the load height was reduced to be approximately 20-40% of the maximum ice thickness, corresponding to the centre illustration in Figure 2.11 [3]. The current rules continue to use load patch heights on the order of a 20-40 cm, depending on the ice class.

In the 1990s, laboratory and full-scale tests focusing on the nature of ship-ice contacts were conducted [19]. In both tests, clear panels were installed to directly observe the contact area with the ice. Narrow line-like contacts were observed where pressures of up to 50 MPa occurred [19]. The ship-ice contact observed in these studies is reflect in the illustration from the 1990s in Figure 2.11.

In contrast to the PC Rules, the design point of the FSICR is the yielding of the plate field between frames. The frames are assumed to have more plastic reserve, and thus, can generally withstand higher loads. If a frame fails earlier than a single plate field, more significant damage to the hull of the ship is assumed to occur. Due to the increased flexibility assumed for the plates, the pressure distribution across the plates and the frames is not constant as seen in Figure 2.12. It is assumed that

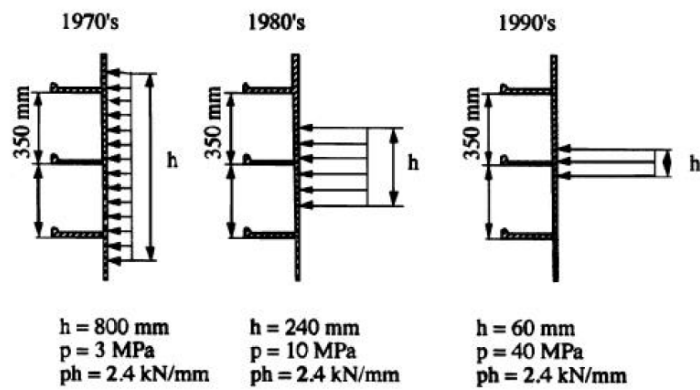


Figure 2.11: Historical development of ice load design heights [52]

the frames will experience a pressure, p , greater than the average pressure, \bar{p} . These assumptions are taken into account in the rules by the incorporation of different safety factors into the equations that govern the design of the plate thicknesses and frame section modulus [3]. There are, however, studies that do not agree with the pressure distribution assumed by the FSICR and instead propose that the pressure is distributed uniformly across the structures [53].

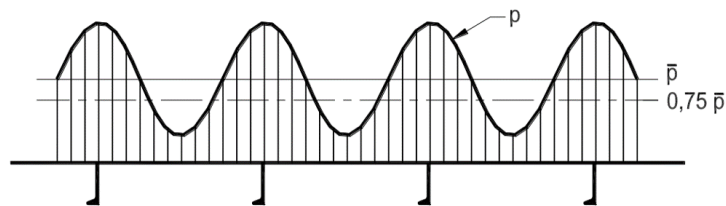


Figure 2.12: FSICR pressure distribution between plates and transverse frames [46]

2.4 Icebreaker Baltika

Built in 2014 to escort vessels much larger than itself, the *IB Baltika* is a rescue vessel with icebreaking capabilities. The ship is unique as it can break ice obliquely, that is, by going sideways instead of forward or backward. The ship was designed by Aker Arctic Technology Inc. and built by Arctech Helsinki Shipyard Inc. The vessel has an asymmetric hull where the port side of the vessel is inclined to break ice sideways. Despite having a beam of 20.5 m, the asymmetric design makes it possible to create a wide channel of approximately 40-50 m in mild ice conditions. The oblique icebreaking allows for more flexibility in the ship's operations compared to traditional icebreakers. The *IB Baltika* is also capable of breaking ice when travelling forward or astern.

The ship is classed as a RMRS Icebreaker 6. The *IB Baltika* is equipped with three 2.5 MW azimuthing thrusters: two in the stern and one in the bow of the ship. The main particulars of the vessel are summarised in Table 2.1 and a photo of the ship is provided in Figure 2.13.



Figure 2.13: The icebreaking Multipurpose Emergency and Rescue Vessel *Baltika* [54]

Table 2.1: Main particulars of the *IB Baltika*

| | | |
|-----------|-----------|------|
| Length | 76.4 | [m] |
| Beam | 20.5 | [m] |
| Draft | 6.3 | [m] |
| Power | 3x2.5 | [MW] |
| Speed | 15.4 | [kn] |
| Ice Class | RMRS IB 6 | [-] |

During the construction of the vessel, strain sensors were installed on the hull structures on the inclined side which is used during oblique icebreaking operations. Figures 2.14 and 2.15 present schematics of the sensor locations relative to directions of travel and waterlines (WL) of the ship, respectively. The measurement system was tested during the ice trials of the vessel in March 2015. Since then, the ILM system has continuously recorded data including, but not limited to, the strain on the hull structures, the speed, and the position of the ship. There are now approximately two years of recorded data available for analysis.

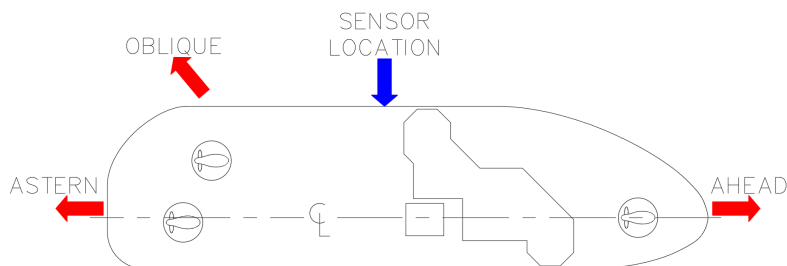


Figure 2.14: Plan view of the *IB Baltika*

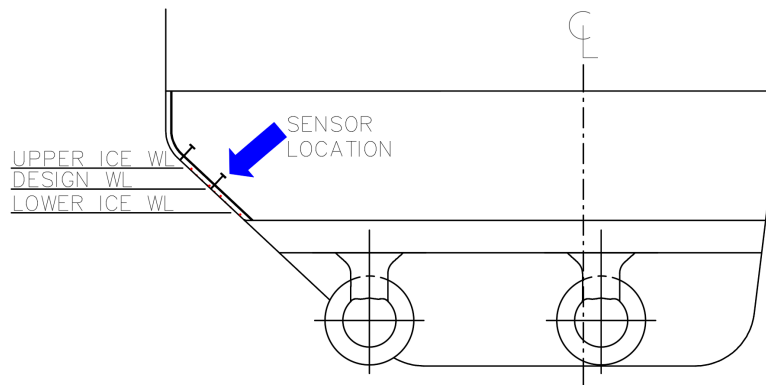


Figure 2.15: Section view of instrumented area

The strain measurements can be used to inversely estimate the ice-induced loads on the hull. Knowledge of ice loads is critical to dimension and to design the structures of an icebreaker.

2.4.1 Oblique Angle of Attack

The oblique angle of attack, α , is defined as the angle between the tail of the heading vector and the head of the course vector, as shown in Figure 2.16. The angle is calculated using Equation (2.11) where θ_C is the course of the ship and θ_H is the heading of the ship. The resulting angle is adjusted if it falls outside of the -180° to 180° range. In this context, positive oblique angles represent when the ship is travelling port-side first and an oblique angle of 0° is when the ship is travelling astern.

$$\alpha = \theta_C - (\theta_H + 180) \quad (2.11)$$

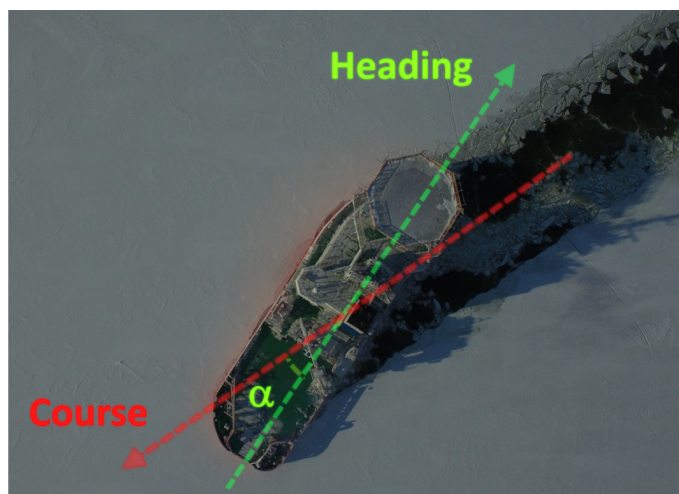


Figure 2.16: Definition of the oblique angle, α

2.5 Ice Load Measurement (ILM) Systems

Many tests have been conducted to gather information about the interactions between ships and ice. While ice tank experiments with model ships can be used to estimate the resistance of the ship in ice, it is difficult to predict ice impact loads on ships from model-scale tests [33]. Full-scale tests, on the other hand, are more expensive to conduct; however, they can provide greater insight into ship-ice interactions.

In typical full-scale tests, several frames in critical locations on the hull are instrumented using strain sensors. The instrumented frames are most often located in the bow, bow shoulder or stern shoulder where ice loads are typically the highest. Some examples of icebreakers and ice-going ships that have been instrumented for research are Finland's *IB Sisu* [41] and *MT Uikku* [37], South-Africa's *PSRV S.A. Agulhas II* [16, 55], and the American *USCGC Polar Sea* [34]. In each of these studies, the ships have been equipped with strain sensors at strategic locations throughout the hull depending on the ship's intended operations. In addition to measuring the hull's response, the ship's operational parameters are measured in these systems and, often, the ice conditions are also measured.

This section details the ice load measurement system on board the *IB Baltika*. The location of the sensors, the data recorded and the limits of the system are described.

2.5.1 Instrumentation On Board the *IB Baltika*

The hull of the *IB Baltika* is instrumented with a total of 22 strain gauges spread between two consecutive frames. The instrumentation is located at midship on the port side and spans a total height of approximately 1.5 m (Figures 2.14 and 2.15). The layout of the sensors is presented in Figure 2.17. "PL" indicates a normal strain sensor located on the hull plating, "FR" is a shear strain sensor on a transverse frame and "STR" is a shear strain sensor located on the waterline stringer. The shear strain data are recorded as the difference between the two strain sensors located on the different frame spans. For example, FR13_14 refers to the shear difference between sensors FR13 and FR14 shown in Figure 2.17. The frame strain sensors are located 44 mm from the shell plating on the bulb side of the frames and the stringer sensors are located 228 mm from the shell plating on the lower side of the stringer. The locations of the shear strain sensors correspond to the neutral axis of the structural members to measure on the shear response.

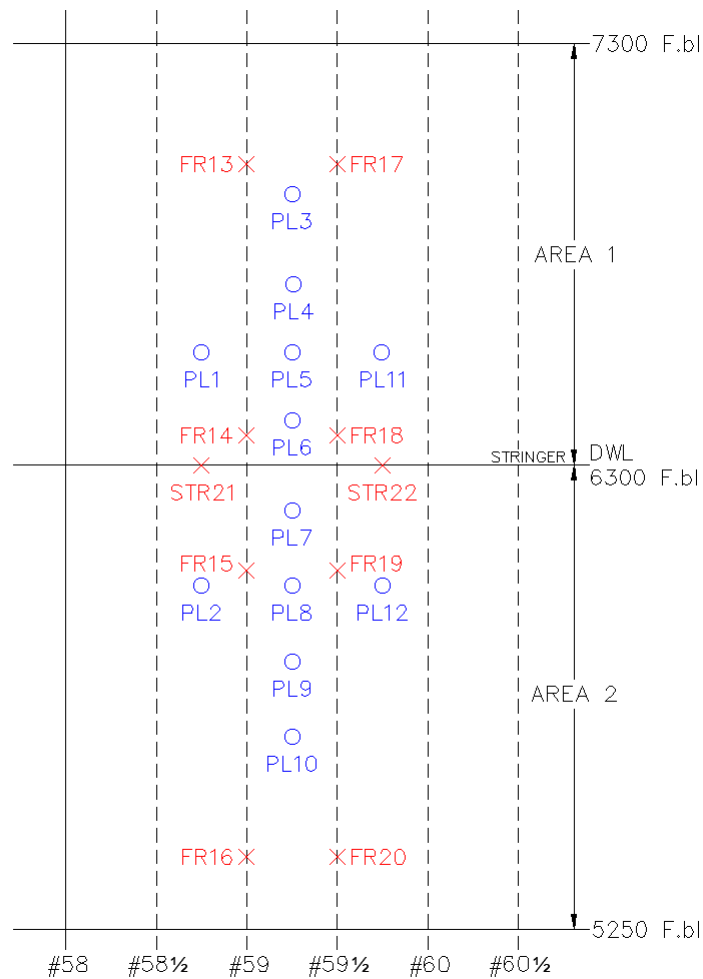


Figure 2.17: Position and names of strain gauges

In addition to the strain measurements, many aspects of the ship's navigational parameters were recorded simultaneously. The speed, power, course, heading, and position are the most important parameters for this project. The units and sampling rates of the various channels are given in Table 2.2.

Table 2.2: Summary of measurement channel properties

| Measurement | Unit | Frequency |
|--------------------|--------------------------|-----------|
| Strain | $[\mu\text{m}/\text{m}]$ | 500 Hz |
| Speed | [kn] | 10 Hz |
| Power | [kW] | 100 Hz |
| Latitude/Longitude | [ddmm] | 10 Hz |
| Course/Heading | [deg] | 10 Hz |

One disadvantage of the ILM system installed on the *IB Baltika* is that it does not record the ice conditions. This is largely due to the inaccuracies or high processing requirements in current automated ice thickness measurement systems and unautomated methods are not practical. One method to estimate ice thickness is by using electromagnetic-inductive (EM) soundings; however, this is typically done on the ice itself or through fly-overs in a helicopter. Both EM sounding techniques are not feasible considering the frequency of strain recordings. The accuracy of an automated EM system suspended from the bow of an icebreaker has been evaluated; however, the system was found not to be as accurate as other methods [56].

Stereo cameras have also been used to automate ice thickness observations. Image processing techniques are used to estimate the ice thickness from pictures taken as ice floes turn during the icebreaking process. Stereo cameras have been used in recent studies of short duration [30]; however, for a multi-year study such as this, the amount of data processing required made the installation of a stereo camera system impractical.

Visual observations were most likely made and recorded in the log books of the ship; however, the log books are not readily available and observations are likely too infrequent to be of any significance.

The lack of precise ice thickness data means that conclusions cannot be drawn between the magnitude of the measured ice loads and the ice conditions as is often done in other studies [37, 42]. The primary source for ice data in this study, which is used to gather a understanding of the general ice conditions, is from the Russian Arctic and Antarctic Research Institute (AARI).

2.5.2 System Functionality Verification

The ILM system on board the *IB Baltika* was verified during the sea and ice trials in the Baltic Sea and the electrical signals were calibrated before delivery of the ship. The calibration of the system was performed external to this study and the information presented here was gathered from the vessel's sea and ice trial reports.

While in open water, the sensor's functionality was evaluated based on a comparison between measurements taken while rolling in waves and while standing still in a calm sea. All sensors responded to the waves and showed varying levels of strain based on their location with respect to the waterline. The sensors closer to the waterline experienced higher levels of strain compared those above or far below the waterline.

In response to the light ice conditions that the ship experienced during the sea trials, the strain sensors recorded peak strains of higher frequency and higher magnitude than compared to open water conditions. The highest magnitude strains were recorded on the lower frames and plate field. The upper sensors were above the ice level.

Finally, during the ice trials in the Russian Arctic, the system was tested under harsher ice conditions than the conditions experienced during the sea trials. The ILM system recorded ice-induced strains throughout the entirety of the ice trial period of varying magnitudes. The results corresponded well to the prevailing con-

ditions at the time. A study of the ice-induced loads during the ice trials indicated that the design load of the vessel had not been surpassed.

Overall, the system is functional and has been recording measurements for two years. There is no indication from the time histories that any bias or errors have been introduced into the system throughout this time.

3 Measurement Data Processing

The aim of this chapter is to detail the environmental conditions experienced by the *IB Baltika* and to present the raw strain measurements. The route of the ship over the two-year measurement period and the general ice conditions in the Gulf of Ob are presented. The raw strain signals and processing methods are detailed and the methods used to select events for analysis are described.

3.1 Environmental Study

Due to the extended measurement period on board the *IB Baltika*, it was impractical to continuously monitor the concurrent ice conditions the ship encountered (Section 2.5.1). There is no available ship-recorded data concerning the ice thickness, concentration or any ice features. Therefore, to understand the ice conditions surrounding the ice loads, archived ice charts must be used. Archived ice charts are not as accurate as recording the conditions at the time of the measurements; however, they can provide some insight into the general ice conditions in the areas of operation.

The primary area of operation for *IB Baltika* is the Kara Sea and the Gulf of Ob as shown in Figure 3.1. During the measurement period, the ship's route can be divided into 5 segments based on location and activity. In the first 3 months, the *IB Baltika* stayed in Murmansk port and only made short, 1-2 day, trips into the immediately surrounding waters. Between August and December 2015, the ship made two return trips from Murmansk to the eastern part of the Kara Sea. The first transit took place between August and September 2015 and lasted approximately 5.5 weeks. On the second return trip from Murmansk between October and December 2015, the *IB Baltika* spent 1 week transiting to the Gulf of Ob, 11 weeks in the Gulf of Ob, and 1 week transiting back to Murmansk. Finally, in January 2016, the ship made a one-way journey to the Gulf of Ob which took approximately 1 week. From mid-January 2016 until May 2017, the ship stayed exclusively in the Gulf of Ob. Of the 727 days of recorded measurements, the ship was in the Gulf of Ob for 551 days.

The main source for ice charts and information in the area of operation is AARI. Their archives include weekly ice charts covering the entire Arctic area as well as higher resolution charts detailing the conditions in Russian waters. An example chart of the ice conditions on February 14, 2017 is provided in Figure 3.2 and similar charts can be obtained for each week of measurement period. Ice data from the Norwegian Meteorological Institute and the National Snow and Ice Data Center were examined as well; however, they did not provide any additional information or higher resolution charts.

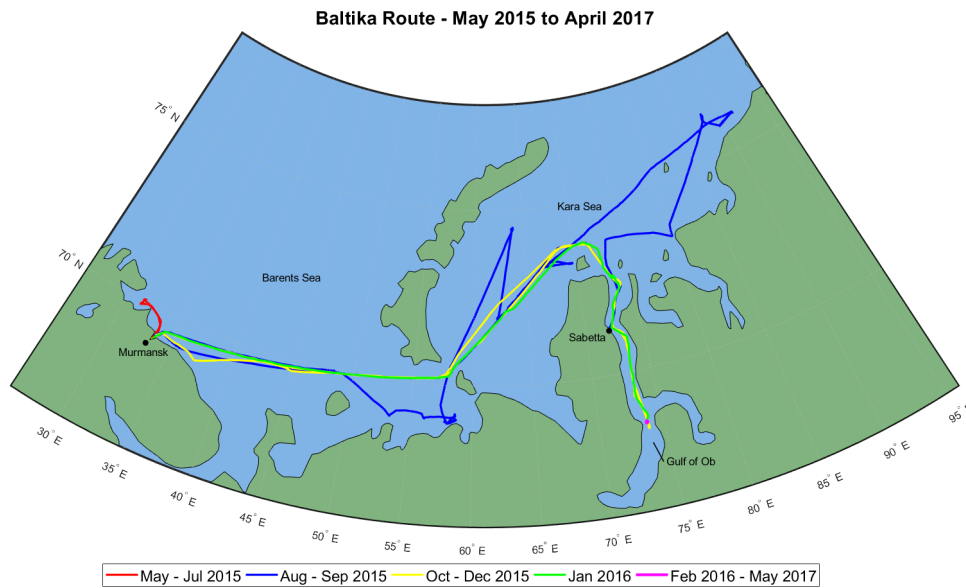


Figure 3.1: Route history of *IB Baltika* between May 2015 and May 2017

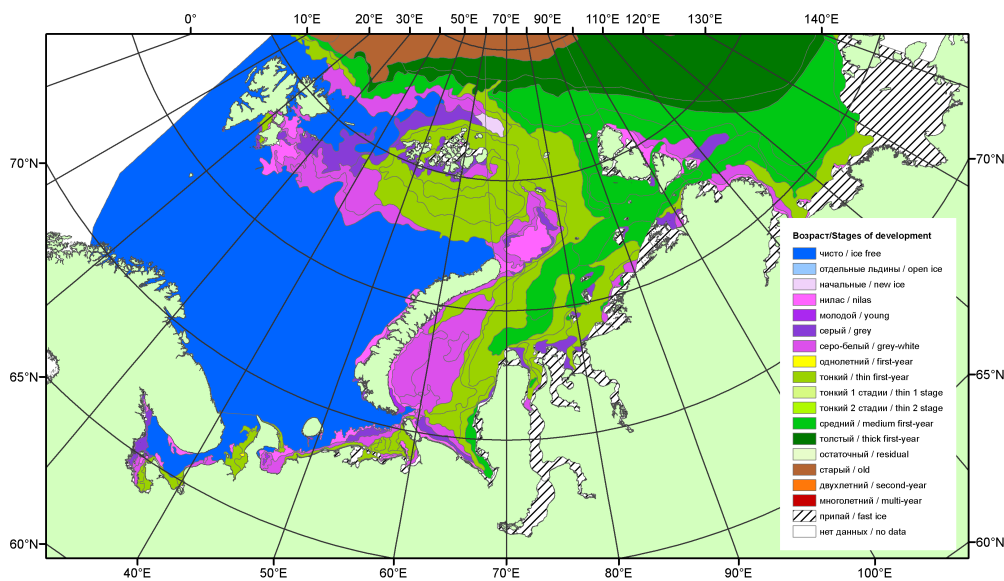


Figure 3.2: Sample ice chart from 14 February 2017 [57]

As can be seen in Figure 3.2, the information is general and ice thicknesses are not specified. During the winter months (1 October to 31 May), the charts show the same details as in Figure 3.2; however, the charts only list concentrations of ice during the summer months (1 June to 30 September). Table 3.1 summarises the general ice conditions in the Gulf of Ob gathered from ice charts published by AARI.

Due to the lack of information available through ice charts, conclusions cannot be drawn concerning the relationship between ice thickness or the activities of the *IB Baltika* and the forces measured on the hull.

Table 3.1: Ice conditions in the Gulf of Ob between 4 May 2015 and 3 May 2017

| Start Date | End Date | Condition |
|------------|------------|--|
| 05.05.2015 | 09.06.2015 | Fast ice or concentration > 9/10 |
| 16.06.2015 | 13.10.2015 | Open water or concentration < 5/10 |
| 20.10.2015 | 17.11.2015 | Formation of new ice |
| 24.11.2015 | 21.06.2016 | Fast ice or concentration > 9/10 |
| 28.06.2016 | 25.10.2016 | Open water or concentration < 5/10 |
| 01.11.2016 | 29.11.2016 | Formation of new ice and thin first-year ice |
| 06.12.2016 | 02.03.2017 | Fast ice or concentration > 9/10 |

3.1.1 Ice Type

After analysing the route history presented in Figure 3.1, it was determined that for the majority of its operations, the *IB Baltika* was located in the Gulf of Ob. The ice charts show that there is no multi-year ice in this area; however, the Gulf of Ob is a body of fresh water which influences the mechanical properties of the first year ice. Generally, fresh water ice is harder and stronger than typical first-year sea water ice due to the lower brine concentration and lower porosity of the ice [58].

Fresh water ice is also generally more brittle than brackish ice which influences the failure mode of the ice during ship-ice interactions. The ice is more likely to fail due to crushing than bending in this case. The general mechanical properties of the ice in the Gulf of Ob are important to the subsequent analysis as they can influence the pressure loads and the load patch shape.

3.2 Strain Measurement Pre-Processing

Before the analysis of ice-induced loads can be performed, the raw data must be pre-processed to extract the unbiased measurements. The full time history must be sorted to identify periods of ice-free conditions, inactivity and high loading events. This section will describe the methods used to process the raw strain data gathered from the shear strain sensors on the frames and the normal strain sensors on the plates of the *IB Baltika*.

3.2.1 Shear Strains

The strain measurements on board the *IB Baltika* were recorded over a two-year period between May 5, 2015 and May 3, 2017. The measured strains were recorded at a frequency of 500 Hz which resulted in approximately 31.5 billion strain data points; however, when looking at the time history of the measurements, it is clear that not all data points contain useful information. There are periods, particularly in the summer months, where the ship did not experience any significant loads. These periods of time should, therefore, be removed from the data set to facilitate

the analysis and reduce computational requirements.

The preliminary parsing of the data was done by finding the maximum shear strain measured for each hour of the two-year measurement period. Figure 3.3 reveals three main periods of where no significant loads were recorded:

1. May to August 2015
2. February to May 2016
3. July to November 2016

An analysis of the operational data collected for these periods showed that the *IB Baltika* was stationary for most of these periods; hence, the lack of significant ice loads, despite often being surrounded by ice according to the ice charts. Due to the lack of significant loads, these periods can be omitted from further analysis. There remains 13 months of measurements to use in the analysis.

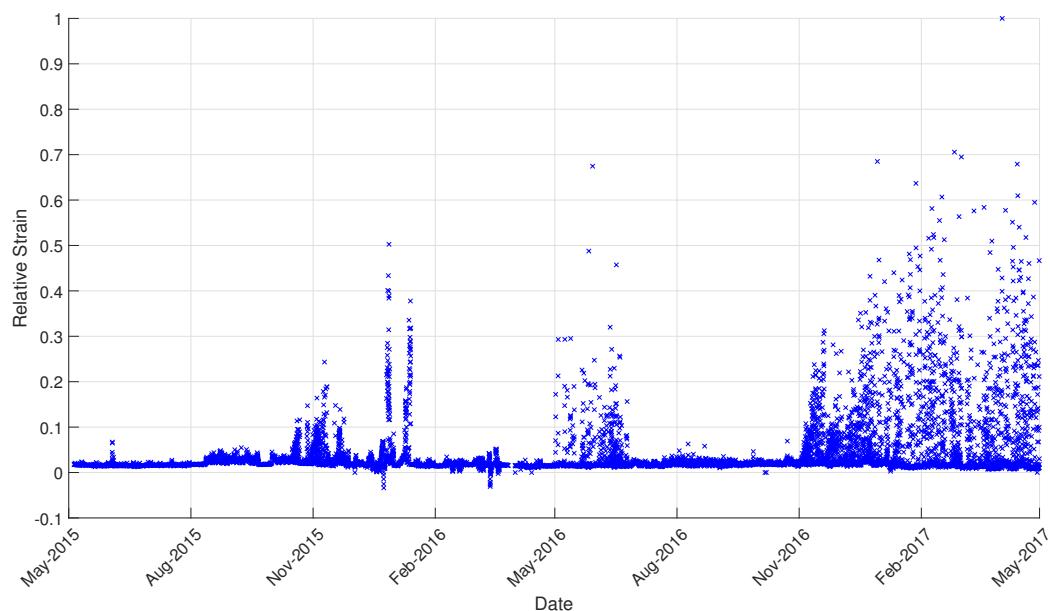


Figure 3.3: Time history of hourly maximum shear differences for FR13_14

3.2.2 Normal Strains

Unlike the shear strain measurements, the normal strain measurements do not measure the strain difference between two sensors. Instead they measure the local normal strain in the longitudinal direction at one location on the plate field. As such when a yielding event occurs in the plate field, the baseline of the normal strain measurement signal will change to reflect the residual strain in the plate due to plastic deformation.

As discussed in Section 2.3, the plate fields of the hull are design to yield before the frames. Therefore, it is expected, and acceptable, that the plates will yield if they experience high loads. Analysis of the full time histories of the normal strain measurements reveals that several small magnitude yielding events occurred during

the measurement period. The yielding events are apparent from the sudden changes in the baseline of the signal as shown in Figure 3.4.

It should be noted that the yielding events evident in the strain history do not indicate a failure of the plate structure, but instead they indicate incidents of small scale plastic deformation. Without conducting a survey of the instrumented area, the exact deformation of the plates cannot be known; however, based on the magnitude of the changes to the baseline normal strain signal, it is assumed that the plastic deformation induced by high loads is small, on the order of a few millimetres. The small scale deformation assumption is confirmed by the uninterrupted functionality of the measurement system. The strain gauges have a maximum elongation of 5% and the limit was not exceeded at any point in the measurement period.

A comparison of the 12 strain signals showed that the signals follow a consistent pattern and only the magnitude of the change in baseline varies from sensor to sensor; therefore, only the strain signals with the largest change in the baseline signals are shown in Figure 3.4.

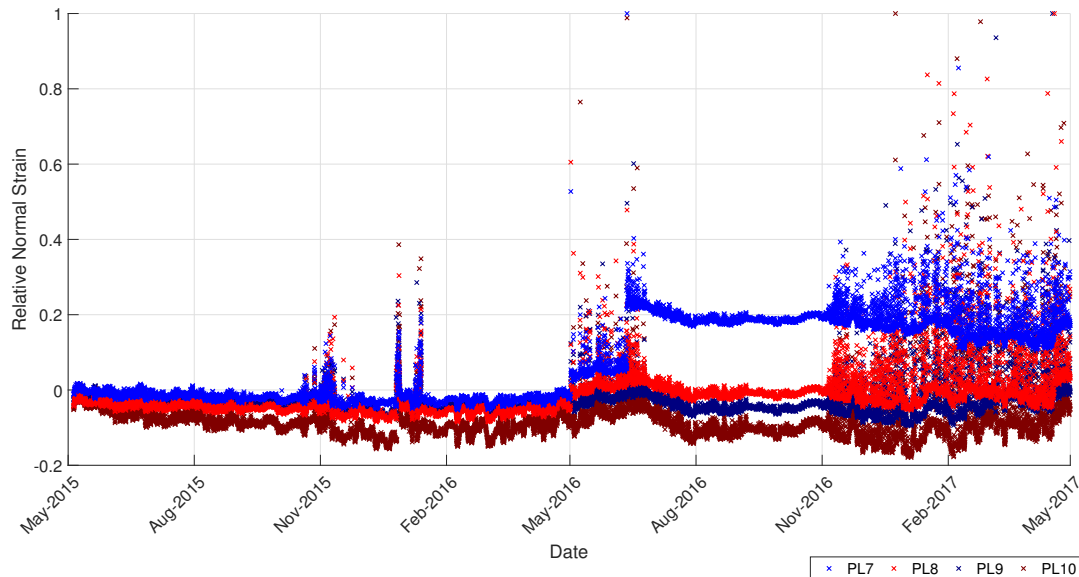


Figure 3.4: Sample raw time histories of normal strain measurements

The most significant change in the measurement signal is in sensor PL7, which is located immediately below the waterline. Figure 3.4 shows two significant changes in the baseline of the normal strain signal for PL7 in May 2016 and June 2016. Sensors PL6 and PL8 have the second highest change in the baseline signal at the same points in time presumably due to their proximity to sensor PL7.

Since the amplitude of the strain signal is desired, the discontinuous baseline must be compensated for and the time history adjusted to have a baseline at $0 \mu\text{strains}$. The baseline of each signal was found using a moving median over a two-week period. The two-week time window proved to capture the baseline signal the most accurately in comparison to one-week time periods, which resulted in a noisy signal, or a one-month time window, which overestimated the baseline significantly. Using

a moving average of the signal did not prove successful due to the largest variation in peak magnitudes.

By subtracting the moving median from the signal, the baseline of the entire signal is shifted to 0 μ strain and the amplitudes of the peaks of the measurement signals can be directly compared. Figure 3.5 presents a comparison between the original strain signal on PL7, the moving median and the adjusted strain signal.

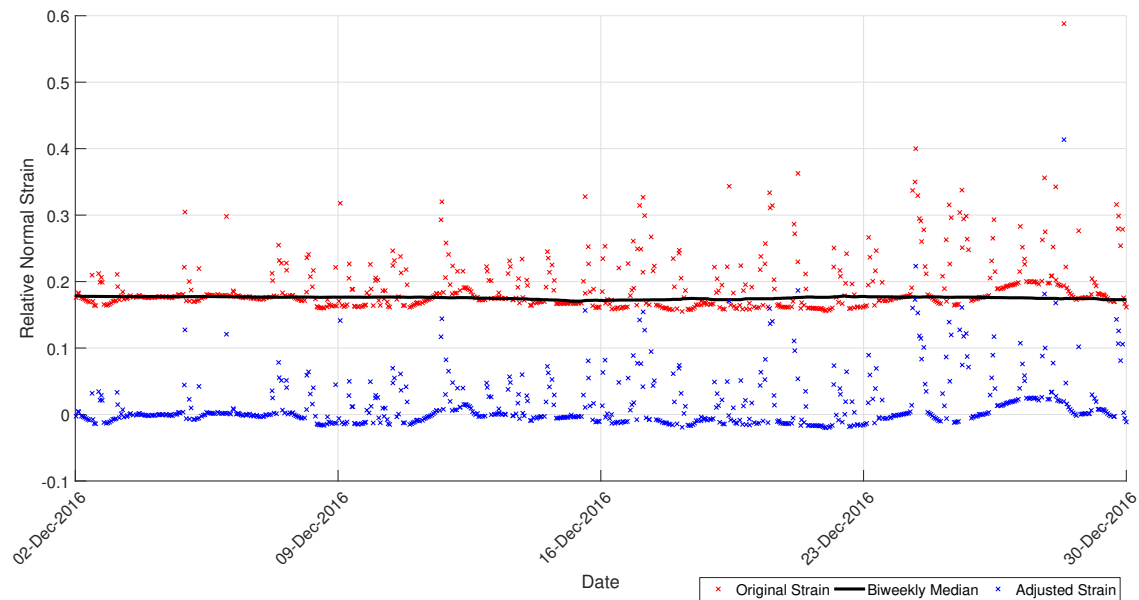


Figure 3.5: Normal strain adjustment on sensor PL7 for December 2016

3.3 Event Selection

To facilitate the analysis of the ice-induced impact events, three representative sets of strain measurements were selected. The instances for analysis were selected based on the magnitude of the maximum hourly strains. The hourly maximum strains were chosen to capture high loading events throughout the entire measurement history.

The measured time histories are filtered at a frequency of 100 Hz from the raw data that was measured at a frequency of 500 Hz. The filtering reduces the computational load significantly while still allowing sufficient measurement points to create a complete picture of the loading event.

For the general analysis, the time instances for analysis were selected from the upper 66% of the hourly maximum strains. Only the measurements from sensors PL3 through PL10 were used because their strain histories matched the best with the occurrences of peak pressures. Including measurements from plate sensors PL1, PL2, PL11 and PL12 results in a large number of loads centred about ± 0.4 m from the waterline stringer. A total of 250 events were identified for the wider strain range. To save on computational time, only a period of 0.1 seconds, centred about the peak strain measurement, was considered for analysis.

In the detailed analysis of individual impact events, all sensors were used in the load identification process. The strain measurements were selected from the upper 50% of the hourly maxima. A total of 52 instances were selected from the shear strain measurements and 50 impact events were selected from the normal strain measurements. A duration of 1 second is used for each instance.

Finally, for the analysis of the load carrying structures, a set of impact events were selected from the most active time period of the *IB Baltika*. To remove bias towards either the plate or the frame sensors, a condition that both instrumented frames experience a peak load within a one-second interval was applied. Simultaneous high magnitude loads on both Frame 59 and 59.5 indicate that the minimum length of the ice-induced load is one frame spacing. Rayleigh separation was used to parse the data collected from 1 January to 31 March 2017 to capture all high magnitude strain events. A total of 168 impact events were identified where both frames were loaded simultaneously during the selected time period.

4 Methodology

The general process to solve for the ice-induced loads using inverse methods follows the methodology developed by T. Ikonen [20]. As described in Section 2.1, the primary inputs to solve the inverse problem are the strain history, $\boldsymbol{\varepsilon}(\mathbf{t})$, and the influence coefficient matrix, \mathbf{Z} . The processing methods for the raw data and the selection of events are described in Chapter 3. This chapter details the methodology used to obtain the ICM and the minimisation algorithm used to solve the inverse problem. Figure 4.1 presents a flow chart of the steps used to determine the ice-induced loads.

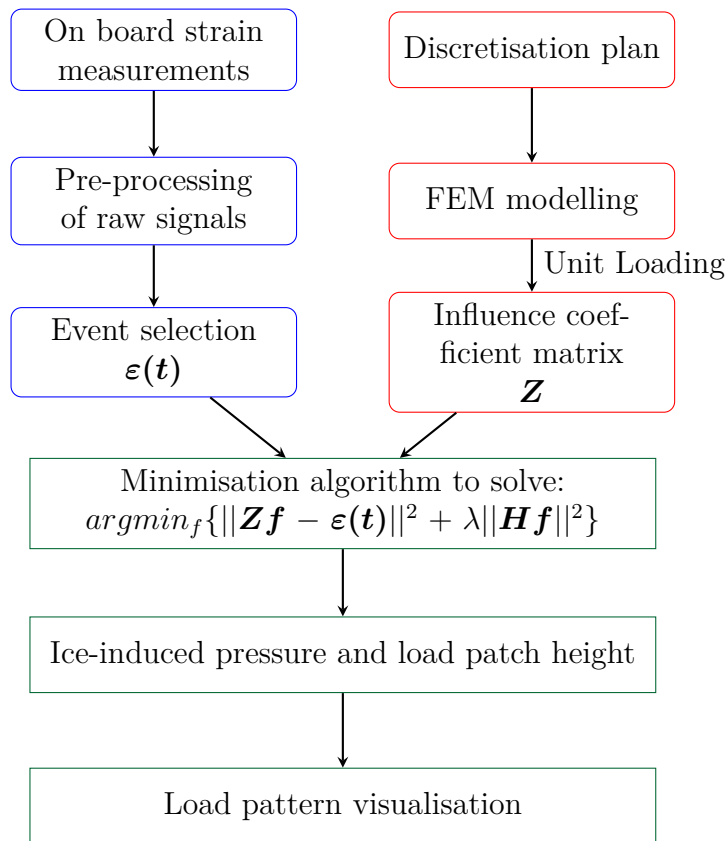


Figure 4.1: Flow chart of the ice-induced load determination process

4.1 Discretisation of the Measurement Area

As shown in Figure 2.17, the instrumented area on the *IB Baltika* is divided by a rigid stringer which is located at the waterline of the vessel. The stringer is approximately halfway between the highest and the lowest normal strain sensors. It is much stiffer than the surrounding frame and plate structures, and therefore, it causes a discontinuity in the strain response of the structural system. As such, the instrumentation area should be divided to minimise the influence of the discontinuity. The division creates two separate solution areas and a small area immediately surrounding the stringer has been neglected from the analysis of the strain measurements.

Three coordinate systems are implemented in the discretisation plan. The global coordinate system, Y , is positioned with the origin in line with the waterline stringer. The global y-axis is the primary reference point for the results of the investigation. The global vertical extent of the solution area is ± 0.95 m from the stringer. Two local coordinate systems, y_1 and y_2 , are used for each of the solution areas. The local coordinates are used during the creation of the influence coefficient matrix. The y-axis of the two local coordinates are positioned at $+0.5$ m and -0.5 m in the global system, respectively. The x-axis of all coordinate systems follows the framing system of the ship.

Discretisation 1 consists of six discretisation variables: two pressure variables, p_1 and p_2 , and four height variables, $h_{1,up}$, $h_{1,low}$, $h_{2,up}$ and $h_{2,low}$. The final load heights of the contact areas, h_1 and h_2 , are calculated as the difference between the upper and lower height variables for each respective solution area. Figure 4.2 shows the discretisation variables of Discretisation 1 in relation to the ship's structures and the solution area boundaries.

Discretisation 2 was created to investigate the pressure distribution between the frames and the plates as suggested by Figure 2.12. The horizontal extent of the solution areas is divided into three equal parts 0.1 m wide; thus creating six pressure variables, $p_{1,\#59}$, $p_{1,pl}$, $p_{1,\#59.5}$, $p_{2,\#59}$, $p_{2,pl}$ and $p_{2,\#59.5}$, as shown in Figure 4.3. The load height is assumed to be constant between the two frames, and since the load height is found in Discretisation 1, the load height from Discretisation 1 is used as input for Discretisation 2. This assumption helps reduce the computational requirements to solve the second discretisation pattern.

To efficiently identify the ice loads using the inverse method, boundaries must be applied to the discretisation areas. The horizontal bounds of all solution areas falls between Frame 59 and 59.5. In Solution Area 1, the vertical bounds, in the global coordinate system, are $+0.05$ m and $+0.95$ m. The vertical bounds are then create the bounds of the height variables. Similarly, in Solution Area 2, the height variables are limited to the area between -0.05 m and -0.95 m in the global system. The interior boundaries located at ± 0.05 m are used to limit the influence of the response discontinuity created by the stringer. The pressure variables are limited between 0 MPa and 50 MPa since all variables must be bounded in the optimisation process. Table 4.1 summarises the bounds of the discretisation variables in the global coordinate system.

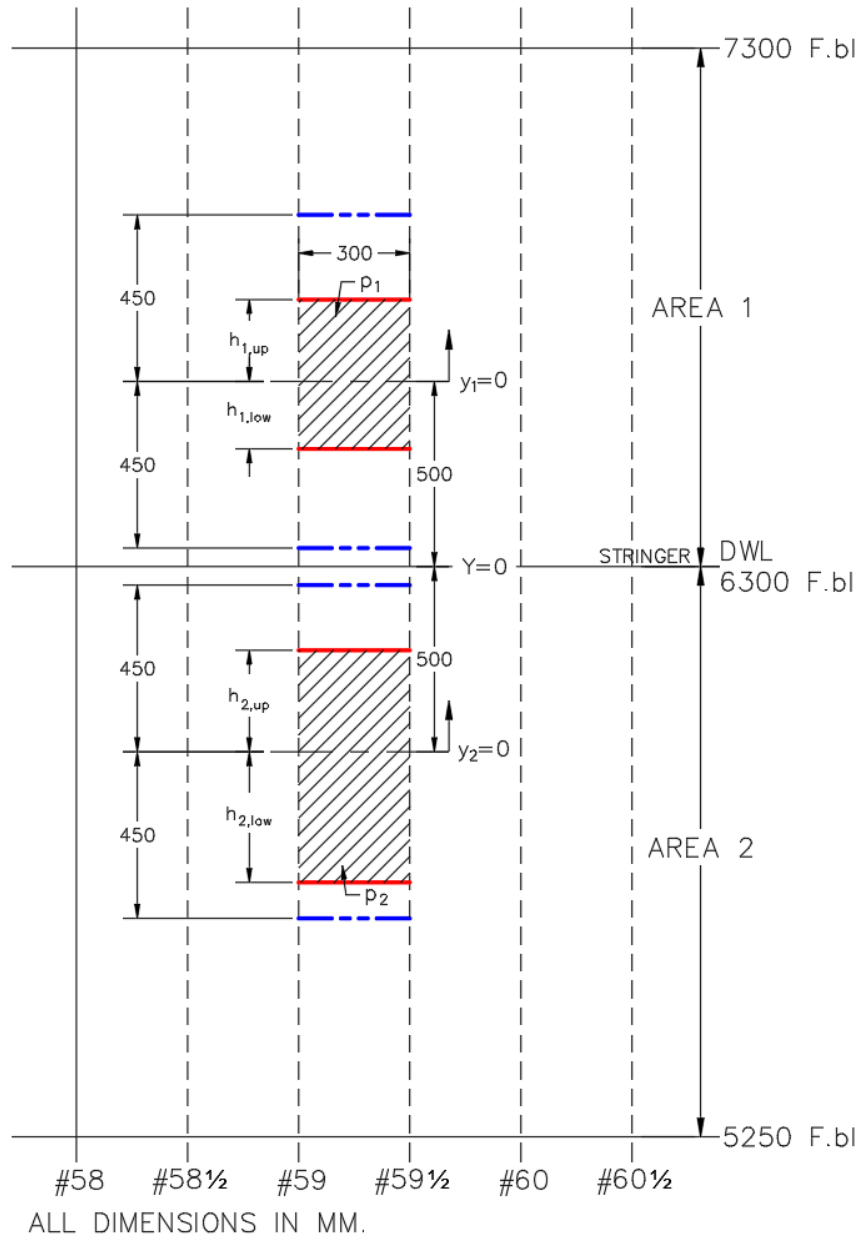


Figure 4.2: Discretisation 1 plan

Table 4.1: Global bounds of the discretisation variables

| Variable | Lower Bound | Upper Bound | Unit |
|---|-------------|-------------|------|
| $h_{1,up}, h_{1,low}$ | +0.05 | +0.95 | m |
| $h_{2,up}, h_{2,low}$ | -0.95 | -0.05 | m |
| $p_n, p_{n,\#59}, p_{n,pl}, p_{n,\#59.5}$ | 0 | 50 | MPa |

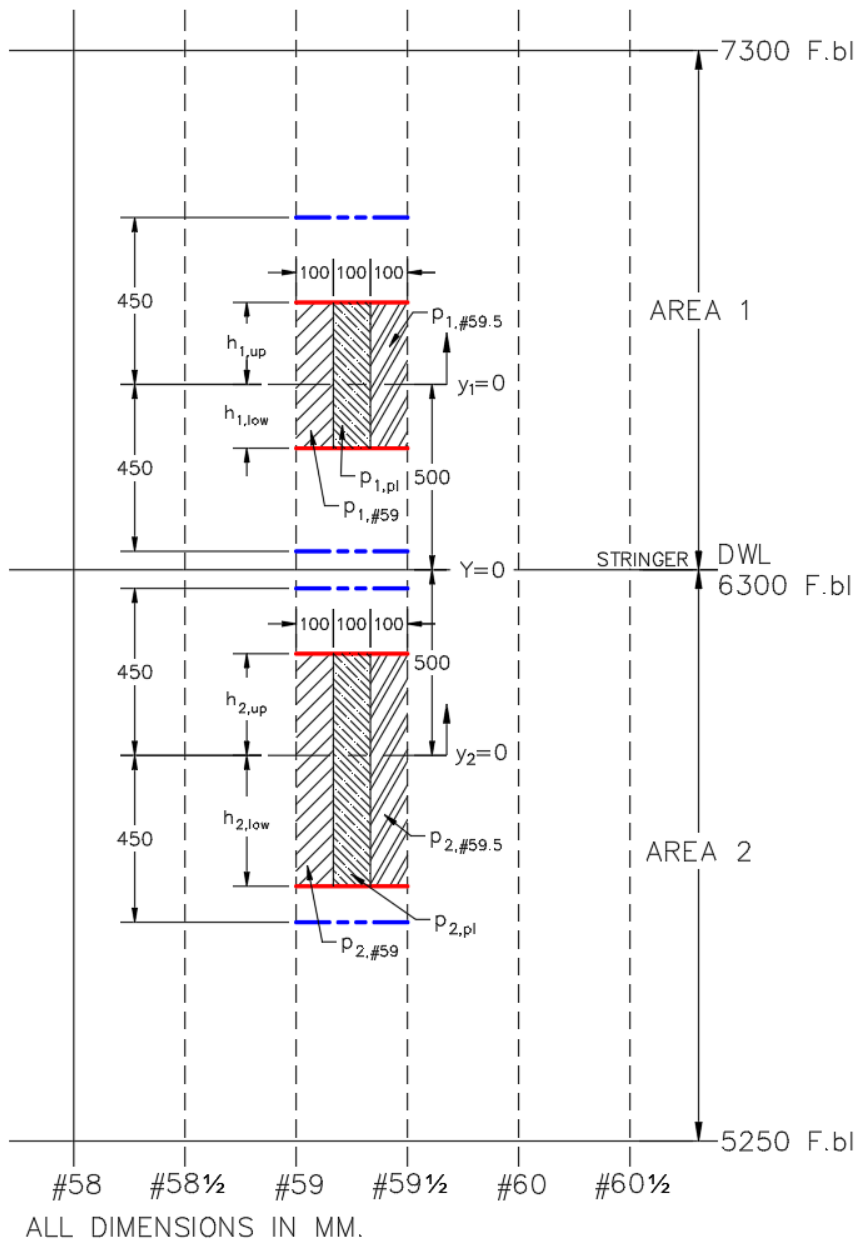


Figure 4.3: Discretisation 2 plan

4.2 Influence Coefficient Matrix Determination

As mentioned in Section 2.1.3, the ICM is used to relate the input and the output of the system. The elements of this matrix are determined by measuring the system's response to a known input. In this study, a finite element (FE) model is used to estimate the strain response at the sensor locations when a unit pressure load is applied to the structure in various locations. The FE model is described in more detail in Section 4.3. This section describes the methodology for the determination of the ICM coefficients.

In a discretisation pattern where the load height associated with a given pressure variable is known and constant, the elements of the ICM are found using Equation (4.1) where $Z_{i,j}$ is the response at the i th sensor to a unit pressure load on the j th discretisation area. However, when allowing the load height to vary, the each element of the ICM then become a function of the load heights, h_j . Therefore, a function describing the strain response of the system at each sensor to unit pressure loads of varying height must be found.

$$Z_{i,j} = \frac{\varepsilon_i}{p_{unit,j}} \quad (4.1)$$

4.2.1 System Response Functions

For the discretisation patterns shown in Figures 4.2 and 4.3, the strain response of the system is a function of the varying load heights associated with the applied pressure. To determine the elements for the ICM, unit loads are applied to the measurement area with increasing height from the centre of the two respective solution areas. The strain is measured at each sensor for each load height and a polynomial curve of order m is fitted to the measured response for each sensor. Equation (4.2) describes the polynomial relationship used for each element of the ICM, $Z_{i,j}(h_{j,k})$ where c is the polynomial coefficient, i is the sensor number, j is the discretisation variable number and k is either the upper or lower height boundary.

$$Z_{i,j}(h_{j,k}) = c_{i,0} + c_{i,1}h_{j,k} + c_{i,2}h_{j,k}^2 + \dots + c_{i,m}h_{j,k}^m \quad (4.2)$$

The reference point for the height measurements is the y-axis of the respective local coordinate system. The load height is varied between ± 0.45 m in 0.05 m increments with respect to the local x-axis. One boundary of the load patch is always at the origin of the local coordinate system. Based on the principle of superposition, the response of the system $Z_{i,j}(h_j)$ can be seen as the sum of the strain response functions for the upper and lower height variables as shown in Equation (4.3).

$$Z_{i,j}(h_j) = Z_{i,j}(h_{j,up}) + Z_{i,j}(h_{j,low}) \quad (4.3)$$

A linear inequality constraint must be applied to ensure that the upper height variable is always greater than the lower height variable. The constraint is implemented through the choice of the direction of the unit loads applied to the structures when

determining the strain response. For the upper height variables, the unit pressure is applied in the positive direction when the height variable is positive relative to the local coordinates and in the negative direction, when the load height is negative relative to the local coordinates. For the lower height variable, the unit pressures are applied in the opposite direction. Therefore, when the responses are superimposed, the pressures will oppose each other and only the area bounded by the two height variables will experience a positive pressure acting on the external side of the shell plating. The directions of the unit pressure loads are illustrated in Figure 4.4.

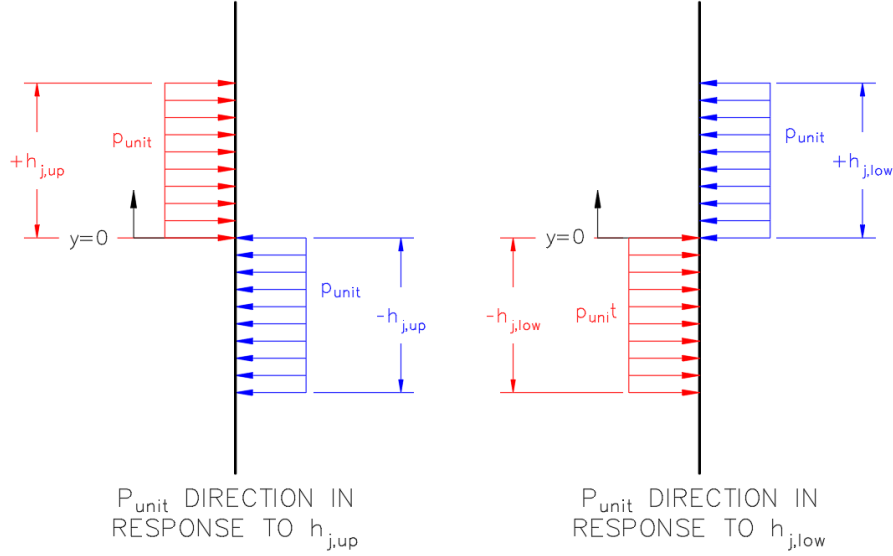


Figure 4.4: Definition of the direction of p_{unit} for varying load heights

The response curves corresponding to the $h_{1,up}$ variable for the normal sensors in Solution Area 1 are shown in Figure 4.5. The curves are 6th order polynomial curves found using Equation (4.2).

The linearity of the FE model makes it possible to simplify the response function and the ICM by combining the equations for the load heights. The linear model implies that the response for $h_{j,up}$ and $h_{j,low}$ are symmetric about x-axis in Figure 4.5 since the only difference between the two variables is the direction of the unit load. The relationship between the responses is explained in Equation (4.4).

$$Z_{i,j}(h_{j,up}) = -Z_{i,j}(h_{j,low}) \quad (4.4)$$

The coefficients of the polynomials used to describe the strain response in Equation (4.2) can, therefore, be factored out and a simplified equation can be used to describe the strain response of the full structure. Equation (4.5) is the factored version of Equation (4.2) and is used to find each element in the $\mathbf{Z}(h)$ matrix. Equation (4.6) shows the matrix representation. The final ICM is found using Equation (4.7).

$$Z_{i,j}(h_{j,up}, h_{j,low}) = c_{i,1}(h_{j,up} - h_{j,low}) + c_{i,2}(h_{j,up}^2 - h_{j,low}^2) + \dots + c_{i,m}(h_{j,up}^m - h_{j,low}^m) \quad (4.5)$$

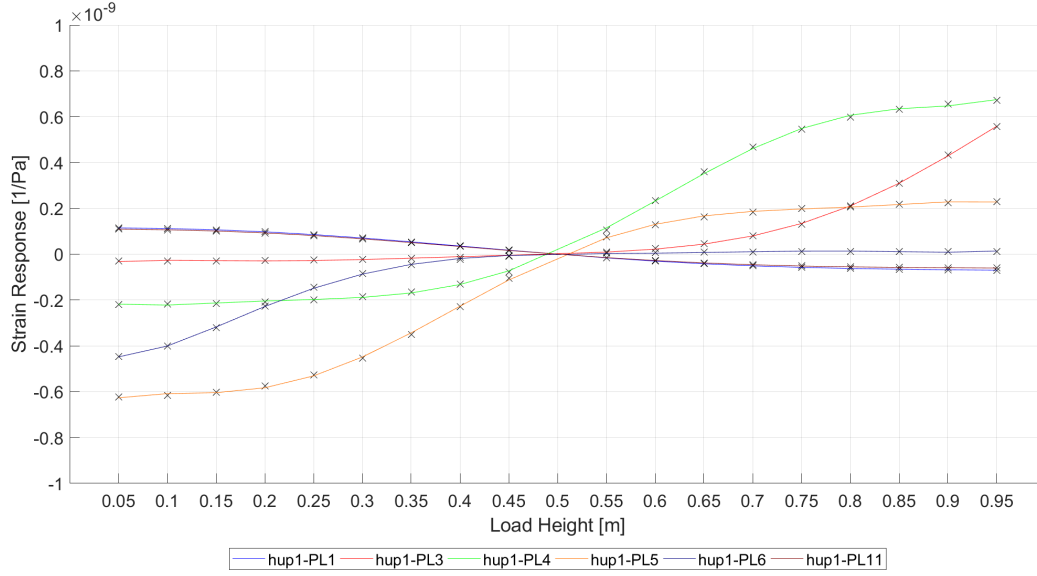


Figure 4.5: Strain response curves for the variable $h_{1,up}$ for the normal strain sensors in the upper plate field

$$Z_{i,j}(h_{j,up}, h_{j,low}) = [c_{i,1} \quad c_{i,2} \quad \cdots \quad c_{i,m}] \begin{Bmatrix} h_{j,up} - h_{j,low} \\ h_{j,up}^2 - h_{j,low}^2 \\ \vdots \\ h_{j,up}^m - h_{j,low}^m \end{Bmatrix} \quad (4.6)$$

$$\mathbf{Z}(h) = \begin{bmatrix} Z_{1,1}(h_{1,up}, h_{1,low}) & Z_{1,2}(h_{2,up}, h_{2,low}) \\ Z_{2,1}(h_{1,up}, h_{1,low}) & Z_{2,2}(h_{2,up}, h_{2,low}) \\ \vdots & \vdots \\ Z_{17,1}(h_{1,up}, h_{1,low}) & Z_{17,2}(h_{2,up}, h_{2,low}) \end{bmatrix} \quad (4.7)$$

The same process is followed to determine the ICM for Discretisation 2. The unit pressures applied in the ICM creation for Discretisation 2 are only applied to the pressure panel in question and not across the full frame spacing. The ICM for Discretisation 2 is a 17x6 matrix.

4.3 Finite Element Model

FEM is used to create the ICM required to estimate the ice loads from the measured strains. FEM is used to apply known loads to the structure and measure the strain response of the structural system. This section will present the FE model geometry, the boundary conditions and loads, and a short mesh independence study. The FE model was created and analysed in ABAQUS [59].

4.3.1 Geometry

The strain sensors are located in a small dry tank at approximately midship on the asymmetric side of the *IB Baltika*'s hull. The tank is bounded on either side by stiff bulkheads at Frame 58 and Frame 62 which create the forward and aft boundaries for the FE model. The stiff boundaries of the tank make it possible to model only a small portion of the ship structures. In the vertical direction, the model is bounded by the main deck at the top and an intermediate deck 4000 mm above the baseline of the ship. These decks are chosen as boundaries since the decks are stiff structures and are at an appropriate distance from the sensors to reduce their influence on the strain response. The tweendeck, shown in the geometry was not chosen since it is only 150 mm from the nearest sensor. In the transverse direction, the model extends from the side shell plating to the inner side plating. The full geometry used in the FE model is presented in Figure 4.6.

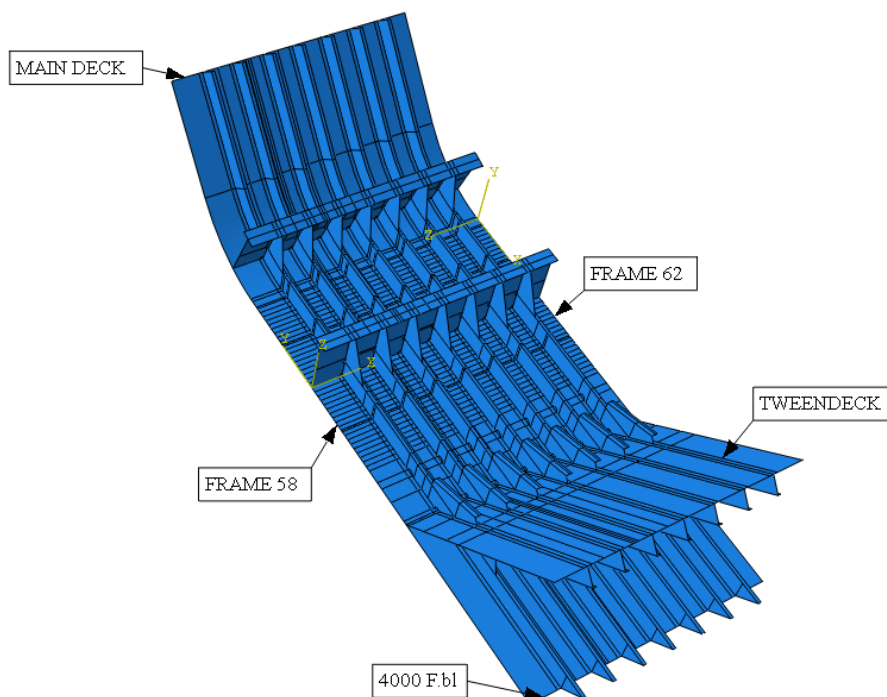


Figure 4.6: Full geometry used in the FE model

The structural stiffeners are modelled such that they are on the inside of the shell plating with the shell plating thickness added to the outer side of the plating. The frames are modelled as "L" shapes with flange thicknesses that match the cross sectional area of the true bulb flats used in construction. The entire geometry is modelled with shell elements.

4.3.2 Loads and Boundary Conditions

Rigid boundary conditions are applied to the edges of the model that are in contact with the bulkheads and decks, including the flanges of the stiffeners. A previous study to evaluate the strain response of the FE model concluded that the change

in response of the model between pinned boundary conditions or rigid boundary conditions was insignificant, and therefore, the model boundaries are at a sufficient distance from the sensor locations to minimise their influence [60].

Due to the limited number of instrumented frames and the resulting uncertainty of the load length, only the space between Frame 59 and Frame 59.5 was loaded to find the strain response curves. An example of one of the applied units loads and the boundary conditions is shown in Figure 4.7.

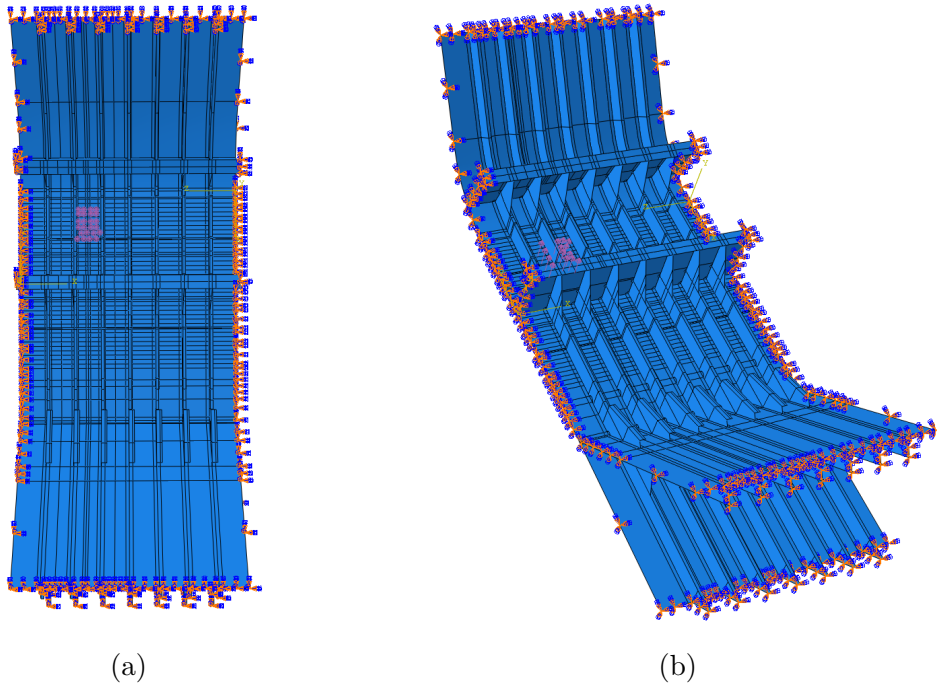


Figure 4.7: Rigid boundary conditions and a sample load of the FE model

4.3.3 Mesh

The geometry is meshed using shell elements of varying thicknesses according to the structural plans of the *IB Baltika*. The main shell and frame structures are meshed with quadrilateral elements and the areas surrounding small cutouts or brackets are meshed with triangular elements.

Four mesh densities are evaluated in this study on the basis of the ICMs created by each model. Table 4.2 summarises the properties of the four meshes used to create four different ICMs and Figure 4.8 provides samples of the different meshes.

Using the methods presented in Section 4.2.1, the strain response curves are fitted for each model to generate the respective ICMs. Figures 4.9 and 4.10 present sample shear and normal response curves, respectively, for varying mesh densities. The four response curves indicate the response is converging as the density of the FE mesh increases.

When analysing the raw strain results generated by the four FE models, the difference between strains simulated with the finest and the coarsest mesh is less than $1 \mu\text{strain}$ for the majority of applied loads. While there are some cases with strain

differences greater than $1 \mu\text{strain}$, they occur on the outer boundaries of the solution areas and the largest difference is $10 \mu\text{strain}$. The accuracy of the installed measurement system is $0.5\text{-}2 \mu\text{strain}$ depending on the sensor [61], and therefore, the differences between the finest and coarsest mesh are acceptable and all meshes are valid. The selection of the final mesh is described as part of the inverse method verification process in Section 4.5.2.

Table 4.2: Summary of the different mesh properties

| Mesh | Global Seeding [m] | Number of Elements | Number of Nodes |
|------|--------------------|--------------------|-----------------|
| 1 | 0.0125 | 291 000 | 270 700 |
| 2 | 0.0250 | 84 300 | 79 400 |
| 3 | 0.0500 | 29 800 | 28 600 |
| 4 | 0.0750 | 21 500 | 20 650 |

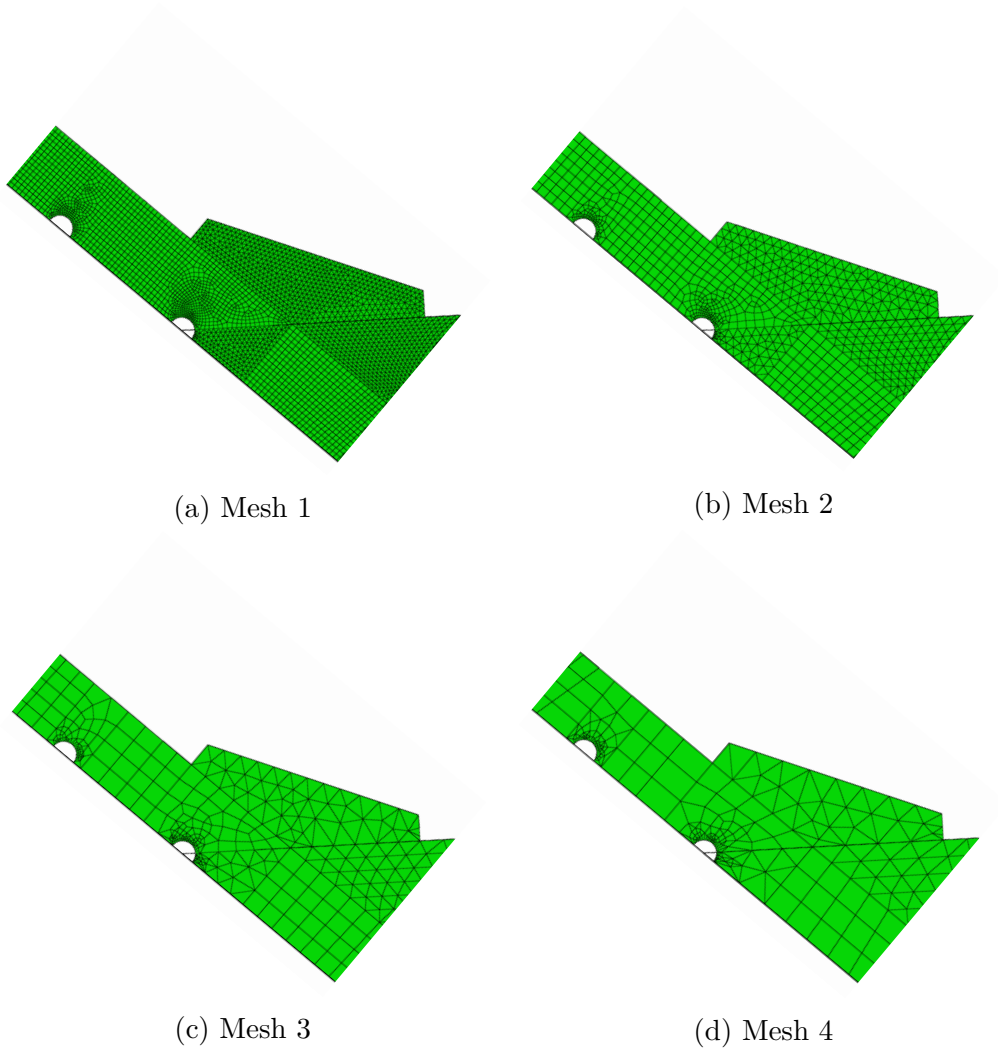


Figure 4.8: Comparison of mesh densities

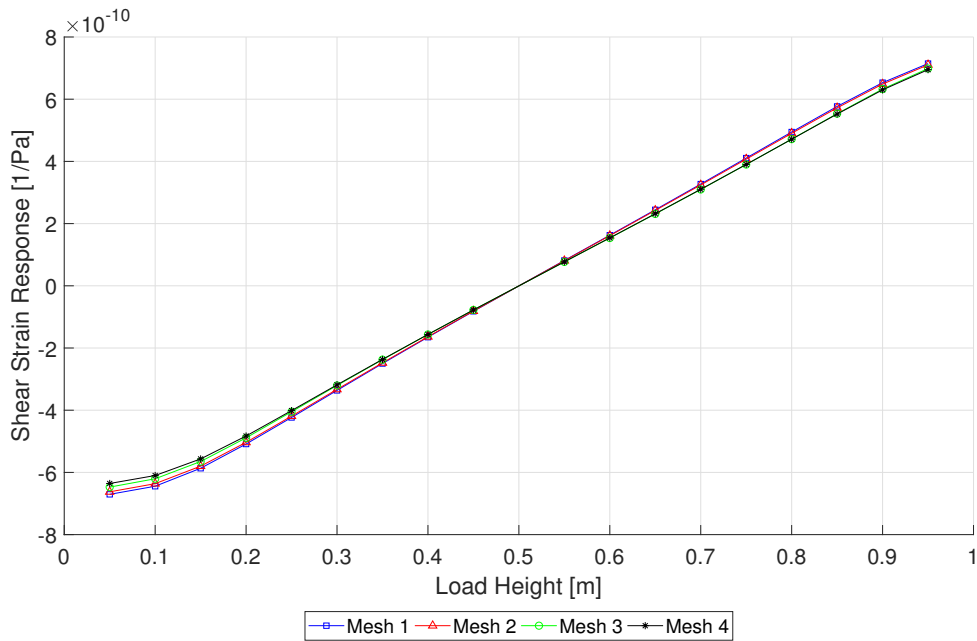


Figure 4.9: Shear strain response between sensors FR13 and FR14 for varying mesh densities

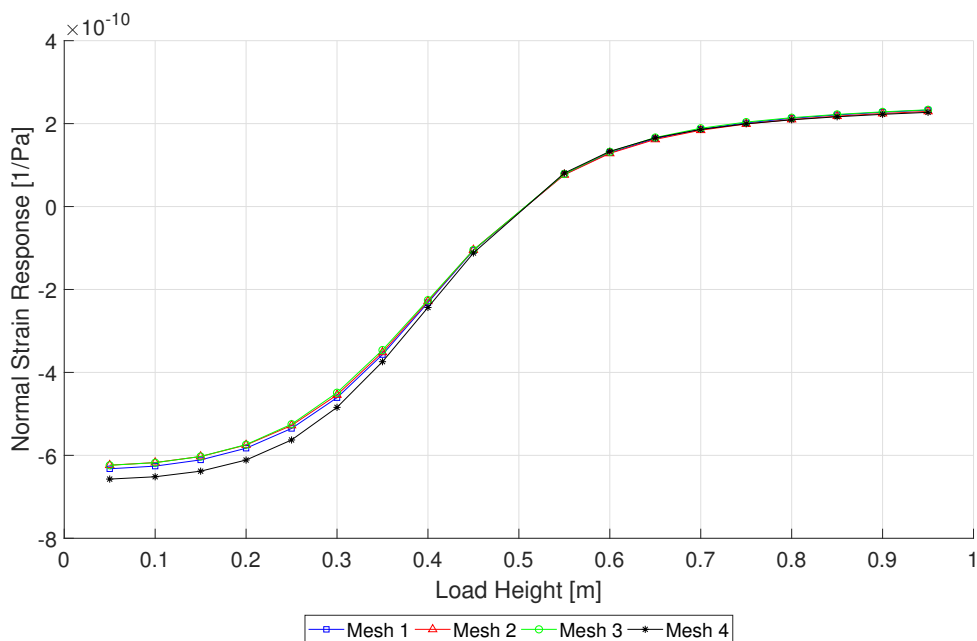


Figure 4.10: Normal strain response at sensor PL5 for varying mesh densities

4.4 Optimisation Algorithm

The equation presented in Equation (2.2) is solved using optimisation functions in MatLab [62]. The inverse problem is classified as a multi-objective minimisation problem that is subjected to linear inequality constraints and whose variables are bounded. Based on MatLab documentation, the *patternsearch* function is the recommended optimisation function [63].

The solution process is such that once the strain history for the desired time period is known and the ICM is determined, the minimisation routine is run to determine the results for Discretisation 1. One limitation of the current algorithm is that it treats the two areas above and below the stringer independently, and therefore, it is possible that two simultaneous loads are identified. As it is unlikely that two large ice-loads occur simultaneously on the same frame span, only the largest, non-infinite load is considered.

Based on the Discretisation 1 solution, the algorithm determines the area in which the load occurred. To find the solution for Discretisation 2, the minimisation routine is run again; however, only for the solution area found using Discretisation 1. For example, if the load is found to be in Solution Area 1 for Discretisation 1, then the minimisation routine is only run to solve for $p_{1,\#59}$, $p_{1,pl}$ and $p_{1,\#59.5}$ to save on computation time and effort. The load height is assumed to be constant between discretisations, and therefore, the load heights found in Discretisation 1 are used as input for Discretisation 2. For reference, the run time for each one-second loading event, with a measurement frequency of 100 Hz, is generally 1-2 hours for Discretisation 1. Therefore, reducing the computational time where possible is important to ensure a sufficient number of cases can be analysed. Figure 4.11 outlines the flow of the optimisation routine.

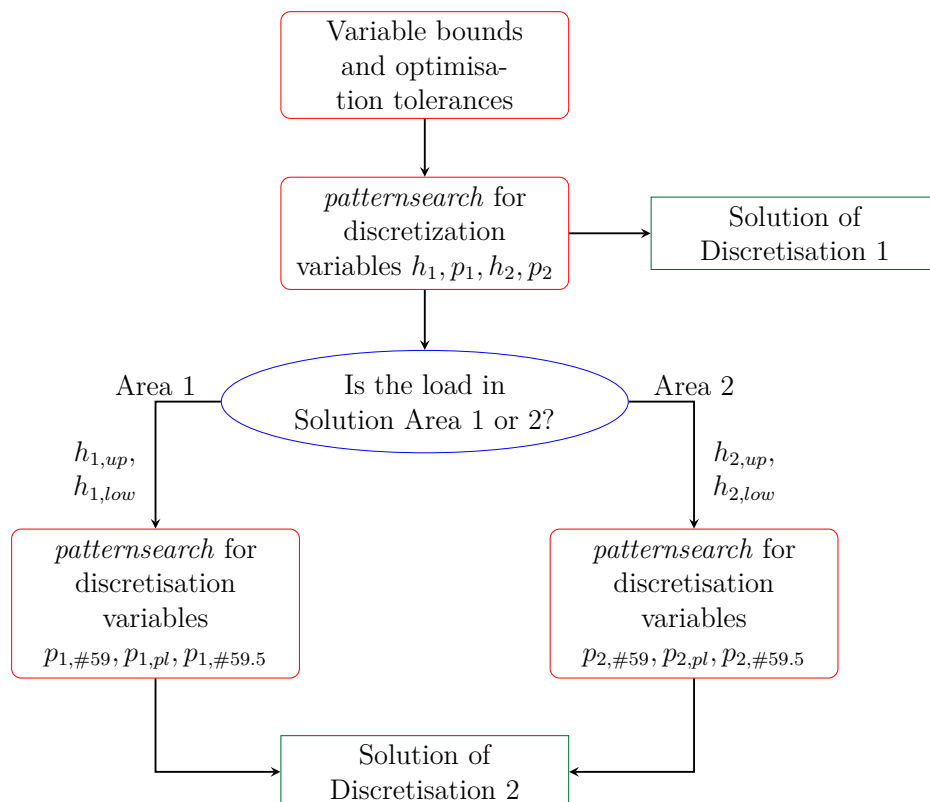


Figure 4.11: Flow chart of the solution process

After identifying the load and load height, the post-processing of the results can occur. This includes, but is not limited to, visualising how the load moves during the loading events, analysing the distribution of peak loading events and studying the distribution of forces between structural members.

4.5 Method Verification

To assess the proposed inverse method, several trial cases are evaluated. The FE model is used to create strain vectors for known applied loads with varying locations and magnitudes. The inverse method is applied to the simulated strain state to estimate the input load. The resulting load is compared to the original input of the FE model.

Since the method could not be verified with full-scale data, alternative precautions must be taken to avoid inverse crime. The mesh independence study concluded that each of the four meshes are valid. Therefore, in an effort to avoid inverse crime, the strain vectors for each trial case were created using an FE model with a different mesh density than the model being investigated. This technique reduces the probability of inverse crime since the same model is not used to verify itself.

4.5.1 Optimisation Properties and Input

Results of optimisation routines can be quite sensitive to the tolerances and properties that are used as input for the program. An investigation of the influence of the tolerances and initial guesses is conducted to determine the most appropriate tolerances that balanced result accuracy and computational time. The ICM and the strain vectors generated by Mesh 2 (Figure 4.8) are used to investigate the optimisation properties.

Four combinations of tolerances and initials guesses are used in the evaluation of the inverse method. The default tolerances are used in the first iteration and the tolerances are decreased in successive iterations. The limits of the height variables are used as initial guesses in the first three iterations and the centre of the height span is used in the fourth iteration. The initial estimate for the applied pressure is 0.1 MPa for all iterations. Table 4.3 summarise the tolerances and inputs of the four iterations.

Table 4.3: Optimisation input and tolerances

| Input Variable | Default | Iteration 2 | Iteration 3 | Iteration 4 |
|--------------------|--------------------|--------------------|---------------------|---------------------|
| Maximum Time [s] | Inf | 300 | 600 | 600 |
| Function Tolerance | 1×10^{-6} | 1×10^{-9} | 1×10^{-9} | 1×10^{-9} |
| Step Tolerance | 1×10^{-6} | 1×10^{-9} | 1×10^{-12} | 1×10^{-12} |
| Mesh Tolerance | 1×10^{-6} | 1×10^{-9} | 1×10^{-12} | 1×10^{-12} |
| $h_{1,up}$ [m] | 0.95 | 0.95 | 0.95 | 0.51 |
| $h_{1,low}$ [m] | 0.10 | 0.10 | 0.10 | 0.49 |
| $h_{2,up}$ [m] | -0.05 | -0.05 | -0.05 | -0.49 |
| $h_{2,low}$ [m] | -0.95 | -0.95 | -0.95 | -0.51 |
| p_1, p_2 [MPa] | 0.1 | 0.1 | 0.1 | 0.1 |

Ten trial cases are examined to determine the appropriate tolerances and the results of two sample cases are presented in Table 4.4. The cases are evaluated based on the results obtained for Discretisation 1. The results from the iteration using the default settings are neglected since the maximum number of iterations was the stopping criteria for every case indicating that the solutions had not converged. The analysis of the results from the remaining iterations revealed that, for each trial case, Iterations 2 and 3 converged on the same final result; however, Iteration 4 often terminated because the time limit was exceeded, indicating the optimisation routine had not converged within 10 minutes.

Table 4.4: Results of the optimisation properties investigation

| | Variable | Input | Iteration 2 | Iteration 3 | Iteration 4 |
|--------|------------------------|-------|--------------------|----------------|-------------|
| Case 4 | $h_{1,up}$ [m] | 0.50 | 0.53 | 0.53 | 0.48 |
| | $h_{1,low}$ [m] | 0.45 | 0.40 | 0.40 | 0.44 |
| | p_1 [MPa] | 10 | 3.83 | 3.83 | 12.6 |
| | Exit Criteria | – | Time Limit | Mesh Tolerance | Time Limit |
| | $h_1 \cdot p_1$ [kN/m] | 500 | 498 | 498 | 504 |
| Case 6 | $h_{2,up}$ [m] | -0.05 | -0.05 | -0.05 | -0.05 |
| | $h_{2,low}$ [m] | -0.15 | -0.17 | -0.17 | -0.17 |
| | p_2 [MPa] | 10.0 | 8.11 | 8.11 | 8.11 |
| | Exit Criteria | – | Function Tolerance | Mesh Tolerance | Time Limit |
| | $h_2 \cdot p_2$ [kN/m] | 1000 | 973 | 973 | 973 |

While the height and pressure results from Iteration 4 appear closer to the input values, the fact that the optimisation routine did not converge in the allotted time for several trials indicates that the results are unreliable. A small investigation was conducted for several diverging cases where the time limit was increased to 15 and 30 minutes; however, most cases remained unsolved, despite the increase in time. Furthermore, with the limit of 10 minutes, solving a one-second impact event, with data points at a frequency of 100 Hz, could take up to 1000 minutes, or 16.6 hours, if the time limit is reached for each time instant. Increasing the time limit further would not be feasible when analysing a large data set.

The calculated line loads in Table 4.4 justify the large difference between input load and the predicted results for Iterations 2 and 3. Despite the differences in load height and pressure, the resulting line load applied to the structure is accurately predicted. Additional trial cases can be found in Appendix 1.

The input and tolerances for Iteration 3 (Table 4.3) are used in the remainder of the study because Iteration 3 was found to balance an appropriate level of accuracy and computational time. Iteration 2 is not selected because the maximum time was reached for more cases than Iteration 3.

4.5.2 Selection of FE Mesh Density

In addition to selecting the optimisation inputs, the final ICM must be selected from the four that were created in the mesh independence study. The selection is made on the basis of the trial results obtained from the optimisation process using the inputs and properties of Iteration 3 (Table 4.3). The ICM that yielded the most accurate line loads for the majority of the trial cases is Mesh 3, which is a coarser mesh. Two sample trial cases are presented in Table 4.5 to show a comparison between the results from the four meshes. The remaining trial cases can be found in Appendix 1. The ICM created with Mesh 3 was selected as the final ICM to use in the analysis of the strain data measured on board the *IB Baltika*.

Table 4.5: Results of the ICM selection investigation

| | Variable | Input | Mesh 1 | Mesh 2 | Mesh 3 | Mesh 4 |
|--------|------------------------|--------|--------|--------|--------|--------|
| Case 1 | $h_{1,up}$ [m] | 0.550 | 0.532 | 0.532 | 0.531 | 0.531 |
| | $h_{1,low}$ [m] | 0.350 | 0.351 | 0.352 | 0.356 | 0.354 |
| | p_1 [MPa] | 10.00 | 11.08 | 11.14 | 11.46 | 11.30 |
| | $h_1 \cdot p_1$ [kN/m] | 2000.0 | 2010.1 | 2008.8 | 2003.6 | 2005.5 |
| Case 6 | $h_{2,up}$ [m] | -0.050 | -0.100 | -0.051 | -0.051 | -0.050 |
| | $h_{2,low}$ [m] | -0.150 | -0.211 | -0.166 | -0.162 | -0.164 |
| | p_2 [MPa] | 10.00 | 6.905 | 8.106 | 8.485 | 8.261 |
| | $h_2 \cdot p_2$ [kN/m] | 1000.0 | 765.5 | 933.2 | 941.0 | 940.5 |

4.5.3 Discretisation 1 Trial Loads

Following the selection of the ICM and optimisation properties, the results for the trial cases are analysed to determine the limitations of the developed method. The trial cases were chosen in an effort to represent as many different loading scenarios as possible. Table 4.6 presents a comparison between the inputs and results for four trial cases analysed with Discretisation 1. The remaining cases used to verify the inverse method are presented in Appendix 1.

The inverse method proved to work well for most load cases. The load heights are predicted within 5 cm for all load cases. However, the prediction of the magnitude of the loading varied more significantly between the trials. The calculated line load proved to be a better assessment of the accuracy of the method since it relates the pressure and the load height.

One limitation found in the verification process is that loads below 0.5 MPa are less accurately predicted. This is assumed to be due to lower strain magnitudes generated with low applied pressures. If the strain measurements are too low, it is hard for the inverse method to locate the load patch, and thus, the result is less reliable. However, since it is high loads that are of interest to this study, the lower accuracy for low magnitude pressure loads will have minimal effect on the results.

Table 4.6: Results of selected trial cases for Discretisation 1

| Variable | Trial 1 | | Trial 2 | | Trial 3 | | Trial 4 | |
|------------------------|---------|--------|---------|--------|---------|--------|---------|--------|
| | Input | Result | Input | Result | Input | Result | Input | Result |
| $h_{j,up}$ [m] | 0.50 | 0.51 | 0.350 | 0.36 | -0.55 | -0.56 | -0.25 | -0.20 |
| $h_{j,low}$ [m] | 0.45 | 0.42 | 0.325 | 0.328 | -0.75 | -0.73 | -0.30 | -0.33 |
| p_j [MPa] | 10.0 | 5.34 | 2.00 | 1.66 | 5.00 | 5.70 | 3.00 | 1.18 |
| $h_j \cdot p_j$ [kN/m] | 500 | 504 | 50.0 | 53.1 | 1000 | 981 | 150 | 147 |

4.5.4 Discretisation 2 Trial Loads

Trial cases including both applied loads with constant and varying pressures are used to validate the ICM created for Discretisation 2. In each trial, the pressures in the areas adjacent to the frames are of the same magnitude and the pressure in the middle panel has a different magnitude. For example, in Solution Area 1, pressures $p_{1,\#59}$ and $p_{1,\#59.5}$ have the same magnitude while pressure $p_{1,pl}$ had a different magnitude. The pressure ratios (Equation (4.8)) between the average frame pressure and the plate pressure ranged between 0.11 and 6 for the trial cases.

$$R = \frac{p_{fr}}{p_{pl}} \quad (4.8)$$

As with Discretisation 1, the estimated line load is the best way to show the accuracy of the inverse method. Large differences between the input pressures and load heights could be found in the trial cases; however, the resulting line loads proved the accuracy of the methods. The ratio between the pressure applied on the frames and on the plate is calculated. Table 4.7 presents four trial cases used in the validation of Discretisation 2. Additional verification trials are presented in Appendix 1.

The accuracy of the Discretisation 2 pattern is lower than that of the first pattern based on the larger differences between the calculated line loads. However, the pattern is capable of identifying three separate loads applied to the plate. There is a good correspondence between the loads predicted in both areas adjacent to the frames for each case with varying loads and between all three areas for load cases with evenly distributed applied loads (i.e. Trial 3 in Table 4.7).

Table 4.7: Results of the optimisation properties investigation for Discretisation 2

| Variable | Trial 1 | | Trial 2 | | Trial 3 | | Trial 4 | |
|-------------------------|---------|--------|---------|--------|---------|--------|---------|--------|
| | Input | Result | Input | Result | Input | Result | Input | Result |
| $h_{j,up}$ [m] | 0.40 | 0.42 | 0.51 | 0.53 | -0.40 | -0.41 | -0.35 | -0.37 |
| $h_{j,low}$ [m] | 0.30 | 0.28 | 0.50 | 0.49 | -0.45 | -0.43 | -0.65 | -0.62 |
| $p_{n,\#59}$ [MPa] | 10.0 | 6.70 | 1.00 | 0.35 | 5.50 | 14.5 | 1.00 | 1.34 |
| $p_{n,pl}$ [MPa] | 6.00 | 4.65 | 9.00 | 1.90 | 5.50 | 12.8 | 3.00 | 3.48 |
| $p_{n,\#59.5}$ [MPa] | 10.0 | 6.48 | 1.00 | 0.42 | 5.50 | 15.6 | 1.00 | 1.33 |
| $h \cdot p_{fr}$ [kN/m] | 1000 | 922 | 10 | 15 | 275 | 301 | 300 | 334 |
| $h \cdot p_{pl}$ [kN/m] | 600 | 667 | 90 | 76 | 275 | 279 | 900 | 856 |
| R [-] | 1.67 | 1.38 | 0.11 | 0.20 | 1.00 | 1.08 | 0.33 | 0.39 |

5 Results and Discussion

Results are obtained for both the general and the detailed event analyses by applying the inverse method developed in Chapter 4 to the loading events identified in Section 3.3. First, the general analysis results are presented. The broader range of events allows for the study of the distribution of estimated peak loads, the relationship between pressure and load height and other relationships that can be used to improve design techniques.

In the detailed impact event analysis, individual ice load events are analysed in their entirety from the approaching stage to the final disengagement of the load. The development of the ice-induced load, the relationship between peak strains and load location, and the load height throughout the loading period are presented. Finally, the results from the pressure distribution investigation using Discretisation 2 are given.

5.1 General Event Analysis

Figure 5.1 presents the distribution of peaks identified for the general analysis. Sensors PL1, PL2, PL11 and PL12 are located on the edges of the measurement area (Figure 2.17), and therefore, they are not included to remove the unintentional increase in the number of results that are centred around ± 0.4 m from the stringer. The strains measured on the normal sensors along the centre of the plate (Figure 2.17) align best with the peak load occurrence since the solution area is restricted to only one frame.

The distribution presented shows that the sensors PL3 and PL4, located near the upper edge of the solution area, experience only 15% of the total number of loads which is logical due to the increased distance from the design waterline. The higher number of loads on PL9 and PL10 compared to the sensors at similar distances from the stringer in the Solution Area 1 occurs because ice pieces are pushed below the ship as the ice bends and breaks leading to an increased probability of impact events.

The low number of peaks recorded for sensors PL6 and PL7 is explained due to their proximity to the stiff stringer. PL6 and PL7 are only ± 0.15 m from the stringer. Sensors PL6 and PL7 see a plate area with an aspect ratio of 1:1 where the boundary conditions have a significant influence. The increased stiffness of the plate field due to the boundary requires higher magnitude pressure loads to induce the same magnitude strains as found in the remaining plate field. On plate fields with ratios of 3:1 or higher, for example near sensors PL4 and PL9, the influence of the boundary conditions are negligible.

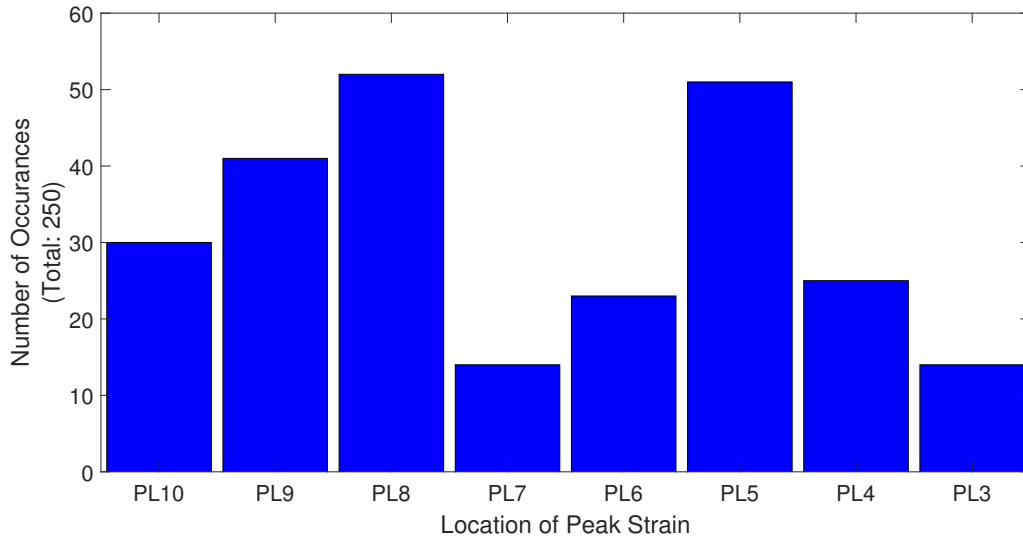


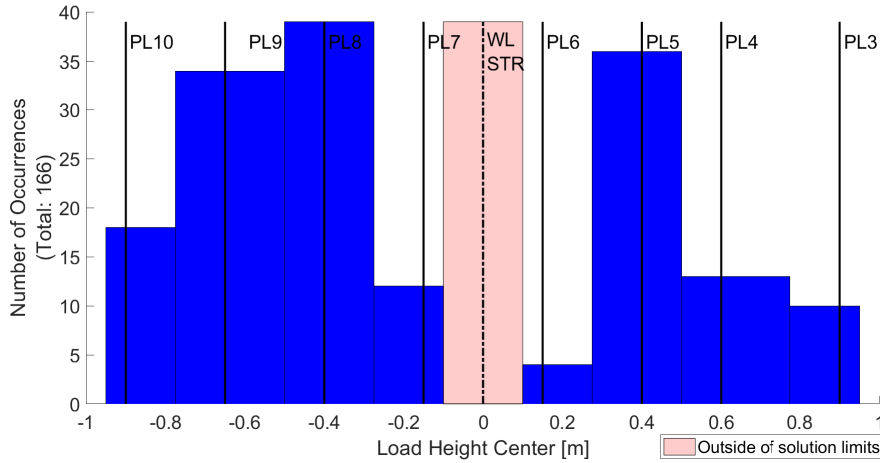
Figure 5.1: Distribution of measurement locations of maximum normal strains events for the general analysis

5.1.1 Load Location Distribution

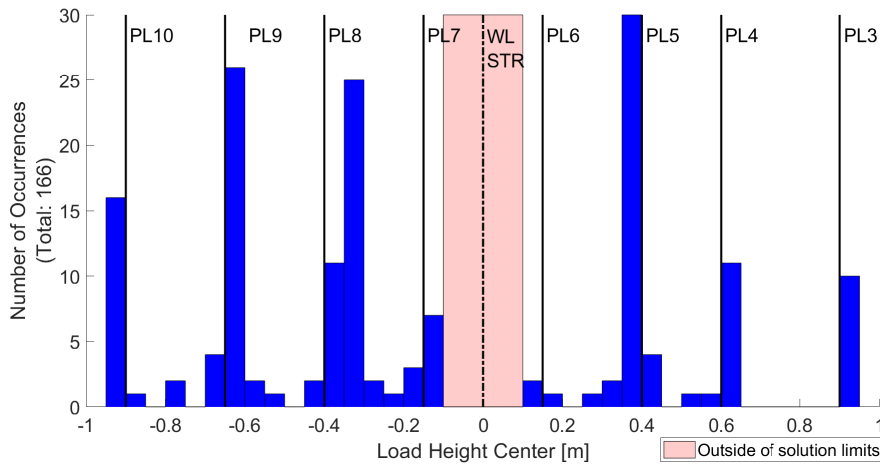
Of the 250 strains measurements selected for the general analysis, only the results of 166 events are presented since the solution of the remaining 84 events did not converge within the bounds of the optimisation routine. Figure 5.2 presents the distribution of the predicted load centres for the viable impact events.

The events discarded due to diverging solutions appear to be random when comparing Figures 5.1 and 5.2a since the overall distribution of loads follows the same pattern after removing the invalid solutions, with the exception of sensor PL6. There is a more pronounced reduction in the number of impact events centred around PL6 compared to other sensor which is assumed to be the result of its proximity to the design waterline. High impact loads that occur on the waterline would likely be registered as peaks on sensor PL6; however, if they occur in the area outside of the solution bounds, the inverse method is not able to identify them and the result would be a diverging solution.

Figure 5.2b presents the distribution of the load centres with finer bin widths. The aim is to examine in more detail where the loads occur. Since the impact events analysed were identified by peak normal strain measurements on individual sensors, it follows that most results would be centred about the plate sensors. Figure 5.2b shows that the load patches of the majority of analysed events are in fact located near the sensor locations. However, there is also a significant number of loads that occur between the sensors, particularly between sensors PL7 and PL8. This indicates that the inverse method is sensitive enough to capture loads throughout the full span of the investigation areas.



(a)



(b)

Figure 5.2: Impact load location distributions

Without information about the draft at the time of the impact events, some context is missing from the results. For example, it is unclear if the high number of impact loads on PL5 is due to the ship floating at a deeper draft than the design, thus moving sensor PL5 to be inline with the waterline or if the impact loads are due to ice pieces moving up the side of the hull. The increased number of loads on sensor PL5 could also be explained by the difference in density between ice and water. Sea ice is approximately 10% less dense than water depending on salinity and temperature, thus the ice floats on the surface [58]. Assuming a level ice sheet, approximately 10% of the ice thickness will be exposed above the water's surface, leading to possible ice contacts above the ship's waterline.

Similarly, it is unknown if the high impact loads on sensor PL8 and PL9 are due to ice at the water's surface or due to broken pieces impacting the hull as they move below the ship in the icebreaking process. While not integral to the determination of the magnitude of the pressure, knowledge of the draft of the ship would help in the overall understanding of the type of events that induce high magnitude ice loads.

5.1.2 Peak Pressure Distribution

Figure 5.3 presents the distribution of maximum pressures obtained for the 166 viable impact events. The range between 10 and 25 MPa accounts for 84% of the impact events. The results are expected to be centred about a relatively high pressure since the aim of the identification process (Section 3.3) was to create a set of impact events that would result in relatively high pressure loads.

The overall distribution of maximum pressures appears to follow the established statistical trends that govern extreme ice loads. Generally, extreme ice loads tend to follow exponential type distributions meaning the tail of the distribution becomes quite narrow and only a few extreme ice loads occur (Section 2.2.4.5). Of the 166 events analysed, only 4 events resulted in pressure loads above 25 MPa.

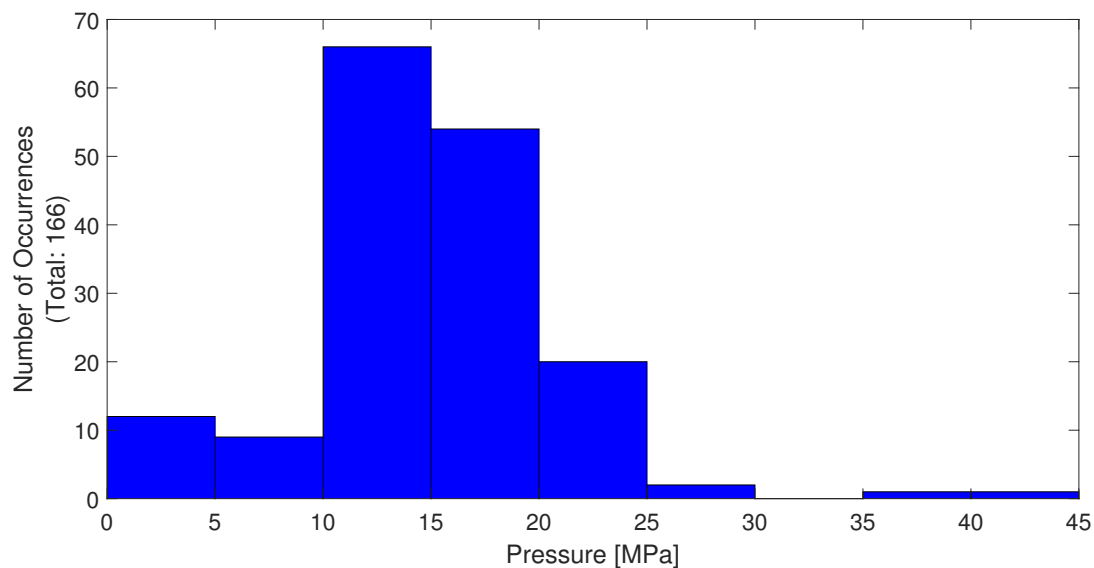


Figure 5.3: Distribution of peak pressures

5.1.3 Load Height Distribution

The results from the strain measurements taken on board the *IB Baltika* indicate that the load height at the peak of an impact event is in fact very narrow. Figure 5.4 shows that most impact events have load heights on the order of 1-2 cm and only 12 impacts had load heights greater than 5 cm.

The results presented in Figures 5.3 and 5.4 indicate that ice-induced pressures are more concentrated than assumed by the design rules [3, 46]. The ice-induced loads are narrow and line-like as observed visually on board the *IB Sampo* in the 1990s [6, 19].

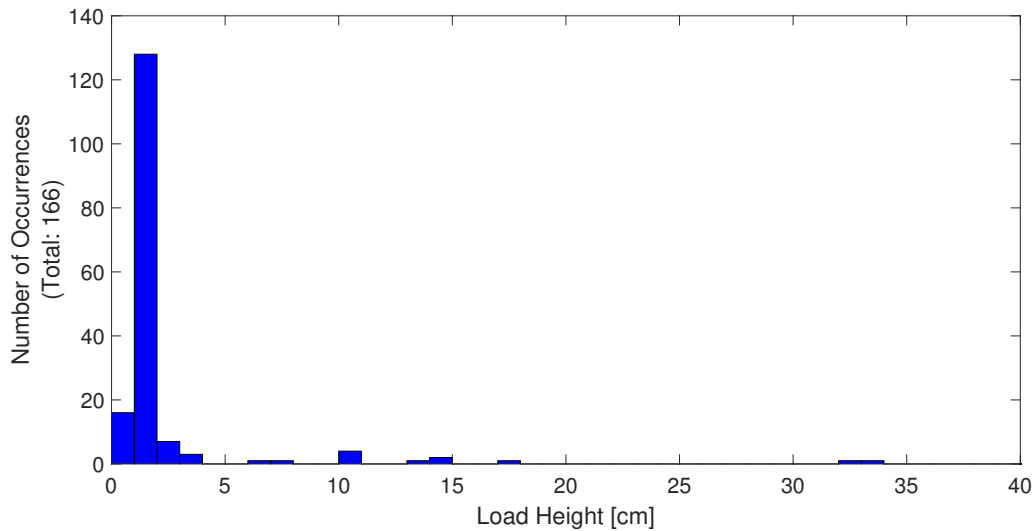
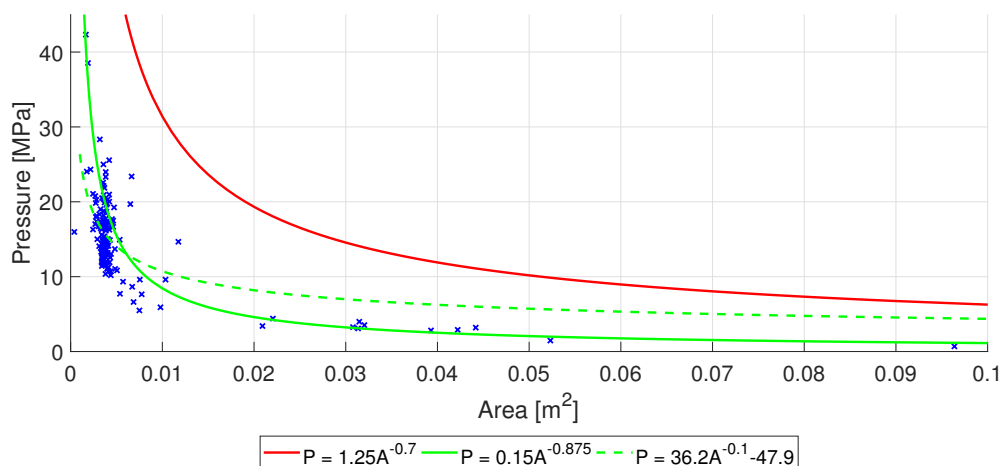


Figure 5.4: Load height at impact distribution

5.1.4 Pressure-Area Curve

Figure 5.5 presents the pressure-area curve assuming the load patch has a height equivalent to the predicted load height and a width equal to the frame spacing. The design curve presented in Section 2.2.3 is shown in comparison to the pressure loads estimated for the *IB Baltika*. All the data points fall within the limits of the design pressure-area curve; however, Figure 5.5 reveals that the design curve overestimates the pressure acting on a given area. The design curve was created based on high impact loading events and is used most often in off-shore applications. Therefore, a ship operating in first-year ice would not be expected to experience loads of such a high magnitude.

Figure 5.5 presents two curves in addition to the design curve that are fitted to the results of this study. Both curves predict steeper curves than the design curve for small areas indicating more concentrated pressure loads than predicted by the design curve.

Figure 5.5: Pressure-area curve for ice-induced loads on the *IB Baltika*

5.2 Detailed Event Analysis

Both shear and normal sensors were used in the selection of strain measurements for the detailed analysis. Figure 5.6 reveals that events identified by the four shear strain pairs located on the frames are distributed almost equally. The near equal distribution presented in Figure 5.6 is expected since ice loads occur randomly. The shear strain is recorded as a difference between sensors located at the extents of each solution area and, therefore, the shear strain signals should capture all loads on the plates and the loading events should be distributed almost evenly between all sensors. The FR17_18 sensor pair recorded slightly fewer loads than the other sensors; however, for the limited sample size of 52 loads, it is expected that the distribution is not exactly equal between all sensors. The lack of loading events on STR21_22 pair is due to the increased stiffness of the stringer meaning it is less likely to deform and to record strains of the same magnitude as the frames.

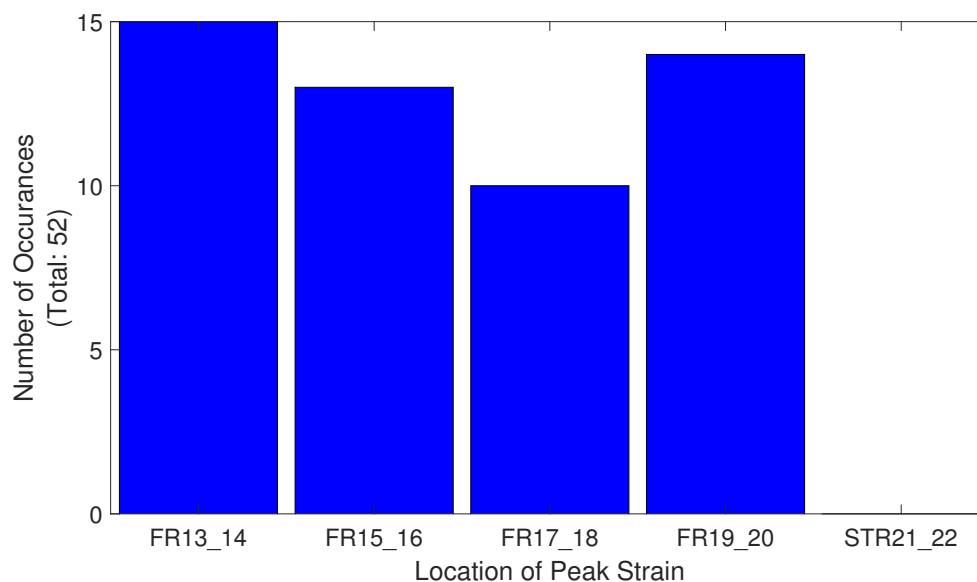


Figure 5.6: Distribution of shear strain peaks identified for the detailed event analysis

Figure 5.7 presents the distribution of the peaks identified by all the normal strain sensors. The distribution shows that sensors located the furthest from the waterline (PL3, PL4, PL10) recorded significantly less peaks than the sensors near the waterline. The remaining loads are fairly well distributed between the sensors surrounding the waterline.

The pattern of the sensor locations introduces a slight bias since sensors PL1, PL5, and PL11 are located along the same horizontal line in Solution Area 1 and PL2, PL8 and PL12 are located in a horizontal line in Solution Area 2. The bias results in a higher number of results centred around ± 0.4 m from the waterline as opposed to an even distribution of the results. Since the loads associated with the distribution shown in Figure 5.7 are only used to analyse the loading history of the individual events, the bias is acceptable.

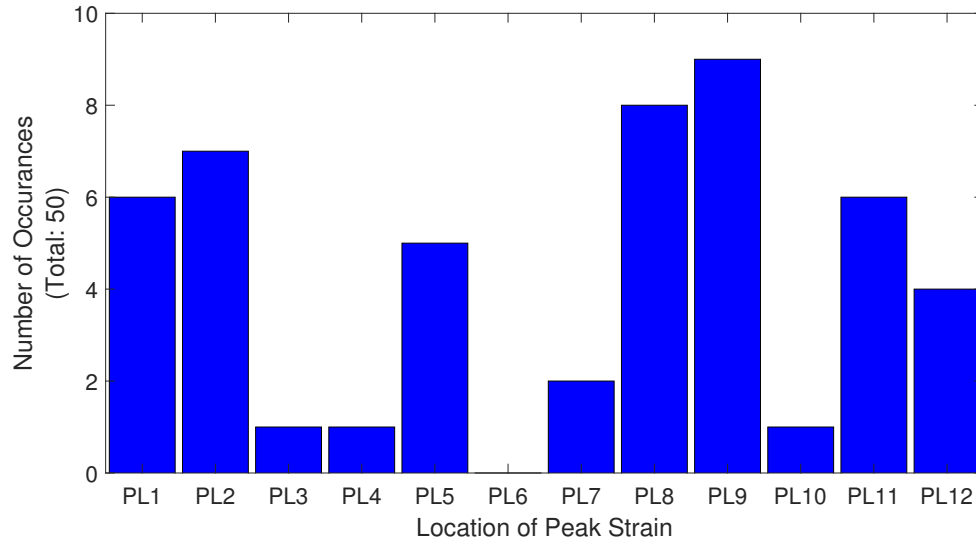


Figure 5.7: Distribution of normal strain peaks identified for the detailed event analysis

5.2.1 Sample Cases

Three example cases of the full event loading history are presented to illustrate the results obtained from the inverse method. The selected cases are distributed throughout the time history, both before and after the yielding events shown in Figure 3.4. The strain history of each of the three events also vary in their characteristics. Table 5.1 summarises the characteristics of the predicted ice-induced load and the strain histories for the three events. Figures 5.8 through 5.13 present the visualisations and time histories of the three sample events. Appendix 2 contains 15 additional cases with figures of the load patches and the time histories.

Table 5.1: Details of sample loading events

| Case | Date | Max Pressure [MPa] | Load Height [cm] | Notes |
|------|-------------|--------------------|------------------|------------------------------------|
| 1 | 28.Dec.2015 | 10.9 | 1.14 | Small peaks on varying sensors |
| 9 | 17.Dec.2016 | 16.9 | 1.20 | 1 smooth peak on one sensor |
| 54 | 2.Mar.2017 | 11.8 | 2.20 | 2 smooth peaks at different starts |

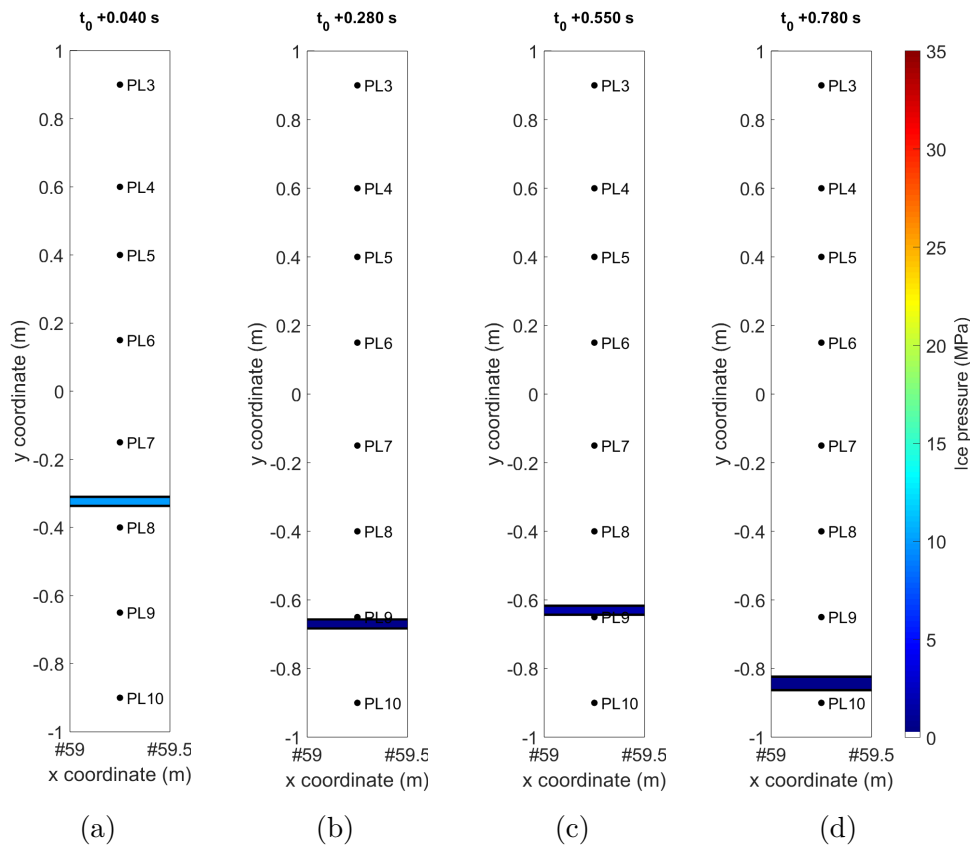


Figure 5.8: Sample load patches for Loading Event 1

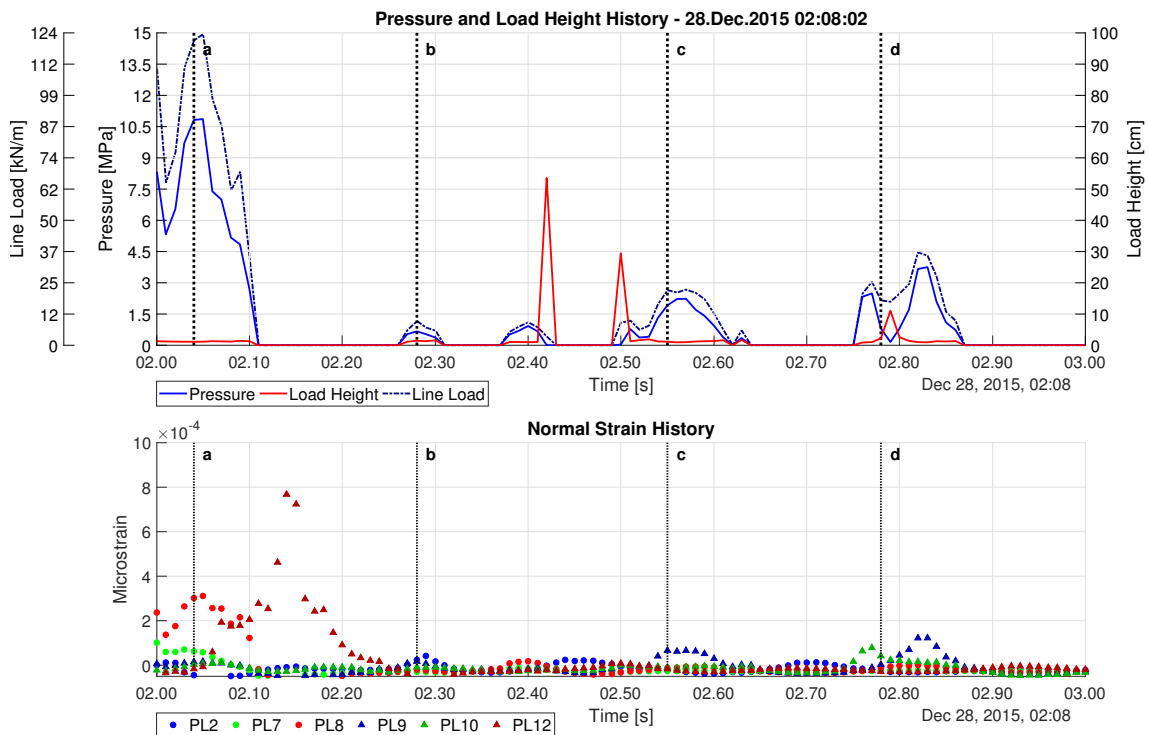


Figure 5.9: Relevant time histories for Loading Event 1

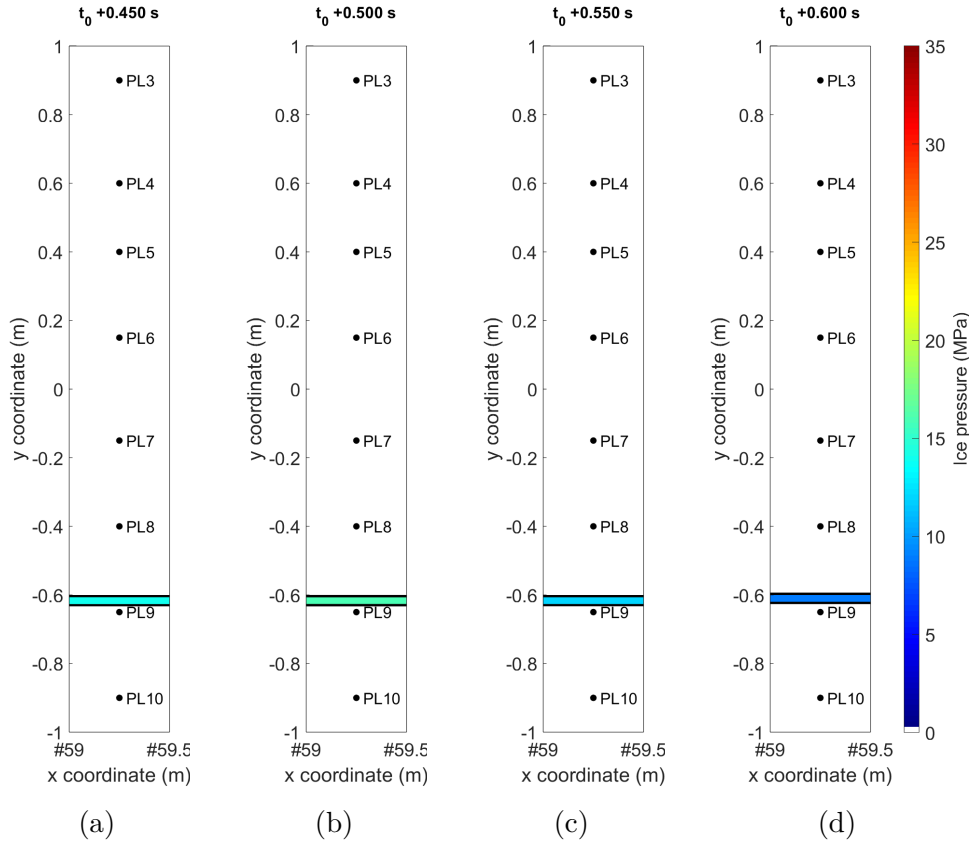


Figure 5.10: Sample load patches for Loading Event 9

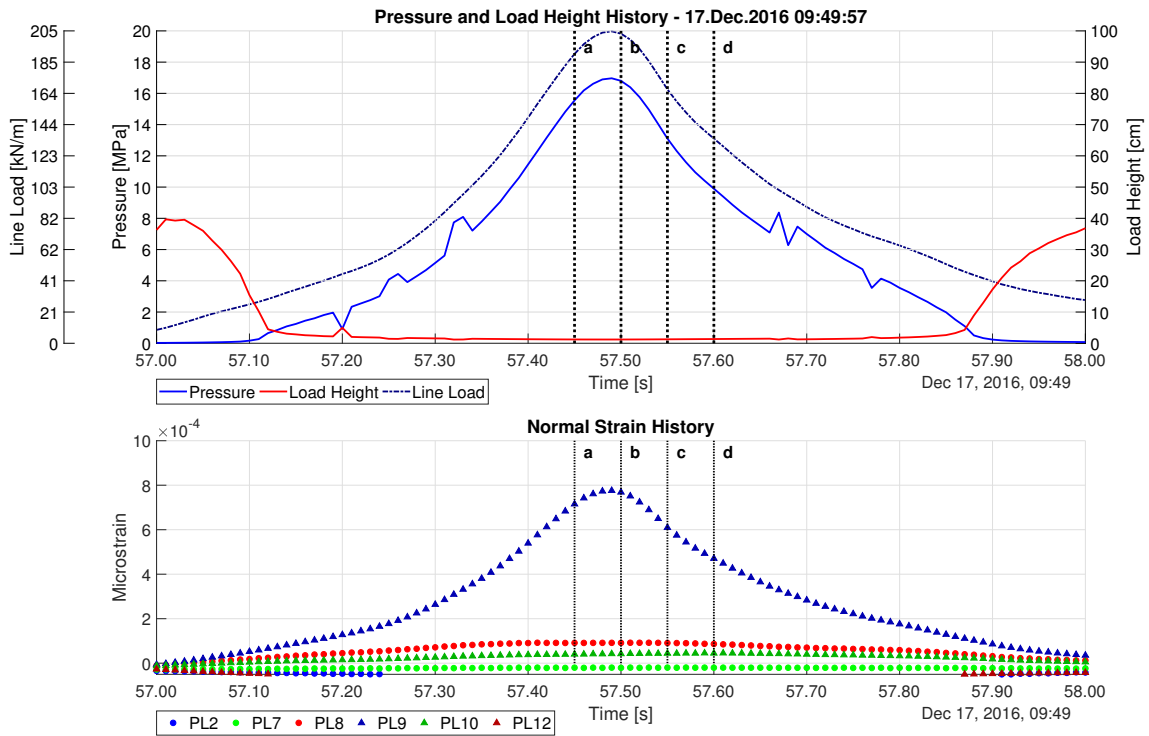


Figure 5.11: Relevant time histories for Loading Event 9

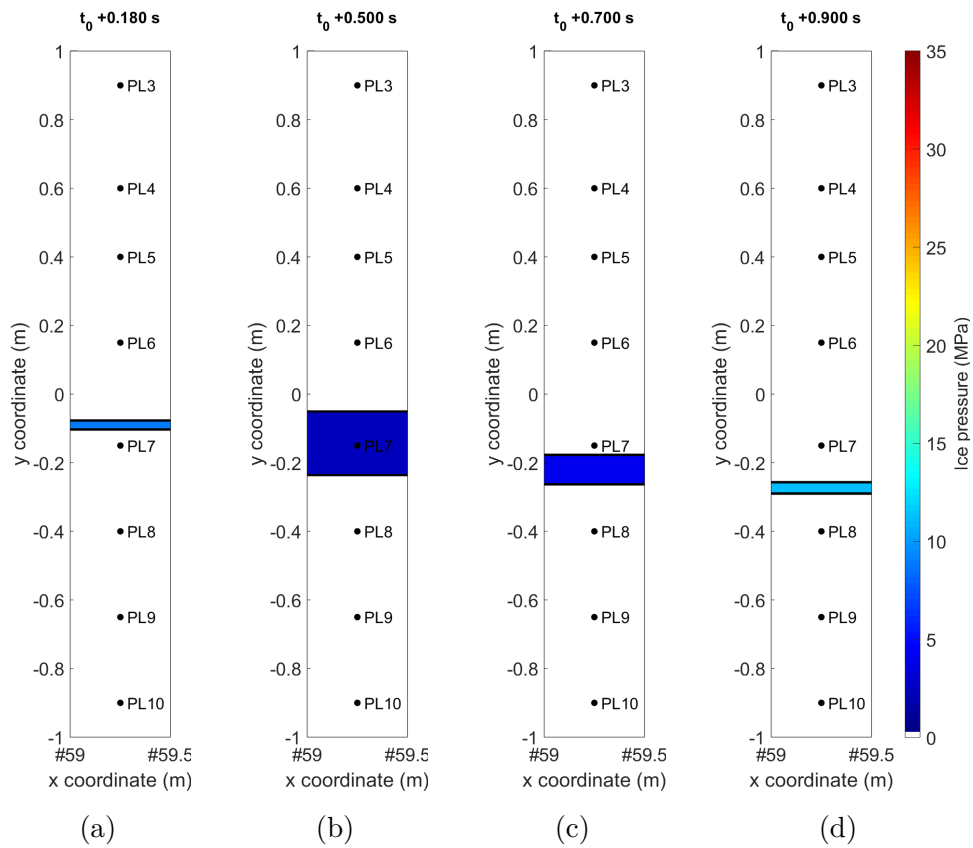


Figure 5.12: Sample load patches for Loading Event 54

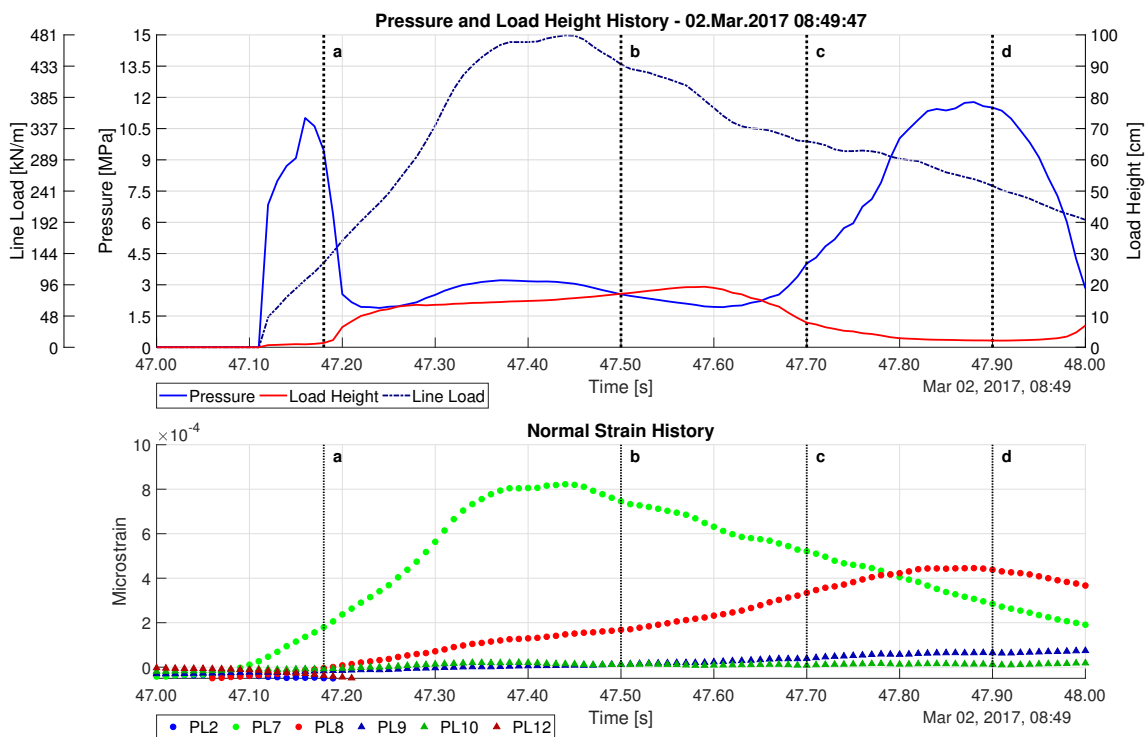


Figure 5.13: Relevant time histories for Loading Event 54

5.2.2 Load Patch Location

Analysis of the load height predictions indicate that the inverse method can identify the location of the applied load well in the vertical direction. The correlation between the peak strains and the location of the load patch for each loading event is evident when comparing the load patch figures to the respective strain histories.

During Event 1, there are peak strains recorded on sensors PL8, PL9 and PL10 at different points in time (Figure 5.9). The strain peaks during Event 1 are reflected in Figure 5.8 as the load patch moves throughout the event to match the sensors with the highest strain. In contrast, during Event 9, there is only one smooth strain peak on sensor PL9 (Figure 5.11). The corresponding load patches in Figure 5.10 show that the load patch remains almost stationary, and centred near PL9 for the duration impact.

Event 54 has a more complicated strain history than Events 1 and 9 since two strain peaks build on different sensors with only a small difference in time in between. At approximately $t_0 + 0.1$ s, the strain measured at sensor PL7 begins to build quickly resulting in a pressure peak concentrated around that sensor. At sensor PL8, a strain peak begins to show 0.1 seconds later; however, the strain increases at a slower rate. The result is a wider load patch between sensors PL7 and PL8. Finally, at the time of maximum strain on PL8, the strain measured on sensors PL9 and PL10 grows and a more concentrated load patch occurs between PL7 and PL8. Event 54 also provides an example of the ice contact moving down through the impact event. The downward movement of the load patch implies that the ice piece moves down after it breaks.

5.2.3 Load Height

Two important observations can be made through the analysis of the load heights predicted for the detailed analysis events. The first is that the load heights are generally on the order of 1-3 cm when the maximum pressure occurs. The second observation is that the load height remains approximately constant for the duration of the impact event.

The majority of the load heights predicted in the detailed analysis fall between 1-3 cm. The narrowness of the load height is important to note as it indicates that ice-induced loads are highly concentrated on a small portion of the ship's structures. Recalling Figure 2.11 and the development of the understanding of load heights in the FSICR, the current rules use load patch heights on the order of 20-40 cm. For higher ice class vessels designed to PC rules, the load patch height can be on the order of 80-100 cm. The results presented in Figures 5.9 through 5.13 are 10 times narrower than the load heights used in the FSICR, indicating that ice-induced loads are strongly line-like in nature. The results correspond well with the observations of line-like ship-ice contacts from the full-scale measurements on board *IB Sampo* in the 1990s [19].

The second observation of the steadiness of the load height is best illustrated in Figure 5.11. For the majority of the impact event, the load height remains virtually

unchanged for Event 9. The consistency of the load height during the peaks of the impact events was observed in all cases. On the basis of the pressure-height relationship presented in Figure 2.11, it was anticipated that the variation in load height over time would be the inverse of the pressure variation or more random in nature. The results, however, indicate that there is only a small variation in pressure near the beginning and end of the impact events, and the load height remains constant otherwise.

5.2.4 Pressure Development

The stages of pressure induced loads observed in Figure 2.5 are evident in the pressure histories presented in Figures 5.9, 5.11 and 5.13. During each impact event, the strain builds gradually during the initial stages until a peak pressure is achieved; at which point, the load disengages, generally at a faster rate than during the pressure build-up. Furthermore, the period over which the impact event occurs is typically on the order of 0.5 seconds.

5.2.5 Line Load

During the ice trials of the *IB Baltika* a scaling matrix was generated using the same FE model (Section 4.3) to estimate the force applied on each frame [60]. The scaling matrix directly relates the measured shear strains to force, but it does not consider the measured normal strains. Ice-induced load estimations on the basis of measured shear strains is one of the most common methods used [7, 16, 11, 64]. As such, a comparison was made between the line loads predicted using the inverse method, by multiplying the pressure and the load height, and line loads predicted by estimating the force using the scaling matrix. In the scaling matrix estimation, the line load, q , is calculated using Equation (5.1) where $F_{\#59}$ and $F_{\#59.5}$ are the forces estimated using the scaling matrix method on Frames 59 and 59.5, respectively.

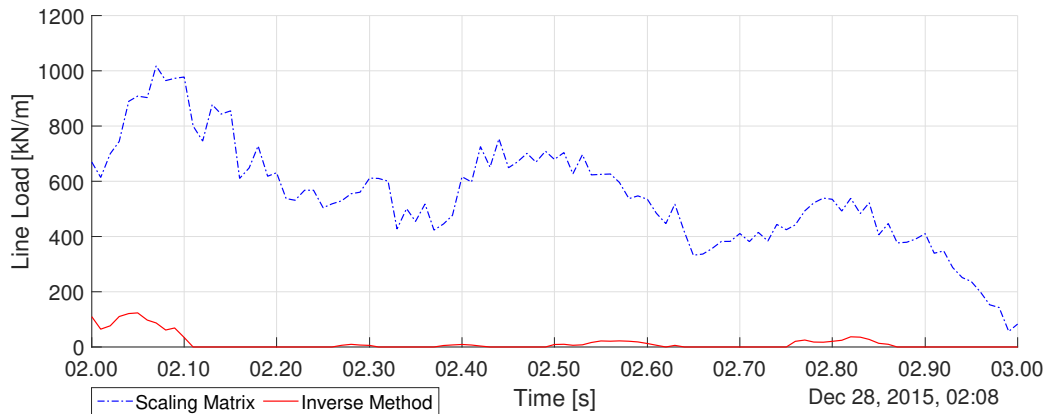
$$q = \frac{F_{\#59} + F_{\#59.5}}{2 \cdot \text{frame spacing}} \quad [kN/m] \quad (5.1)$$

Figure 5.14 presents the estimated line loads for the three cases presented in Table 5.1. Comparing the two predicted line loads, it is clear that the magnitude of the predicted line load is higher when using the scaling matrix method for all three cases. However, the line loads predicted by both methods follow similar trends. The difference in magnitude of the load lines can be attributed to two potential sources of error. The first is the limitation of the inverse method to only identifying the dominant load patch and the second is the unknown load length.

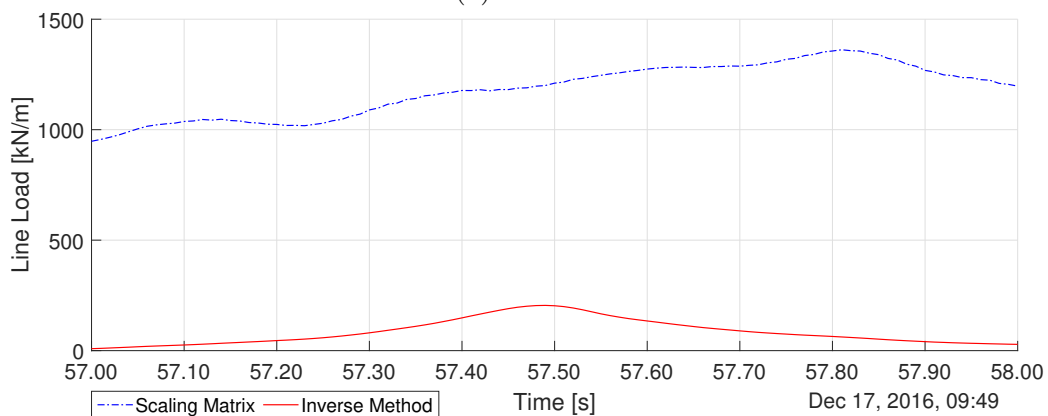
The inverse method used in this thesis does not allow for multiple load patches to occur simultaneously within the two instrumented frames. Only the dominating pressure zone is identified and, therefore, it is not possible to identify secondary lower pressure zones. The scaling matrix method for estimating line loads takes into consideration the full span of the solution area. It is likely that if there are lower pressure zones in addition to the peak pressure zone, the overall line load experienced by the structure would be higher than the line load calculated for only

the high pressure zone identified by the inverse method.

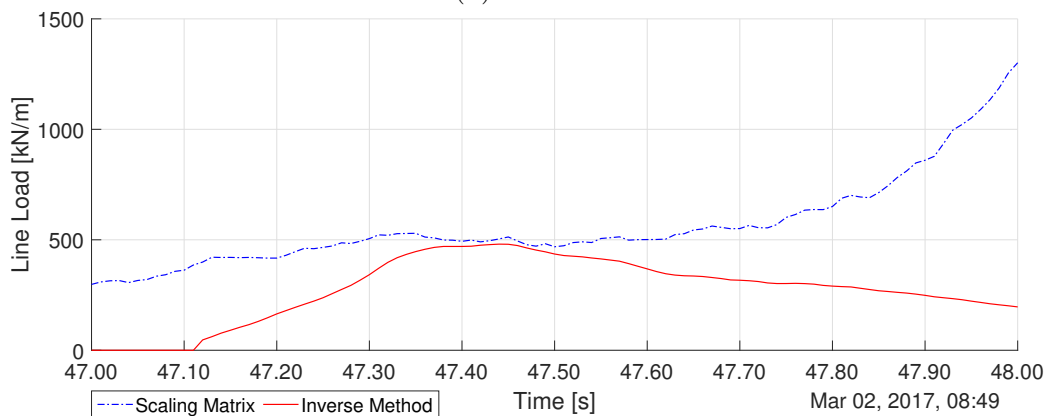
The load length will also have an influence on the magnitude of the line load. Since only two consecutive frames are instrumented with shear sensors, it is difficult to accurately predict the load length. Equation (5.1) assumes that the ice-induced load is 0.6 m long; however, it is possible that more frames are affected by the applied load. Considering these sources of error, only the trends of the predicted line loads are examined.



(a) Event 1



(b) Event 9



(c) Event 54

Figure 5.14: Comparison of line load estimation techniques

During Event 1, the maximum load occurs at the beginning of the time history. The magnitude of the load then decreases throughout the duration of the impact. There are two secondary peaks that are evident in both line load predictions. Event 9 presents a smooth, steadily increasing line load in both cases; however, the maximum load predicted by the scaling matrix method is delayed compared to the maximum load from the inverse method. The two line load predicted for Event 54 do not align as well as the other events. At the end of the impact event, the scaling matrix predicts a significant increase in force which is not apparent in the inverse method prediction. Without studying a longer period, it is unclear whether the increase in force is a delayed peak, similar to Event 9, or if it is the result of the following impact event. Appendix 3 contains the line load plots for the additional impact events presented in Appendix 2.

The comparison of line load estimation methods reveals that areas of further development and research remain. The current inverse method identifies the dominant pressure patch during a ice impact event well; however, the potential for the occurrence of concurrent lower pressure patches is clear. Further research is required to investigate the difference in predicted line loads and the interaction between multiple pressure patches.

5.3 Load Bearing Structures

As mentioned in Section 3.3, a total of 168 impact events were selected with high magnitude strains recorded simultaneously on both frames. The events were used to investigate the pressure distribution between the plate and frame structures. Discretisation 2 was applied to determine the ice-induced pressure on the three areas pictured in Figure 4.3. Following the application of the inverse method, 160 events produced valid solutions; however, 63 impact events did not identify forces for all sections of the discretisation. Therefore, only 97 events are considered for the analysis.

For each impact event, the ratio between the maximum average pressure experienced by the frames and the maximum pressure experienced by the plate was calculated according to Equation (4.8). Figure 5.15 presents the complete distribution of the ratios calculated for each of the impact events and Table 5.2 and Figure 5.16 provide summaries of the results.

Table 5.2: Summary of results for the investigation of load bearing structures

| Structure | Range of R | No. of Events |
|-----------|-------------------------|---------------|
| Plate | $0.00 < R < 0.75$ | 51 |
| Uniform | $0.75 < R < 1.25$ | 4 |
| Frames | $1.25 < R < \text{Inf}$ | 42 |

The summary of the results presented in Table 5.2 and Figure 5.16 indicates that there is no significant trend towards either a uniform distribution of the pressure

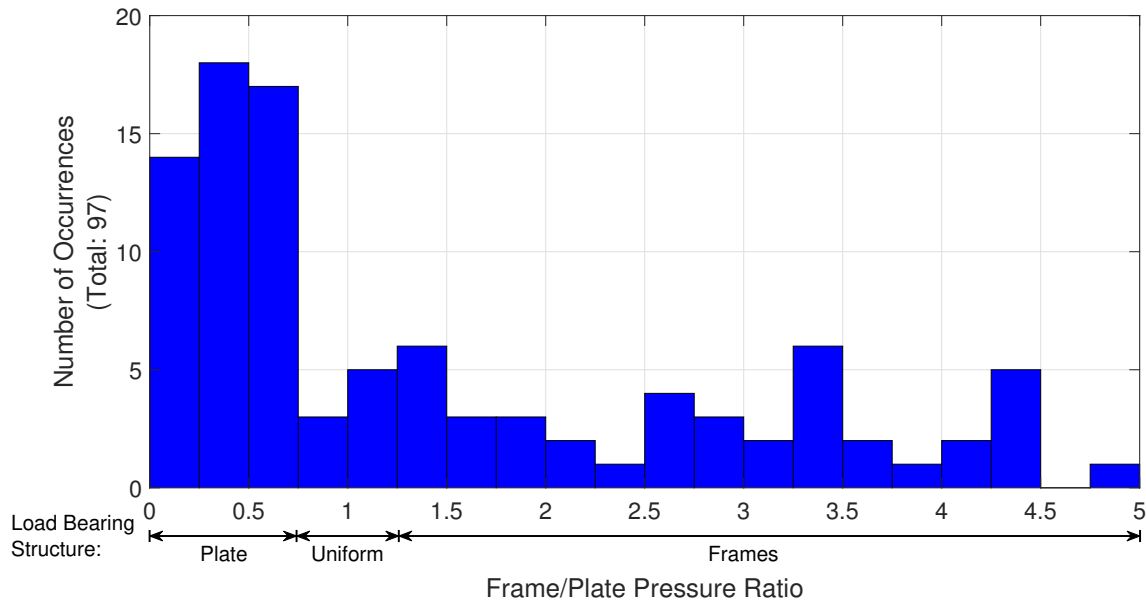


Figure 5.15: Distribution of frame/plate pressure ratios

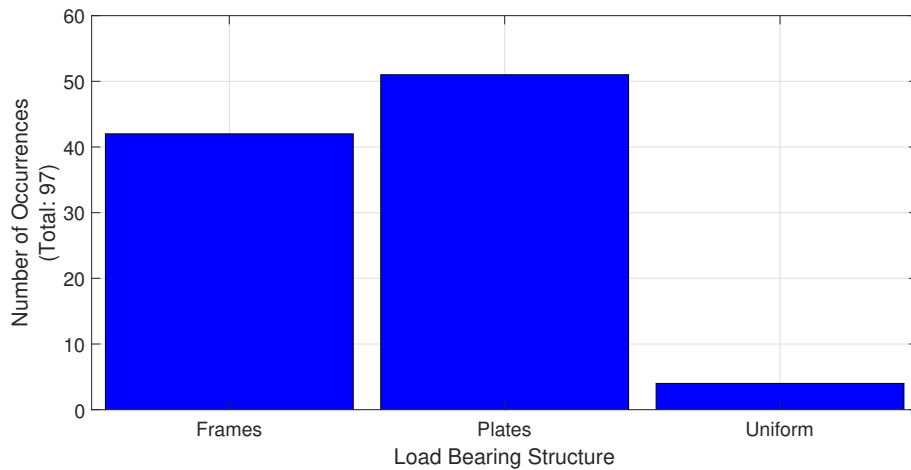


Figure 5.16: Simplified distribution of frame/plate pressure ratios

or a sinusoidal pressure distribution where the frames experience higher ice-induced loads (Figure 2.12). Considering the total number of impact events for each of the ranges given in Table 5.2, the number of events where the plates experience a higher pressure load than the frames is approximately equal to the number of events where the frames experience a higher pressure.

While Figure 2.12 implies that the pressure load is dependent on the ship's structure, the randomness of the results presented in Table 5.2 and Figure 5.15 prove otherwise. For example, if the frames did experience higher pressure loads, the distribution in Figure 5.16 would be heavily skewed towards either the plates or the frames. The stochastic nature of ice loads is translated to the pressure loads, thus resulting in a random distribution of pressure loads across the supporting structures. Therefore, the results of this study imply that the ice-induced pressure loads are independent of the structures of the ship.

6 Conclusions

An inverse method was implemented to analyse full-scale strain measurements taken on board the *IB Baltika* between May 2015 and May 2017. The measurement data was collected primarily in the Gulf of Ob in the Russian Arctic. Two discretisations were used to estimate the pressure and load patch height induced by impact events between the ship and the surrounding sea ice. Analysis of the strain data collected during the two-year measurement period revealed low magnitude yielding incidents; however, there is no indication of excessive deformation since the measurement system remained functional.

Finite element methods were used to create an influence coefficient matrix that describes the strain response of the hull structures to an applied load. The inverse method was applied to the strain measurements from 250 impact events for the general analysis of maximum ice-induced loads, 98 events were selected to analyse the details of the full impact event and a further 168 events were selected to investigate the structural pressure distribution.

The results of the study show that, for the analysed impact events, the peak pressure induced by the ice is most often between 10 and 25 MPa. The load height at the time of maximum pressure is on the order of 1-3 cm, confirming that the ice-induced loads are line-like. The results align well with visual observations made on board the *IB Sampo* in the early 1990s [6, 19]. The ice-induced pressures are higher and more concentrated compared to the design ice pressures used in classification rules.

The detailed analysis revealed relatively constant load patch heights over the duration of the individual impact events. Most high pressure impacts occurred in the area surrounding the design waterline. In most cases, the impact events are less than a second in duration and the full development of the pressure from the crushing stage to the load disengagement can be seen. The load height is markedly constant throughout the entire engagement of the load. The line loads estimated using the inverse method follow the same trends as the loads estimated using more common methods based on shear strains.

Using the Discretisation 2 pattern, the pressure distribution across the structural members was investigated. The results do not show a conclusive tendency for the frames to experience higher ice-induced pressures than the plates or for the distribution to be equal. For the 168 impact events analysed, the distribution between events where the plates experience a higher pressure and where the frame experience a higher pressure is almost equal. The results indicate that the distribution of pressure across the structural members is random and independent of the supporting ship structures.

Through the systematic study of approximately 350 valid ice impact events, the inverse method proved to be a functional tool for analysing ship-ice interactions. The dominant pressure patch is identified at each instant during an impact event and the results provide insight into the complex nature of ship-ice interactions. Further improvements are possible to allow more flexibility in the method with the aims of creating a more complete picture of the full ship-ice interaction.

7 Recommendations

To improve upon the method presented in this thesis, the following recommendations are made:

1. **Full-scale verification:** Efforts were made to verify the ICM matrices created using the FEM model. However, a better method of verification would be to have a data set of strain measurements associated with known input loads. In that way, inverse crime is avoided entirely as the verification of the computational model does not rely on the system model itself.
2. **Horizontal extension of the instrumented area:** Extending the method to include the analysis of several consecutive frames would be beneficial to gain a more complete picture of the ice-induced loads. The general understanding of ice loads is that the load length is often wider than a single frame span. The instrumentation pattern on board the *IB Baltika* is extensive in the vertical direction; however, since only 2 frames are instrumented, the results are limited to only 1 frame span. Including more instrumented frames would allow for the study of show the impact moves along the hull and how the load height varies as the load patch moves horizontally.
3. **Extend the analysis range:** For this thesis, the peak ice loads were of greater interest for their use in furthering design methods. However, from a scientific point of view, the data gathered on the *IB Baltika* is an extensive data set and it would be interesting to study the data set in its entirety. Understanding the full-spectrum of ice loads will help in the understanding of the mechanics behind ship-ice interactions.

Another aspect of the analysis range is the limits imposed during the optimisation process. A limit of 50 MPa was set during the optimisation routine for all pressure variables. For the events analysed in this work, the 50 MPa limit was appropriate; however, the highest strain measurements were not analysed due to the potential influence of non-linear effects. In future analyses, the upper limit of the pressure should be reevaluated to ensure it does not influence result.

4. **Ice conditions and ship operations:** The ice conditions and the ship's operations were not critical to understand the nature of the ice impacts events for this study. However, it would be advantageous to gather data concerning both the ice conditions and the ship's operations to add context to the loads, particularly for the larger impact events. This aspect is particularly interesting when considering how oblique operations might influence the load magnitude.
5. **Non-linear analysis:** The analysis of the normal strain histories revealed

that yielding events occurred during the two-year measurement period. In this work, a simple adjustment of the normal strains based on a bi-weekly moving median was used to account for the yielding events. The highest strain measurements were disregarded due to the high probability that non-linear effects would influence the strain measurements.

In future studies, a non-linear FE model is recommended to create the ICM. Yielding events must consider non-linearity in both the material properties and the geometry of the deformed structure. It is possible that a non-linear ICM would make it possible to evaluate the area surrounding the waterline stringer, in addition to the highest strain measurements.

6. **Ability to identify concurrent load patches:** The current inverse method identifies the dominant pressure patch induced by an ice impact on the ship's hull. However, it cannot determine if concurrent lower pressure zones exist. Developing the inverse method to be able to identify any number of simultaneous load patches would increase the methods ability to resolve the complex nature of ship-ice interactions.
7. **Discretisation 2 refinement:** The current plan for Discretisation 2 is suitable for a high-level investigation of the pressure distribution between frames and plates. The inverse method could be improved through the incorporation of triangular distributed loads or sinusoidal loads as the unit loads applied during the creation of the ICM. Continuous loads would allow more freedom in the pressure distribution compared to the discreet loads used in this study. A brief effort was made to incorporate non-uniformly distributed loads into the ICM; however, the preliminary investigation revealed that the ICM would be significantly more complex as it would be a function of multiple variables.

Based on the results and conclusions of this thesis, the following recommendations are made with the intention of improving ship structural design:

1. **Structural design investigation:** The results of the general analysis indicate that the ice impacts create concentrated, high-magnitude pressure patches on the hull structures. The nature of the load patch differs significantly from the load patches and design pressures used in design and classification rules and standards. It is unclear at this time how the line-like ice loads would affect the dimensions of the ship's structures if more concentrated loads were used as the design scenario. Therefore, an investigation of the effects the concentrated loads is recommended to determine their influence on the structural design with the aim of improving safety and efficiency, of ice-going ships.
2. **Further application of the inverse method:** There exists many full-scale data sets from numerous ships operating in different ice-covered waters. The inverse method developed in this thesis proved to be capable of identifying ice-induced pressures and load patches. Applying the method to additional data sets with different instrumentation layouts would be beneficial to determine the methods accuracy and allow for a comparison of the results.

References

- [1] H. Schøyen and S. Bråthen, “The Northern Sea Route versus the Suez Canal: Cases from Bulk Shipping,” *Journal of Transport Geography*, vol. 19, pp. 977–983, 2011.
- [2] M. Suominen, “Uncertainty and Variation in Measured Ice-Induced Loads on a Ship Hull,” Ph.D. dissertation, Aalto University, 2018.
- [3] K. Riska and J. Kamarainen, “A Review of Ice Loading and the Evolution of the Finnish-Swedish Ice Class Rules,” *SNAME Annual meeting*, pp. 1–44, 2011.
- [4] P. Varsta, “Measurement and Analysis of Ice-Induced Stresses in the Shell of an Icebreaker,” Research Report no. 21, Winter Navigation Research Board, Helsinki, Finland, Tech. Rep., 1976, 115 p.
- [5] R. Gagnon, “Analysis of Data from Bergy Bit Impacts Using a Novel Hull-Mounted External Impact Panel,” *Cold Regions Science and Technology*, vol. 52, pp. 50–66, 2008.
- [6] K. Riska, K. Rantala, and A. Joensuu, “Full Scale Observations of Ship-Ice Contact,” 1990/M-97, Helsinki University of Technology, Ship Laboratory, Espoo, Finland, Tech. Rep., 1990.
- [7] St. John, J., and Minnick, P., “Ice Load Impact Study on the NSF RV Nathaniel B. Palmer,” Report no. 376, Ship Structure Committee, Washington, DC, USA, Tech. Rep., 1995, 174 p.
- [8] P. Kujala and J. Vuorio, “Results and Statistical Analysis of Ice Load Measurements On Board Icebreaker Sisu in Winters 1979 to 1985,” Research Report no. 43, Winter Navigation Research Board, Helsinki, Finland, Tech. Rep., 1986, 52 p.
- [9] G. Ghoneim and A. Keinonen, “Full-Scale Impact Tests of CANMAR Kigoriak in Thick Ice,” in *7th International Conference on Port and Ocean Engineering under Arctic Conditions Proceedings*, vol. 3, Espoo, Finland, 1983, pp. 329–346.
- [10] L. Müller and H. Payer, “Loads on Research Vessel Polarstern under Arctic Conditions,” in *9th International Conference on Port and Ocean Engineering under Arctic Conditions Proceedings*, vol. 1, Fairbanks, USA, 1987, pp. 495–508.
- [11] S. Uto, S. Oka, and C. Murakami, “Ice Load Exerted on the Hull of Icebreaker PM Teshio in the South Sea of Okhotsk,” in *18th International Conference on Port and Ocean Engineering under Arctic Conditions Proceedings*, vol. 2, Potsdam, USA, 2005, pp. 683–692.

- [12] B. Leira, L. Børsheim, Ø. Espeland, and J. Amdahl, “Ice-load Estimation for a Ship Hull Based on Continuous Response Monitoring,” in *Proceedings of the Institution of Mechanical Engineers Part M: Journal of Engineering for the Maritime Environment*, vol. 223, 2009, pp. 529–540.
- [13] R. Ritch, R. Frederking, M. Johnston, R. Browne, and F. Ralph, “Local Ice Pressures Measured on a Strain Panel During the CCGS Terry Fox Bergy Bit Impact Study,” *Cold Regions Science and Technology*, vol. 52, pp. 29–49, 2008.
- [14] R. S. Taylor, I. J. Jordaan, C. Li, and D. Sudom, “Local Design Pressures for Structures in Ice: Analysis of Full-Scale Data,” *Journal of Offshore Mechanics and Arctic Engineering*, vol. 132, no. 3, p. 7, 2010.
- [15] F. Ralph, I. Jordaan, and M. Manual, “Application of Upcrossing Rate Methodology to Local Design of Icebreaking Vessels,” in *Arctic Technology Conference*. St. John’s, Canada: Offshore Technology Conference, 2016.
- [16] M. Suominen and P. Kujala, “The Measured Line Load as a Function of the Load Length in the Antarctic Waters,” in *Proceedings of the 23rd International Conference on Port and Ocean Engineering under Arctic Conditions*, Trondheim, Norway, 2015.
- [17] M. Suominen, P. Kujala, J. Romanoff, and H. Remes, “The Effect of the Extension of the Instrumentation on the Measured Ice-induced Load on a Ship Hull,” *Ocean Engineering*, vol. 144, pp. 327–339, 2017.
- [18] J. Vuorio, K. Riska, and P. Varsta, “Long-term Measurements of Ice Pressure and Ice-Induced Stresses on the Icebreaker Sisu in Winter 1978,” Research Report no. 28, Winter Navigation Research Board, Helsinki, Finland, Tech. Rep., 1979, 50 p.
- [19] K. Riska, “Observations of the Line-Like Nature of Ship-Ice Contact,” in *11th International Conference on Port and Ocean Engineering under Arctic Conditions Proceedings*, vol. 2, St. John’s, Canada, 1991, pp. 785–811.
- [20] T. Ikonen, “Inverse Ice-Induced Load Determination on the Hull of an Ice-going Vessel,” Master’s thesis, Aalto University, 2013.
- [21] T. Uhl, “The Inverse Identification Problem and its Technical Application,” *Archive of Applied Mechanics*, vol. 77, pp. 325–337, 2007.
- [22] J. Kaipio and E. Somersalo, *Statistical and Computational Inverse Problems*. New York, NY: Springer-Verlag, 2005.
- [23] A. Tikhonov and V. Arsenin, *Solution of Ill-Posed Problems*. Washington, DC.: Winston and Sons, 1977.
- [24] A.-J. Romppanen, “Inverse Load Sensing Method for Line Load Determination of Beam-Like Structures,” Ph.D. dissertation, Tampere University of Technology, 2008.
- [25] H. Inoue, J. J. Harrigan, and S. R. Reid, “Review of Inverse Analysis for Indirect Measurement of Impact Force,” *Applied Mechanics Reviews*, vol. 54, pp. 503–524, 2001.

-
- [26] J. Kaipio and E. Somersalo, *Statistical and Computational Inverse Problems*. New York, NY: Springer, 2005.
- [27] W. Chai, B. J. Leira, and A. Naess, “Probabilistic Methods for Estimation of the Extreme Value Statistics of Ship Ice Loads,” *Cold Region Science and Technology*, vol. 146, pp. 87–97, 2018.
- [28] M. Lensu, “Short Term Prediction of Ice Loads Experienced by Ice Going Ships,” Laivalaboratorio M 269, Helsinki University of Technology, Espoo, Finland, Tech. Rep., 2002.
- [29] P. Kujala, “On the Statics of Ice Loads on Ship Hull in the Baltic,” Ph.D. dissertation, Helsinki University of Technology, 1994.
- [30] M. Kotilainen, J. Vanhatalo, M. Suominen, and P. Kujala, “Predicting Ice-induced Load Amplitudes on Ship Bow Conditional on Ice Thickness and Ship Speed in the Baltic Sea,” *Cold Regions Science and Technology*, vol. 135, pp. 116–126, 2017.
- [31] T. Sanderson, *Ice Mechanics: Risks to Offshore Structures*. London, UK: Graham and Trotman, 1988.
- [32] I. J. Jordaan, M. A. Maes, P. W. Brown, and I. P. Hermans, “Probabilistic Analysis of Local Ice Pressures,” *Journal of Offshore Mechanics and Arctic Engineering*, vol. 115, pp. 83–89, 1993.
- [33] P. Kujala and S. Arughadhoss, “Statistical Analysis of Ice Crushing Pressures on a Ship’s Hull During Hull-Ice Interaction,” *Cold Regions Science and Technology*, vol. 70, pp. 1–11, 2012.
- [34] C. Li, I. J. Jordaan, and R. S. Taylor, “Estimation of Local Ice Pressure Using Up-Crossing Rate,” *Journal of Offshore Mechanics and Arctic Engineering*, vol. 132, p. 6, 2010.
- [35] M. Manuel, F. Ralph, and I. J. Jordaan, “Using the Event Maximum Method to Further Analyze Full Scale Local Pressure Data,” in *Arctic Technology Conference*. St. John’s, Canada: Offshore Technology Conference, 2016.
- [36] A. C. Palmer, J. P. Dempsey, and D. M. Masterson, “A Revised Ice Pressure-Area Curve and a Fracture Mechanics Explanation,” *Cold Regions Science and Technology*, vol. 56, pp. 73–76, 2009.
- [37] P. Kujala, M. Suominen, and K. Riska, “Statistics of Ice Loads Measured on M/T Uikku in the Baltic,” in *Proceedings of the 20th International Conference on Port and Ocean Engineering under Arctic Conditions*, Luleå, Sweden, 2009.
- [38] M. Suominen, P. Kujala, J. Romanoff, and H. Remes, “Influence of Load Length on Short-Term Ice Load Statistics in Full-Scale,” *Marine Structures*, vol. 52, pp. 153–172, 2017.
- [39] M. Ochi, “Principles of Extreme Value Statistics and their Application,” in *Extreme Loads Response Symposium*. Arlington, USA: The Society of Naval Architects and Marine Engineers, 1981, pp. 15–30.

- [40] M. Suominen and P. Kujala, “Analysis of Short-Term Ice Load Measurements on board MS Kemira During the Winters 1987 and 1988,” Series AM, Aalto University School of Science and Technology, Espoo, Finland, Tech. Rep., 2010.
- [41] P. Kujala and J. Vuorio, “On the Statistical Nature of the Ice-induced Pressures Measure On Board I.B. Sisu,” in *POAC 85 Conference Proceedings*, Narsaruaq, Greenland, 1985, pp. 823–837.
- [42] P. Kujala, M. Kõrgesaar, and J. Kämäräinen, “Evaluation of the Limit Ice Thickness for the Hull of Various Finnish-Swedish Ice Class Vessels Navigating in the Russian Arctic,” in *Proceedings of the 24th International Conference on Port and Ocean Engineering under Arctic Conditions*, Busan, South Korea, 2017.
- [43] “Gumbel Distribution,” [Online], Wikipedia, Accessed: 13.06.2018. [Online]. Available: https://en.wikipedia.org/wiki/Gumbel_distribution
- [44] “Requirements Concerning Polar Class,” IACS Req. 20016/Rev.2 2016, International Association of Classification Societies, London,UK, 2016.
- [45] “Rules for the Classification and Construction of Sea-Going Ships,” Russian Maritime Register of Shipping, St. Petersburg, Russia, 2010.
- [46] “Ice Class Regulations and the Application Thereof,” TRAFI/494131/03.04.01.00/2016, Finnish Transport Safety Agency, Helsinki, Finland, 2017.
- [47] A. M. Kendrick, “Polar Ship Design Standards – State of the Art , and Way Forward,” in *ICETECH 2014*. Banff, Canada: SNAME, 2015, pp. 1–6.
- [48] P. Kujala, F. Goerlandt, B. Way, D. Smith, M. Yang, F. Khan, and B. Veitch, “Review of Risk-Based Design for Ice-Class Ships,” Submitted for publication.
- [49] Y. Popov, O. Faddeyev, D. Kheisin, and A. Yalovlev, *Strength of Ships Sailing in Ice*. Leningrad, USSR: Sudostroenie Publishing House, 1967, technical Translation, U.S. Army Foreign Science and Technology Center, FSTC-HT-23-96-68.
- [50] C. G. Daley, “Energy Based Ice Collision Forces,” in *POAC 1999*, Helsinki, Finland, 1999.
- [51] E. Kim and J. Amdahl, “Discussion of Assumptions Behind Rule-based Ice Loads due to Crushing,” *Ocean Engineering*, vol. 119, pp. 249–261, 2016.
- [52] P. Kujala, “Ice Strengthening Rules,” [Lecture Notes], Aalto University, 2017.
- [53] E. Ranki, “Irtokeulan Paikallisten Jääpaineiden Mittaukset Keväällä 1985 ja Vaurioanalyysi,” Raportti B86, Wärtsilä Arctic Research Center, Helsinki, Finland, Tech. Rep., 1985, 11p., [In Finnish].
- [54] “Baltika, Aker ARC100,” Aker Arctic Technology Oy, Accessed: 02.04.2018. [Online]. Available: <https://akerarctic.fi/en/references/built/baltika-aker-arc-100>
- [55] M. Suominen, A. Bekker, P. Kujala, and R. U. F. Von Bock und Polach, “Full-Scale Measurements On Board PSRV S.A. Agulhas II in the Baltic Sea,” in

-
- Proceedings of the 22nd International Conference on Port and Ocean Engineering under Arctic Conditions*, Espoo, Finland, 2013.
- [56] C. Haas, “Evaluation of Ship-Based Electromagnetic-Inductive Thickness Measurements of Summer Sea-Ice in the Bellingshausen and Amundsen Seas, Antarctica,” *Cold Region Science and Technology*, vol. 27, no. 1, pp. 1–16, 1998.
- [57] “Arctic Ice Charts,” Russian Federation State Scientific Center: Arctic and Antarctic Research Institute, Accessed: 22.02.2018. [Online]. Available: <http://wdc.aari.ru/datasets/d0040/arctic/png/>
- [58] W. F. Weeks and W. D. Hibler, *On Sea Ice*. Fairbanks, AK: University of Alaska Press, 2014.
- [59] Dassault Systèmes, “ABAQUS/CAE 2017,” (2016_09_28-00.54.59 126836) [Computer Software], 2016.
- [60] T. Ikonen, “Determination of Hull Scaling Matrix on the Side Shell of the Oblique Icebreaker,” Internal Report, Aker Arctic Technology Oy, Helsinki, Finland, Tech. Rep., 2014.
- [61] “Hull Ice Load Measuring System on NB 508, Oblique Icebreaker "Baltika",” Technical Documentation, VTT Technical Research Centre of Finland, Helsinki, Finland, Tech. Rep., 2014.
- [62] MathWorks, “MATLAB,” (R2017b) [Computer Software], 2017, Academic License.
- [63] “Global Optimization Toolbox Solver Characteristics,” MathWorks, Accessed: 02.04.2018. [Online]. Available: <https://se.mathworks.com/help/gads/improving-optimization-by-choosing-another-solver.html>
- [64] P. Kujala, “Results of Long-Term Ice Load Measurements On Board Chemical Tanker Kemira In the Baltic Sea During The Winters 1985 to 1988,” Research Report no. 47, Winter Navigation Research Board, Helsinki, Finland, Tech. Rep., 1989, 200p.

Appendix 1: Method Verification Trial Cases

| | |
|---|----|
| Table A1.1: Additional results of the optimisation properties investigation | II |
| Table A1.2: Additional results of the ICM selection investigation | IV |
| Table A1.2: Additional results for Discretisation 1 verification | V |
| Table A1.3: Additional results for Discretisation 2 verification | VI |

Table A1.1: Additional results of the optimisation properties investigation

| | Variable | Input | Iteration 2 | Iteration 3 | Iteration 4 |
|--------|------------------------|--------|----------------|----------------|----------------|
| Case 1 | $h_{1,up}$ [m] | 0.55 | 0.53 | 0.53 | 0.53 |
| | $h_{1,low}$ [m] | 0.35 | 0.35 | 0.35 | 0.35 |
| | p_1 [MPa] | 10.00 | 11.14 | 11.14 | 11.14 |
| | Exit Criteria | – | Step Tolerance | Mesh Tolerance | Mesh Tolerance |
| | $h_1 \cdot p_1$ [kN/m] | 2000.0 | 2008.8 | 2008.8 | 2008.8 |
| Case 2 | $h_{1,up}$ [m] | 0.90 | 0.91 | 0.91 | 0.80 |
| | $h_{1,low}$ [m] | 0.70 | 0.69 | 0.69 | 0.79 |
| | p_1 [MPa] | 2.00 | 1.83 | 1.83 | 49.86 |
| | Exit Criteria | – | Step Tolerance | Mesh Tolerance | Mesh Tolerance |
| | $h_1 \cdot p_1$ [kN/m] | 400.0 | 403.9 | 403.9 | 405.6 |
| Case 3 | $h_{1,up}$ [m] | 0.70 | 0.70 | 0.70 | 0.70 |
| | $h_{1,low}$ [m] | 0.30 | 0.30 | 0.30 | 0.30 |
| | p_1 [MPa] | 5.00 | 5.08 | 5.08 | 5.08 |
| | Exit Criteria | – | Step Tolerance | Mesh Tolerance | Mesh Tolerance |
| | $h_1 \cdot p_1$ [kN/m] | 2000.0 | 1998.7 | 1998.7 | 1998.7 |
| Case 5 | $h_{1,up}$ [m] | 0.35 | 0.40 | 0.40 | 0.40 |
| | $h_{1,low}$ [m] | 0.25 | 0.20 | 0.20 | 0.20 |
| | p_1 [MPa] | 1.00 | 0.50 | 0.50 | 0.50 |
| | Exit Criteria | – | Step Tolerance | Mesh Tolerance | Mesh Tolerance |
| | $h_1 \cdot p_1$ [kN/m] | 100.0 | 98.6 | 98.6 | 98.6 |
| Case 7 | $h_{2,up}$ [m] | -0.35 | -0.36 | -0.36 | -0.36 |
| | $h_{2,low}$ [m] | -0.55 | -0.53 | -0.53 | -0.53 |
| | p_2 [MPa] | 2.00 | 2.38 | 2.38 | 2.38 |
| | Exit Criteria | – | Step Tolerance | Mesh Tolerance | Mesh Tolerance |
| | $h_2 \cdot p_2$ [kN/m] | 400.0 | 407.1 | 407.1 | 407.1 |
| Case 8 | $h_{2,up}$ [m] | -0.45 | -0.39 | -0.39 | -0.39 |
| | $h_{2,low}$ [m] | -0.55 | -0.61 | -0.61 | -0.61 |
| | p_2 [MPa] | 1.00 | 0.47 | 0.47 | 0.47 |
| | Exit Criteria | – | Step Tolerance | Mesh Tolerance | Mesh Tolerance |
| | $h_2 \cdot p_2$ [kN/m] | 100.0 | 102.9 | 102.9 | 102.9 |

| | Variable | Input | Iteration 2 | Iteration 3 | Iteration 4 |
|---------|------------------------|--------|----------------|----------------|----------------|
| Case 9 | $h_{2,up}$ [m] | -0.55 | -0.56 | -0.56 | -0.56 |
| | $h_{2,low}$ [m] | -0.75 | -0.73 | -0.73 | -0.73 |
| | p_2 [MPa] | 5.00 | 5.80 | 5.80 | 5.80 |
| | Exit Criteria | – | Step Tolerance | Mesh Tolerance | Mesh Tolerance |
| | $h_2 \cdot p_2$ [kN/m] | 1000.0 | 981.6 | 981.6 | 981.6 |
| Case 10 | $h_{2,up}$ [m] | -0.80 | -0.74 | -0.74 | -0.74 |
| | $h_{2,low}$ [m] | -0.85 | -0.95 | -0.95 | -0.95 |
| | p_2 [MPa] | 8.00 | 1.89 | 1.89 | 1.89 |
| | Exit Criteria | – | Step Tolerance | Mesh Tolerance | Mesh Tolerance |
| | $h_2 \cdot p_2$ [kN/m] | 400.0 | 401.7 | 401.7 | 401.7 |

Table A1.2: Additional results of the ICM selection investigation

| | Variable | Input | Mesh 1 | Mesh 2 | Mesh 3 | Mesh 4 |
|---------|------------------------|--------|--------|--------|--------|--------|
| Case 2 | $h_{1,up}$ [m] | 0.90 | 0.90 | 0.90 | 0.90 | 0.90 |
| | $h_{1,low}$ [m] | 0.70 | 0.70 | 0.70 | 0.70 | 0.70 |
| | p_1 [MPa] | 2.00 | 2.02 | 2.02 | 2.02 | 2.02 |
| | $h_1 \cdot p_1$ [kN/m] | 400.0 | 404.7 | 404.5 | 404.1 | 404.6 |
| Case 3 | $h_{1,up}$ [m] | 0.70 | 0.70 | 0.70 | 0.70 | 0.70 |
| | $h_{1,low}$ [m] | 0.30 | 0.30 | 0.30 | 0.30 | 0.30 |
| | p_1 [MPa] | 5.00 | 5.08 | 5.08 | 5.06 | 5.08 |
| | $h_1 \cdot p_1$ [kN/m] | 2000.0 | 1999.1 | 1998.7 | 1997.0 | 1996.8 |
| Case 4 | $h_{1,up}$ [m] | 0.50 | 0.53 | 0.53 | 0.51 | 0.52 |
| | $h_{1,low}$ [m] | 0.45 | 0.39 | 0.40 | 0.42 | 0.41 |
| | p_1 [MPa] | 10.00 | 3.63 | 3.82 | 5.34 | 4.45 |
| | $h_1 \cdot p_1$ [kN/m] | 500.0 | 503.8 | 503.9 | 504.4 | 505.1 |
| Case 5 | $h_{1,up}$ [m] | 0.35 | 0.40 | 0.49 | 0.39 | 0.40 |
| | $h_{1,low}$ [m] | 0.25 | 0.20 | 0.05 | 0.21 | 0.21 |
| | p_1 [MPa] | 1.00 | 0.49 | 0.26 | 0.53 | 0.51 |
| | $h_1 \cdot p_1$ [kN/m] | 100.0 | 98.4 | 114.9 | 99.3 | 98.9 |
| Case 7 | $h_{2,up}$ [m] | -0.35 | -0.36 | -0.36 | -0.36 | -0.36 |
| | $h_{2,low}$ [m] | -0.55 | -0.53 | -0.53 | -0.53 | -0.53 |
| | p_2 [MPa] | 2.00 | 2.39 | 2.38 | 2.47 | 2.36 |
| | $h_2 \cdot p_2$ [kN/m] | 400.0 | 407.5 | 407.2 | 404.5 | 405.6 |
| Case 8 | $h_{2,up}$ [m] | -0.45 | -0.39 | -0.39 | -0.40 | -0.39 |
| | $h_{2,low}$ [m] | -0.55 | -0.61 | -0.61 | -0.60 | -0.61 |
| | p_2 [MPa] | 1.00 | 0.47 | 0.47 | 0.53 | 0.47 |
| | $h_2 \cdot p_2$ [kN/m] | 100.0 | 102.7 | 102.9 | 103.2 | 103.9 |
| Case 9 | $h_{2,up}$ [m] | -0.55 | -0.56 | -0.56 | -0.56 | -0.56 |
| | $h_{2,low}$ [m] | -0.75 | -0.73 | -0.73 | -0.73 | -0.73 |
| | p_2 [MPa] | 5.00 | 5.80 | 5.80 | 5.78 | 5.80 |
| | $h_2 \cdot p_2$ [kN/m] | 1000.0 | 981.9 | 981.5 | 980.5 | 980.6 |
| Case 10 | $h_{2,up}$ [m] | -0.80 | -0.75 | -0.75 | -0.75 | -0.75 |
| | $h_{2,low}$ [m] | -0.85 | -0.90 | -0.90 | -0.90 | -0.90 |
| | p_2 [MPa] | 8.00 | 2.78 | 2.79 | 2.82 | 2.83 |
| | $h_2 \cdot p_2$ [kN/m] | 400.0 | 415.5 | 415.4 | 414.3 | 0.0 |

Table A1.2: Additional results for Discretisation 1 verification

| Variable | Trial 5 | | Trial 6 | | Trial 7 | | Trial 8 | | Trial 9 | | Trial 10 | |
|--------------------|---------|--------|---------|--------|---------|--------|---------|--------|---------|--------|----------|--------|
| | Input | Result | Input | Result |
| $h_{j,up}$ [m] | 0.55 | 0.53 | 0.90 | 0.90 | 0.70 | 0.70 | 0.35 | 0.39 | -0.05 | -0.05 | -0.35 | -0.36 |
| $h_{j,low}$ [m] | 0.35 | 0.356 | 0.70 | 0.70 | 0.30 | 0.30 | 0.25 | 0.21 | -0.15 | -0.16 | -0.55 | -0.53 |
| p [MPa] | 10.00 | 11.46 | 2.00 | 2.02 | 5.00 | 5.06 | 1.00 | 0.53 | 10.00 | 8.48 | 2.00 | 2.47 |
| $h \cdot p$ [kN/m] | 2000.0 | 2003.6 | 400.0 | 404.1 | 2000.0 | 1997.0 | 100.0 | 99.3 | 1000.0 | 941.0 | 400.0 | 404.5 |

| Variable | Trial 11 | | Trial 12 | | Trial 13 | | Trial 14 | | Trial 15 | |
|--------------------|----------|--------|----------|--------|----------|--------|----------|--------|----------|--------|
| | Input | Result |
| $h_{j,up}$ [m] | -0.45 | -0.40 | -0.80 | -0.75 | 0.30 | 0.37 | -0.40 | -0.41 | 0.15 | 0.20 |
| $h_{j,low}$ [m] | -0.55 | -0.60 | -0.85 | -0.90 | 0.25 | 0.17 | -0.45 | -0.43 | 0.10 | 0.10 |
| p [MPa] | 1.00 | 0.53 | 8.00 | 2.82 | 1.50 | 0.36 | 5.50 | 13.97 | 2.50 | 1.11 |
| $h \cdot p$ [kN/m] | 100.0 | 103.2 | 400.0 | 414.3 | 75.0 | 75.9 | 275.0 | 290.6 | 125.0 | 110.7 |

Table A1.3: Additional results for Discretisation 2 verification

| Variable | Trial 5 | | Trial 6 | | Trial 7 | | Trial 8 | | Trial 9 | |
|-----------------------------|---------|--------|---------|--------|---------|--------|---------|--------|---------|--------|
| | Input | Result |
| $h_{j,up}$ [m] | 0.25 | 0.26 | 0.60 | 0.71 | -0.35 | -0.41 | -0.65 | -0.66 | -0.35 | -0.365 |
| $h_{j,low}$ [m] | 0.20 | 0.16 | 0.45 | 0.37 | -0.50 | -0.46 | -0.75 | -0.71 | -0.55 | -0.529 |
| $p_{\#59}$ [MPa] | 2.00 | 1.01 | 15.00 | 6.17 | 2.30 | 6.40 | 0.80 | 2.92 | 2.00 | 2.52 |
| p_{pt} [MPa] | 3.33 | 1.49 | 7.50 | 4.78 | 0.90 | 2.03 | 4.50 | 7.22 | 2.00 | 2.57 |
| $p_{\#59.5}$ [MPa] | 2.00 | 1.04 | 15.00 | 5.48 | 2.30 | 6.38 | 0.80 | 2.96 | 2.00 | 2.59 |
| $h \cdot p_{fr,avg}$ [kN/m] | 100 | 112 | 2250 | 1977 | 345 | 365 | 80 | 139 | 400 | 419 |
| $h \cdot p_{pt}$ [kN/m] | 167 | 162 | 1125 | 1623 | 135 | 116 | 450 | 342 | 400 | 421 |
| $p_{fr,av}/p_{pt}$ [-] | 0.60 | 0.69 | 2.00 | 1.22 | 2.56 | 3.14 | 0.18 | 0.41 | 1.00 | 1.00 |

Appendix 2: Additional Sample Loading Events

List of Figures in Appendix 2

| | |
|--|------|
| Figure A2.1: Sample load patches for Loading Event 5 | II |
| Figure A2.2: Relevant time histories for Loading Event 5 | II |
| Figure A2.3: Sample load patches for Loading Event 14 | III |
| Figure A2.4: Relevant time histories for Loading Event 14 | III |
| Figure A2.5: Sample load patches for Loading Event 19..... | IV |
| Figure A2.6: Relevant time histories for Loading Event 19 | IV |
| Figure A2.7: Sample load patches for Loading Event 23 | V |
| Figure A2.8: Relevant time histories for Loading Event 23 | V |
| Figure A2.9: Sample load patches for Loading Event 26 | VI |
| Figure A2.10: Relevant time histories for Loading Event 26 | VI |
| Figure A2.11: Sample load patches for Loading Event 28 | VII |
| Figure A2.12: Relevant time histories for Loading Event 28 | VII |
| Figure A2.13: Sample load patches for Loading Event 38 | VIII |
| Figure A2.14: Relevant time histories for Loading Event 38 | VIII |
| Figure A2.15: Sample load patches for Loading Event 40 | IX |
| Figure A2.16: Relevant time histories for Loading Event 40 | IX |
| Figure A2.17: Sample load patches for Loading Event 46 | X |
| Figure A2.18: Relevant time histories for Loading Event 46 | X |
| Figure A2.19: Sample load patches for Loading Event 51 | XI |
| Figure A2.20: Relevant time histories for Loading Event 51 | XI |
| Figure A2.21: Sample load patches for Loading Event 64 | XII |
| Figure A2.22: Relevant time histories for Loading Event 64 | XII |
| Figure A2.23: Sample load patches for Loading Event 69 | XIII |
| Figure A2.24: Relevant time histories for Loading Event 69 | XIII |
| Figure A2.25: Sample load patches for Loading Event 71 | XIV |
| Figure A2.26: Relevant time histories for Loading Event 71 | XIV |
| Figure A2.25: Sample load patches for Loading Event 79 | XV |
| Figure A2.26: Relevant time histories for Loading Event 79 | XV |
| Figure A2.29: Sample load patches for Loading Event 80 | XVI |
| Figure A2.30: Relevant time histories for Loading Event 80 | XVI |

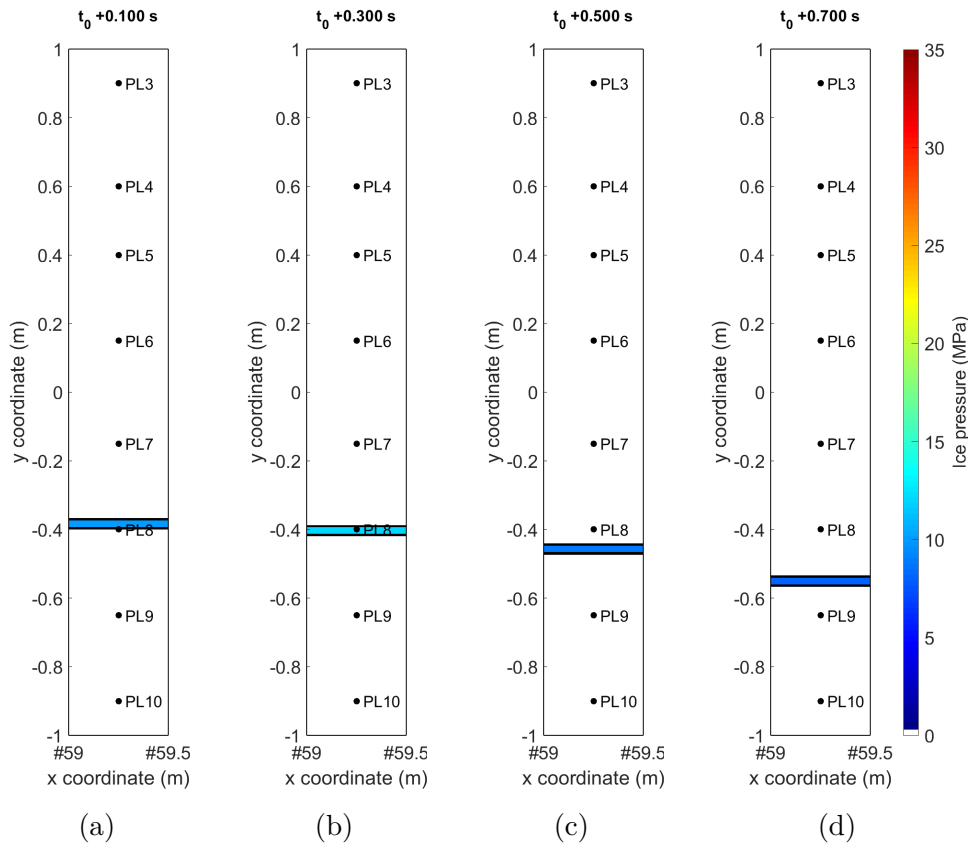


Figure A2.1: Sample load patches for Loading Event 5

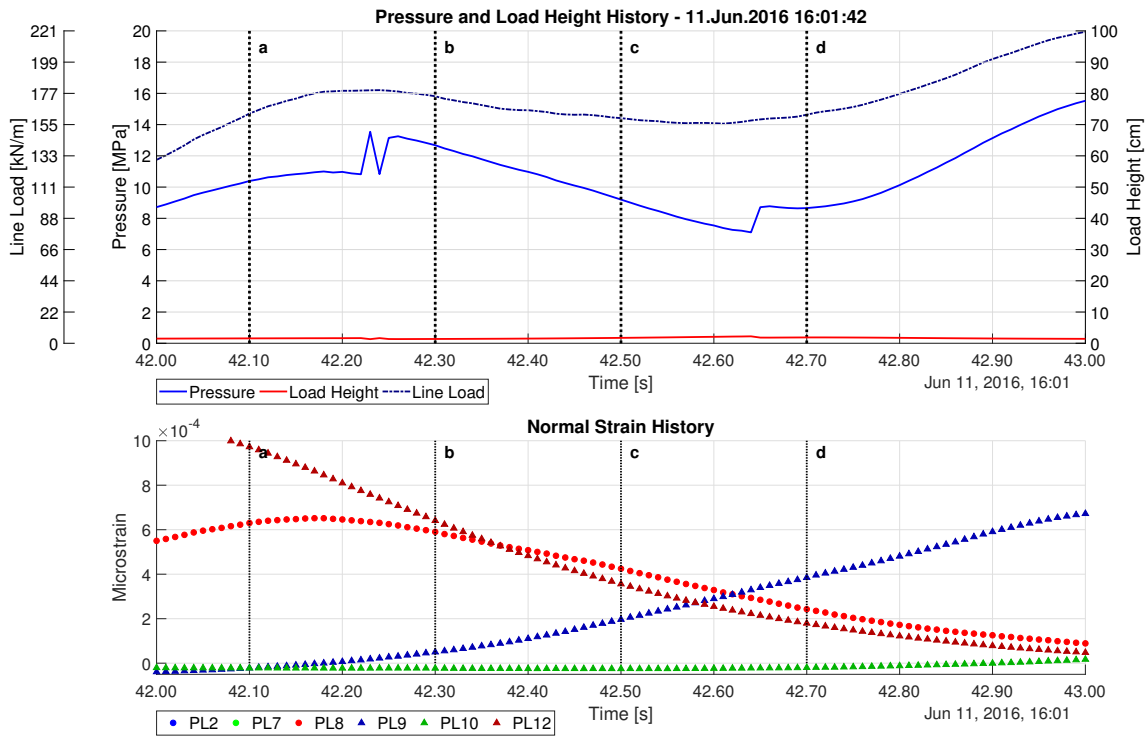


Figure A2.2: Relevant time histories for Loading Event 5

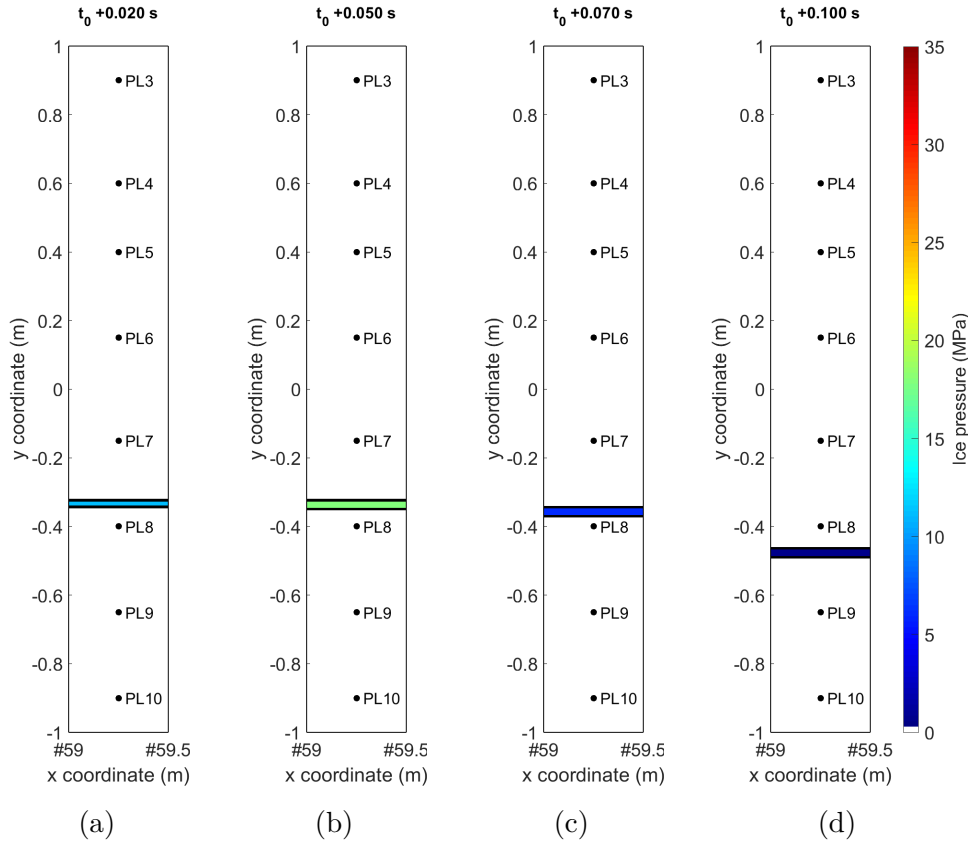


Figure A2.3: Sample load patches for Loading Event 14

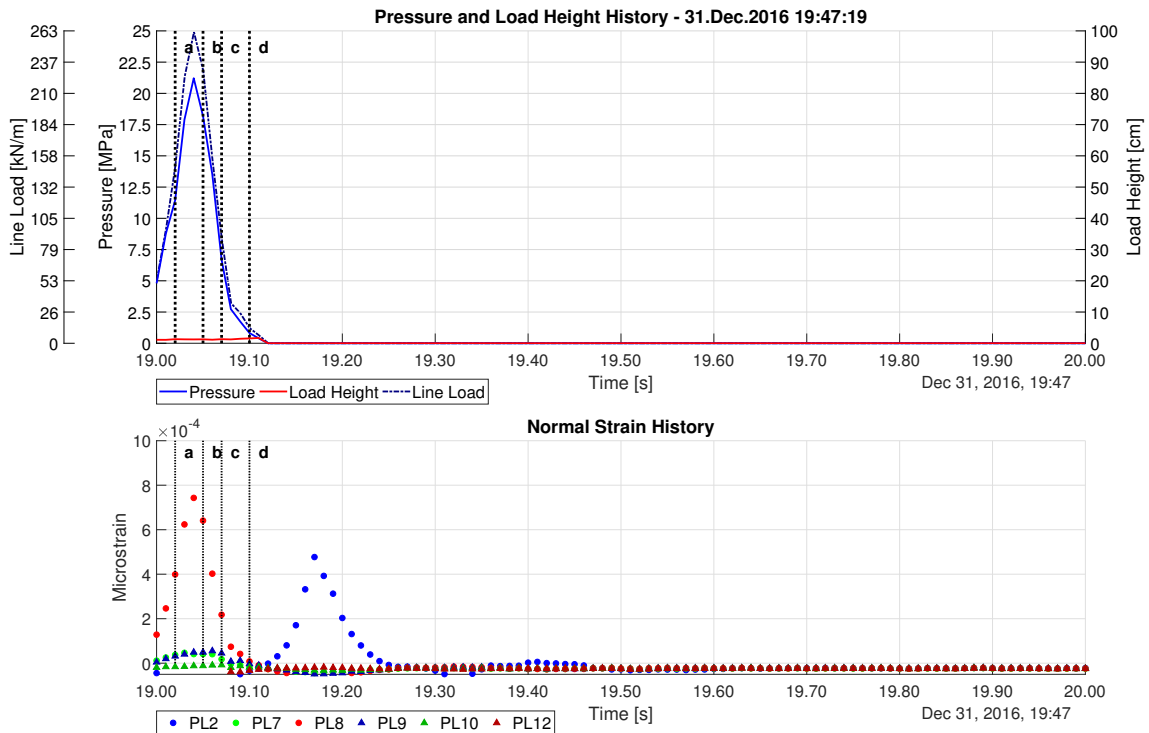


Figure A2.4: Relevant time histories for Loading Event 14

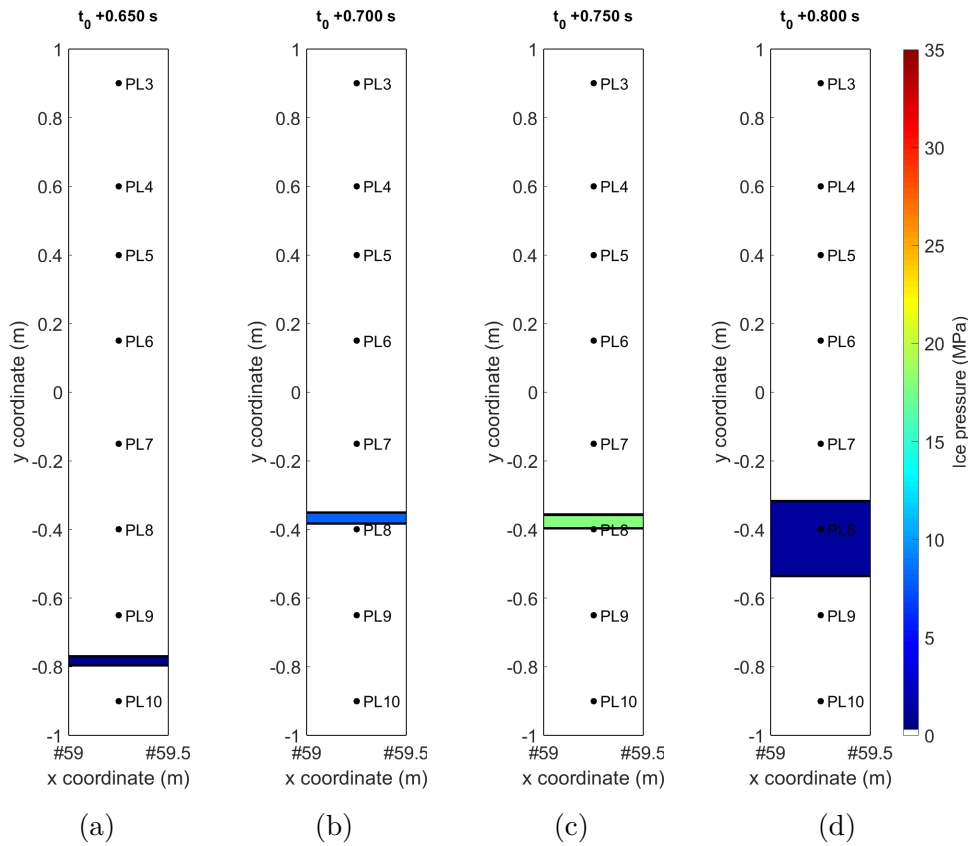


Figure A2.5: Sample load patches for Loading Event 19

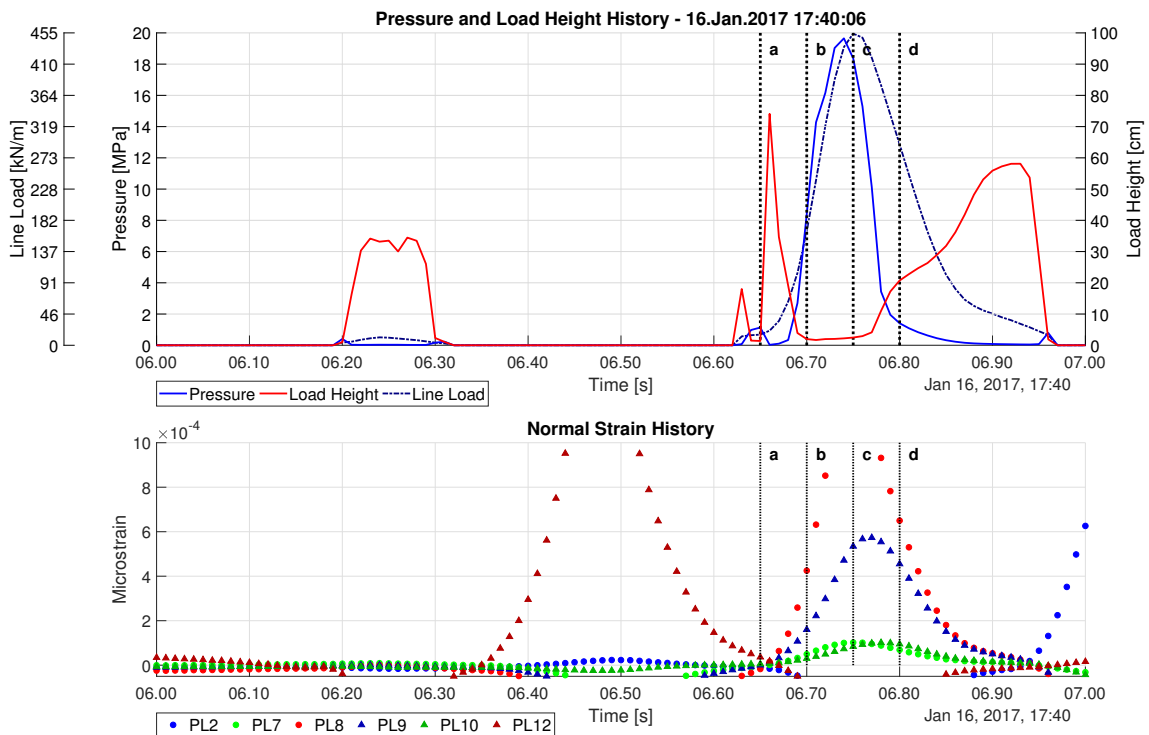


Figure A2.6: Relevant time histories for Loading Event 19

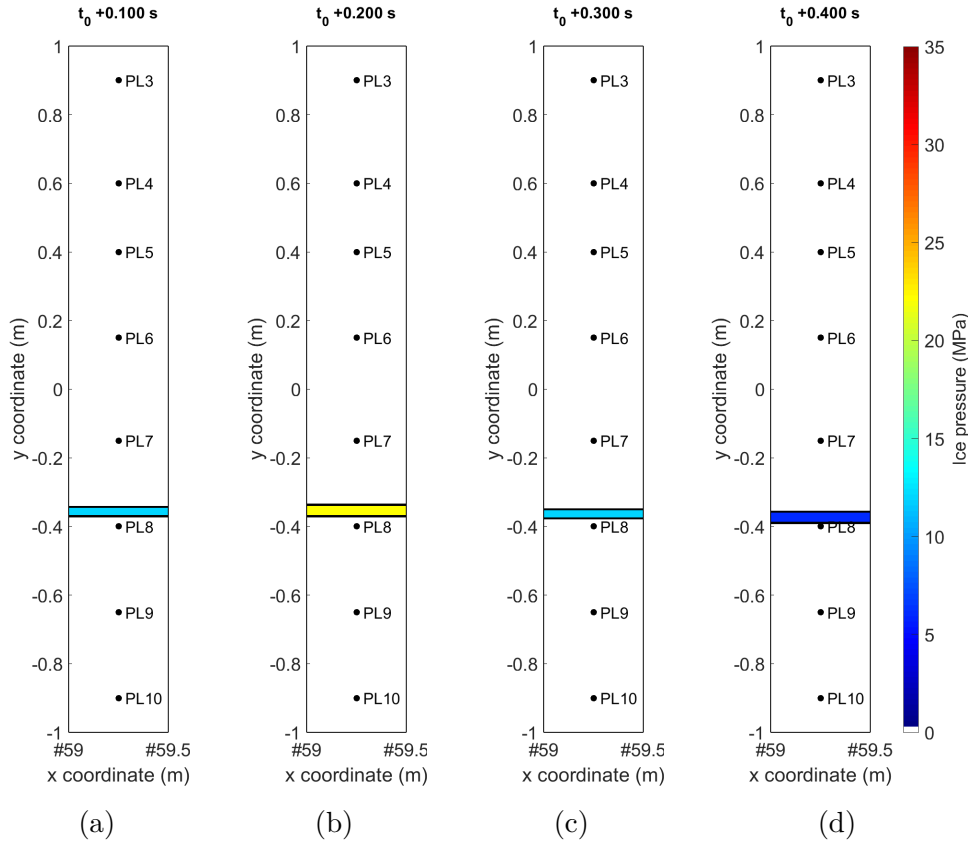


Figure A2.7: Sample load patches for Loading Event 23

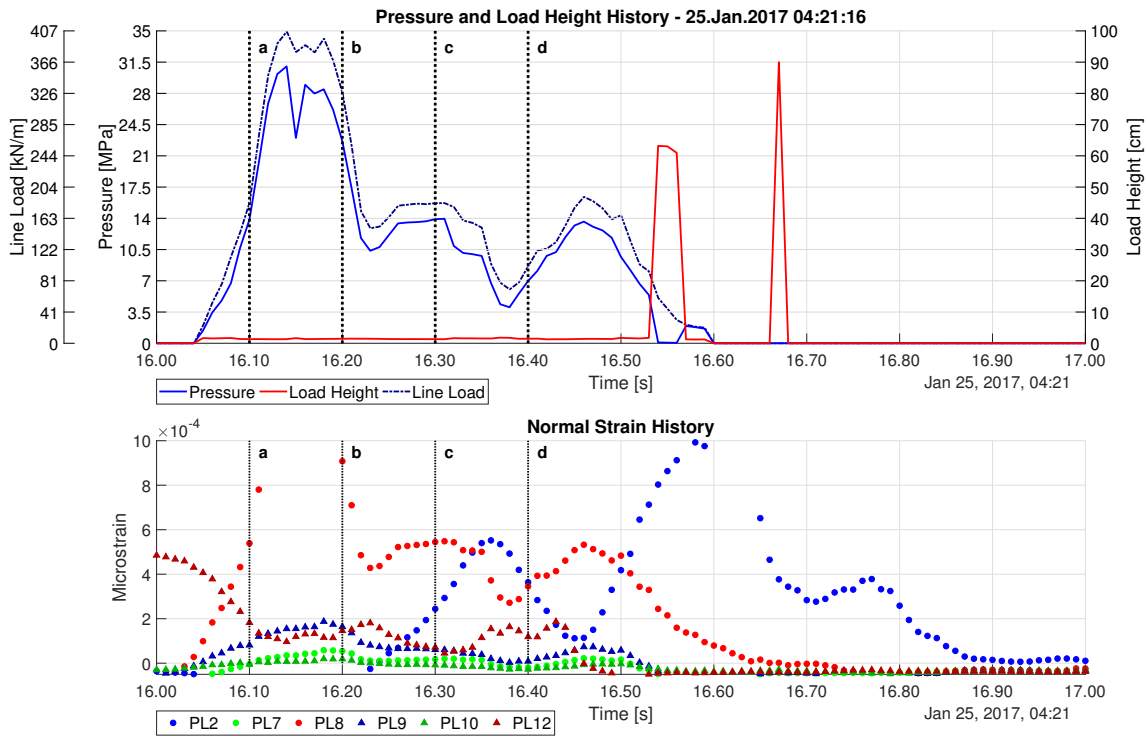


Figure A2.8: Relevant time histories for Loading Event 23

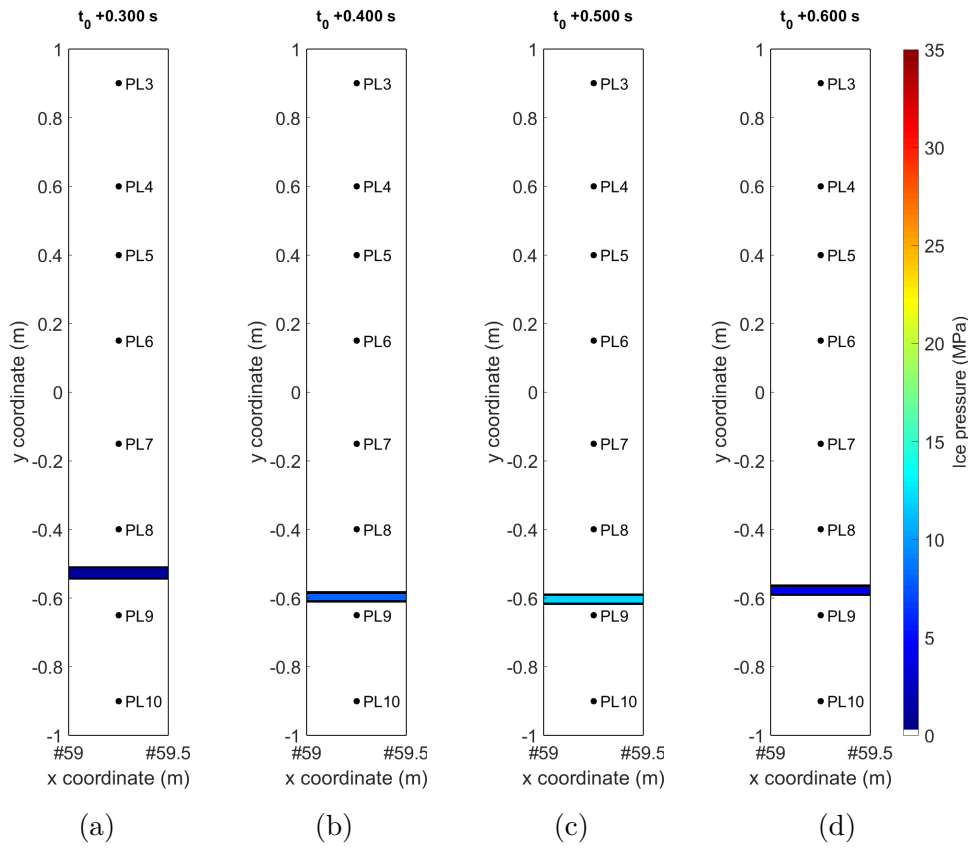


Figure A2.9: Sample load patches for Loading Event 26

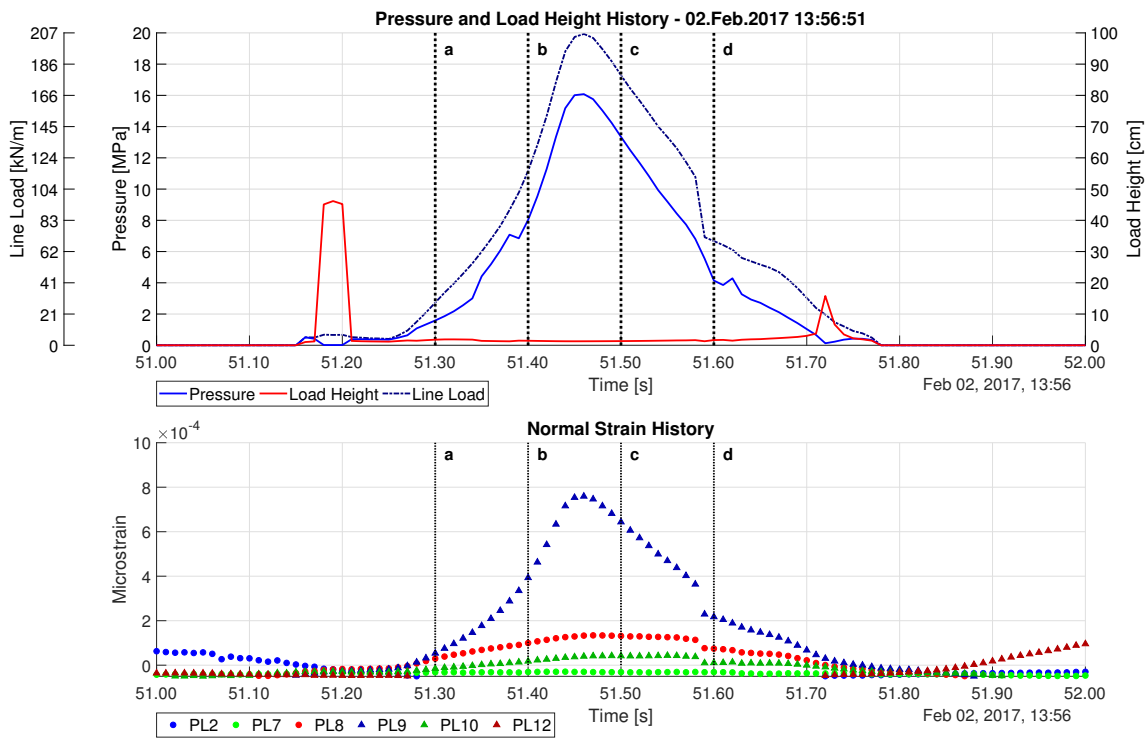


Figure A2.10: Relevant time histories for Loading Event 26

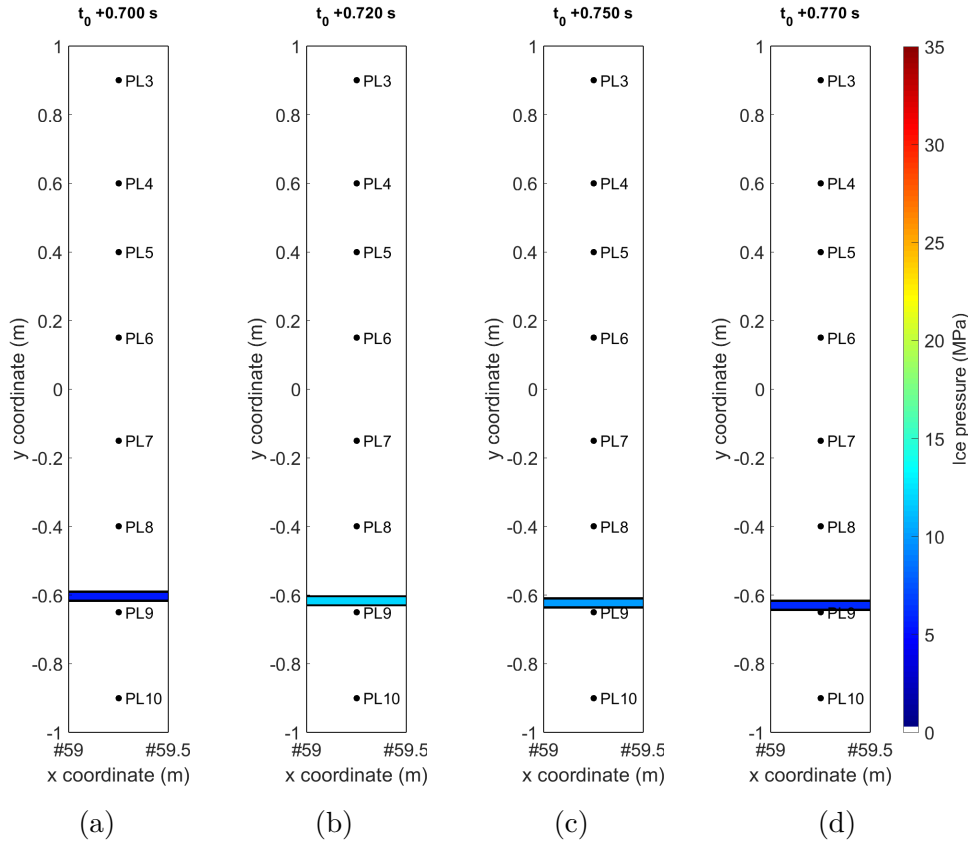


Figure A2.11: Sample load patches for Loading Event 28

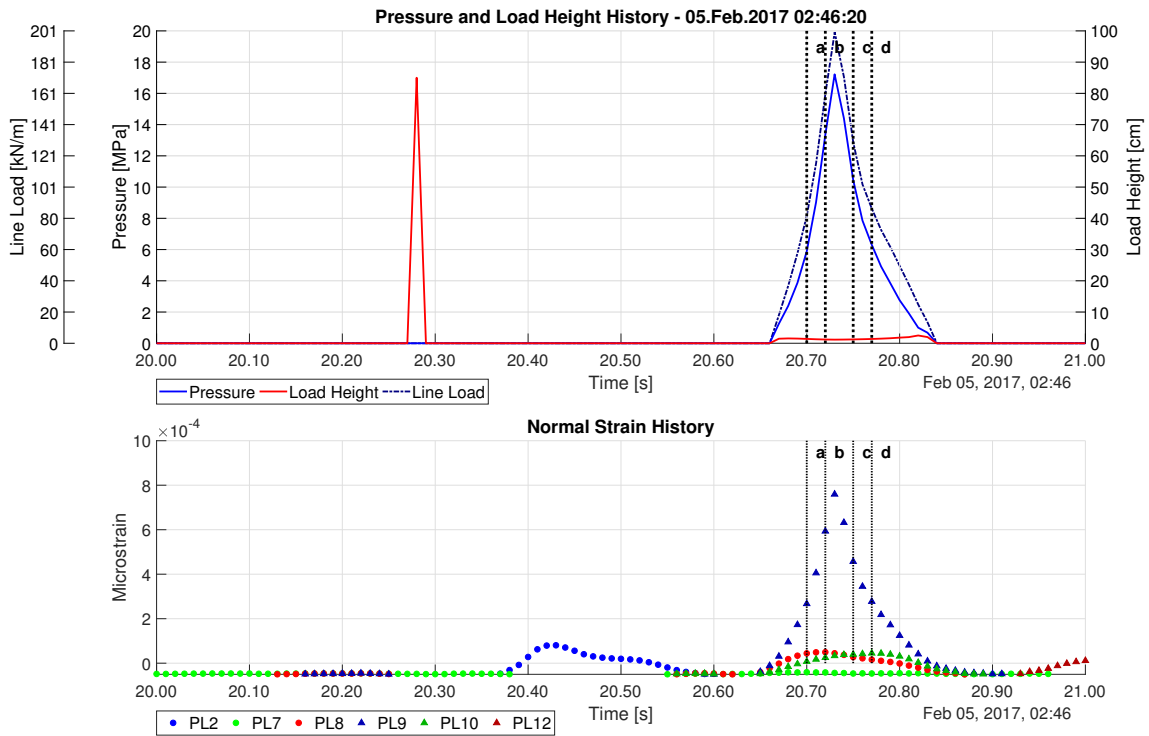


Figure A2.12: Relevant time histories for Loading Event 28

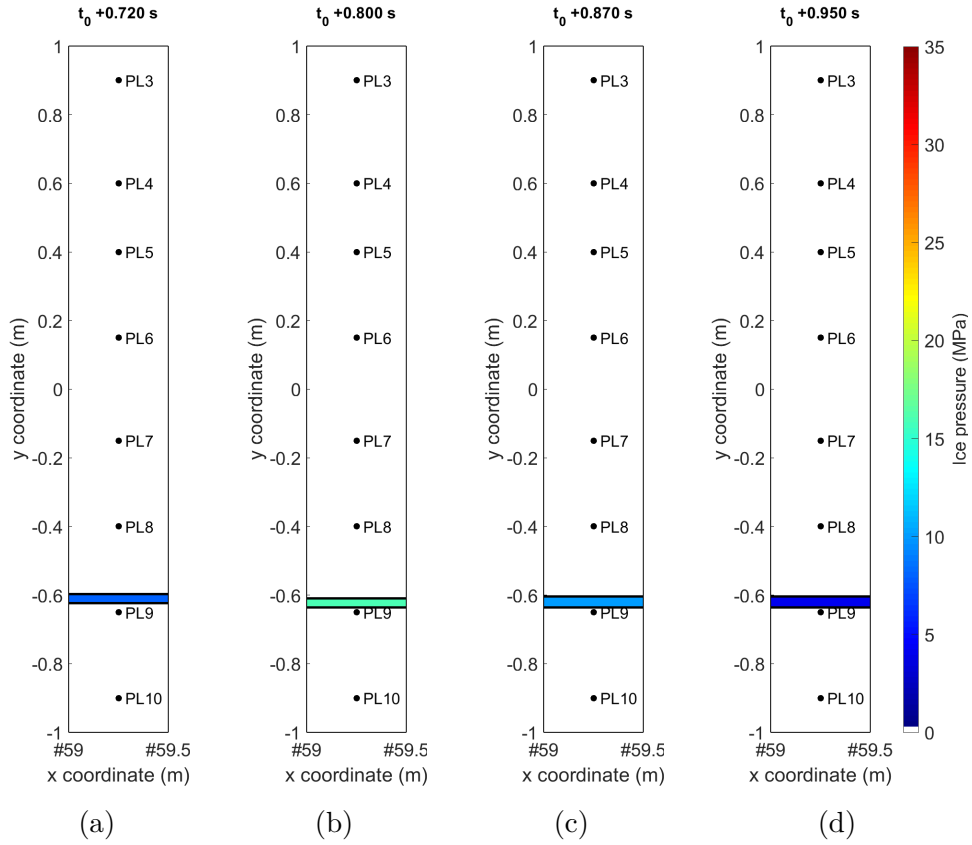


Figure A2.13: Sample load patches for Loading Event 38

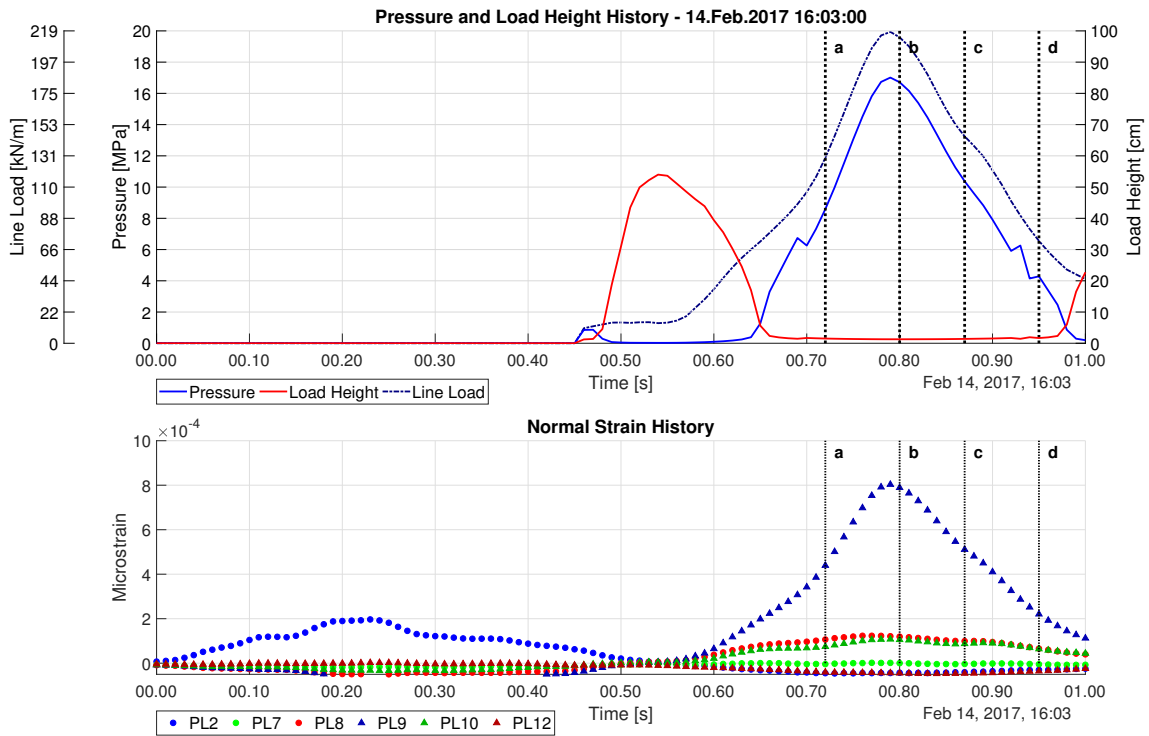


Figure A2.14: Relevant time histories for Loading Event 38

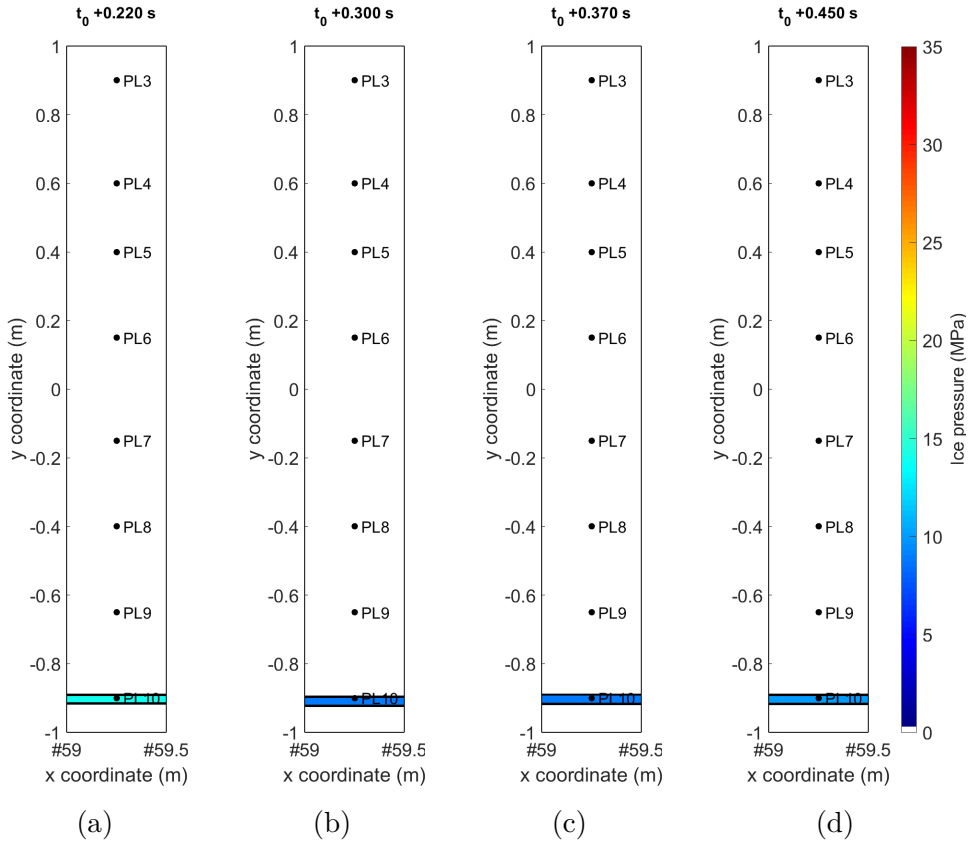


Figure A2.15: Sample load patches for Loading Event 40

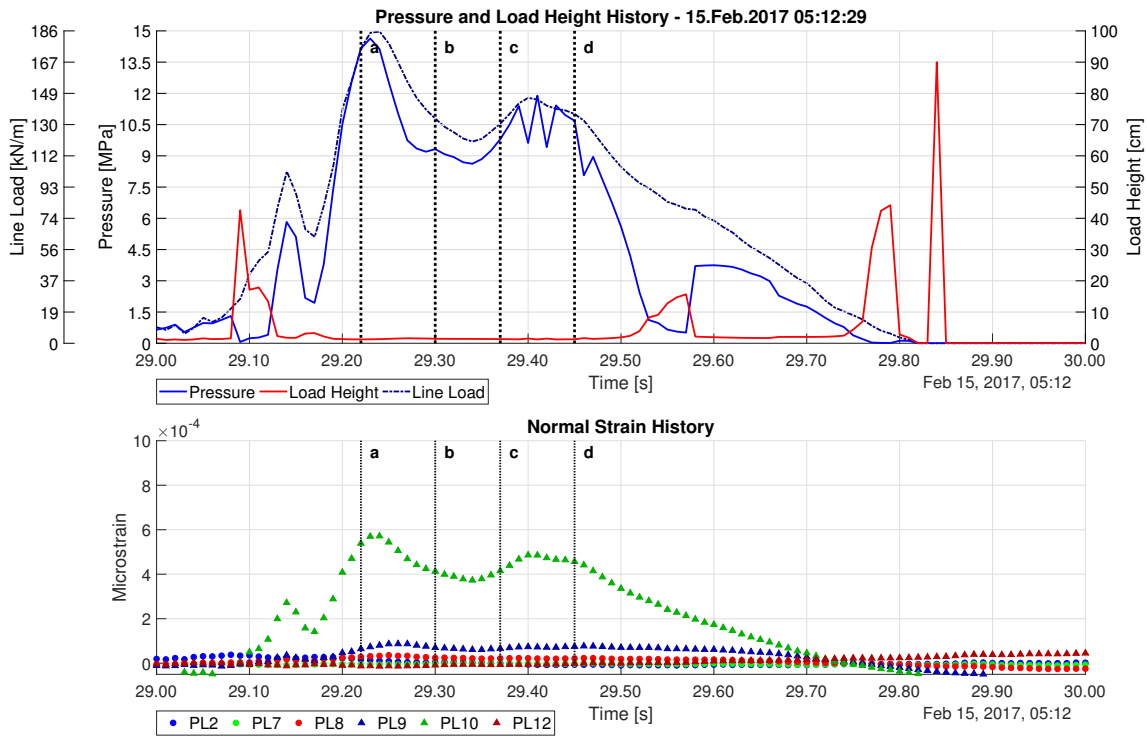


Figure A2.16: Relevant time histories for Loading Event 40

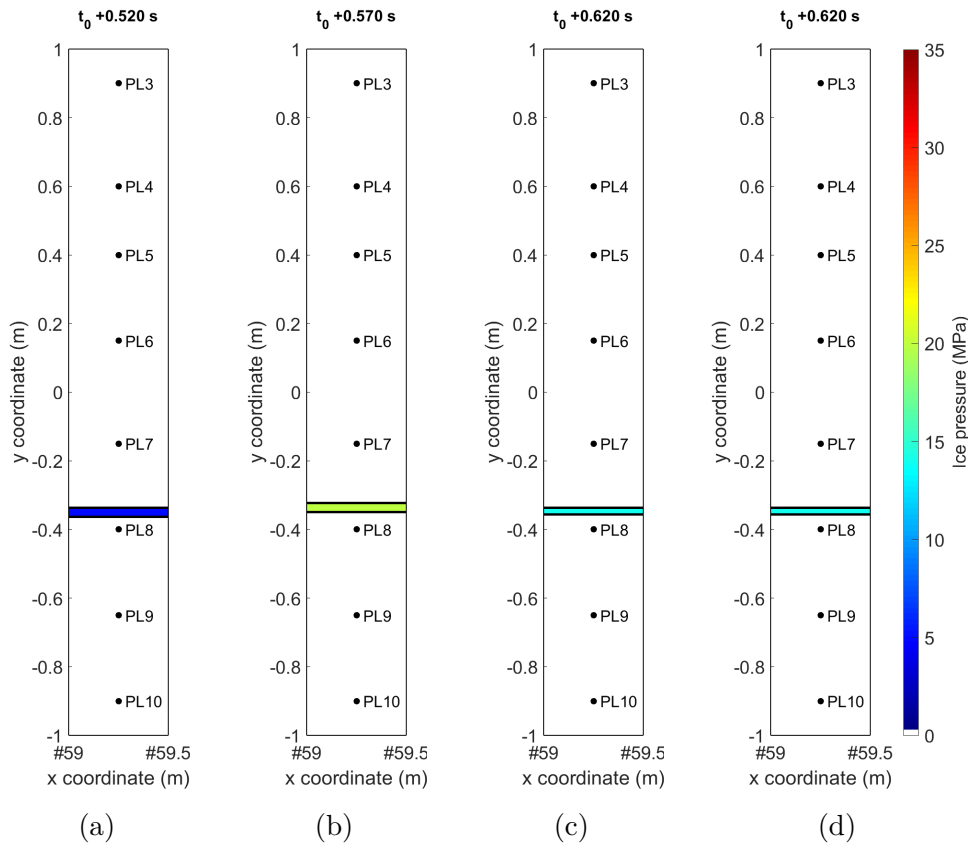


Figure A2.17: Sample load patches for Loading Event 46

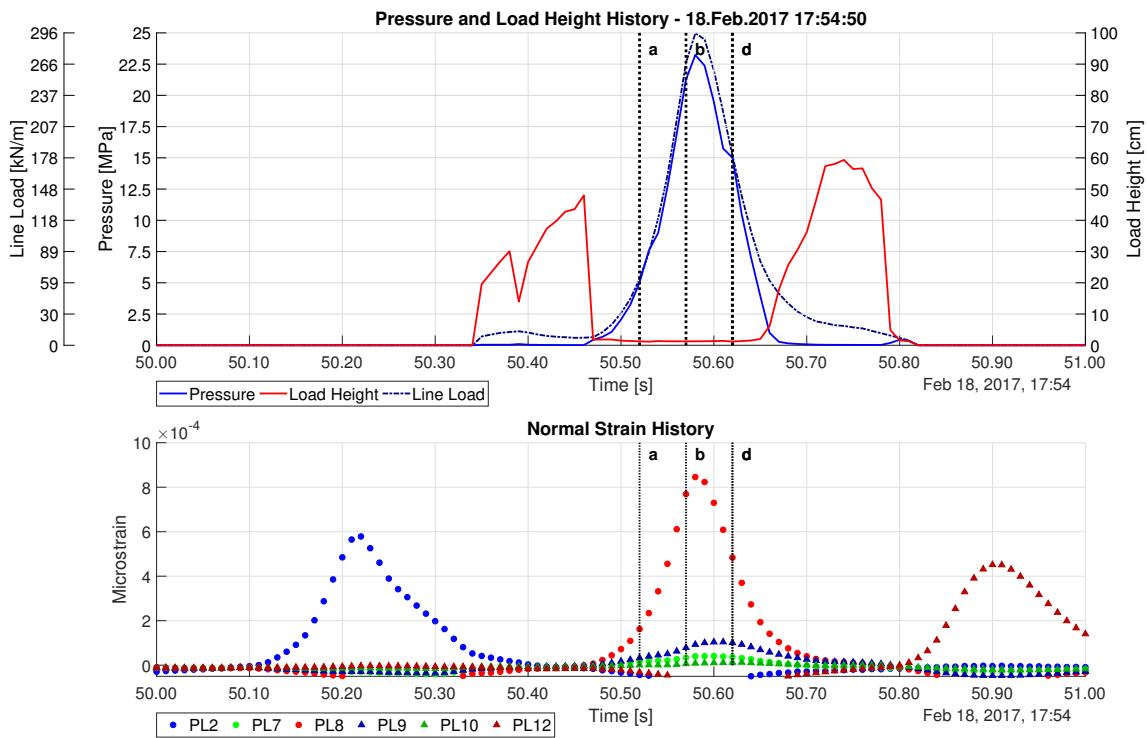


Figure A2.18: Relevant time histories for Loading Event 46

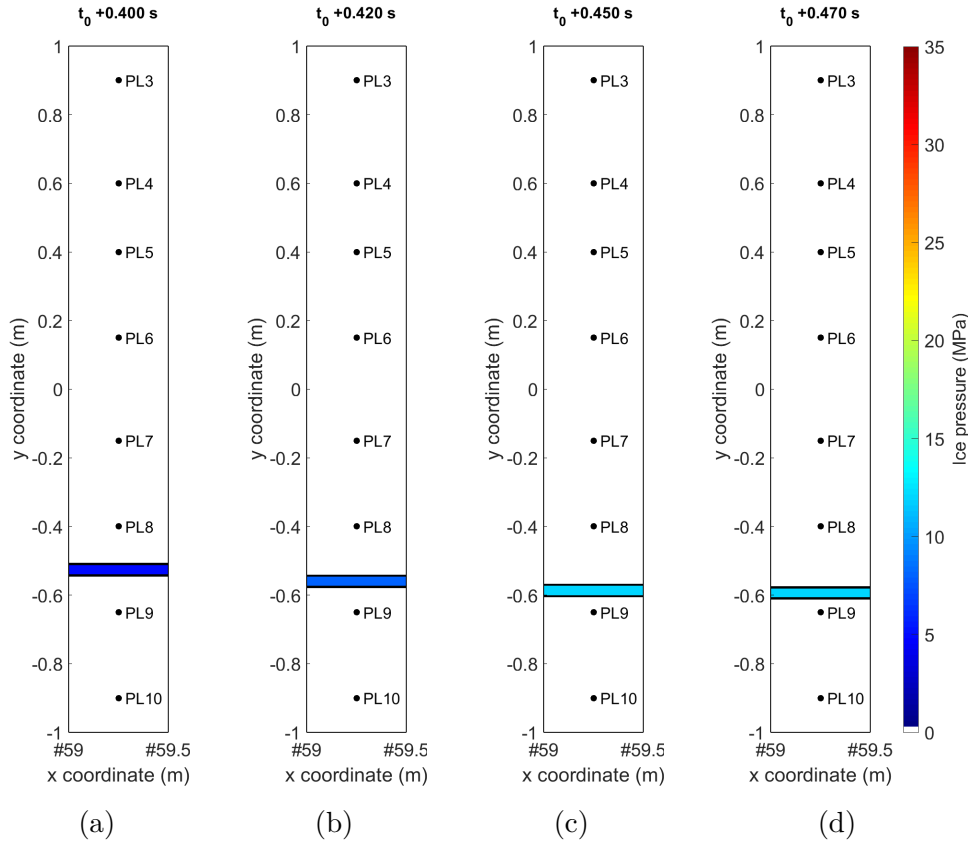


Figure A2.19: Sample load patches for Loading Event 51

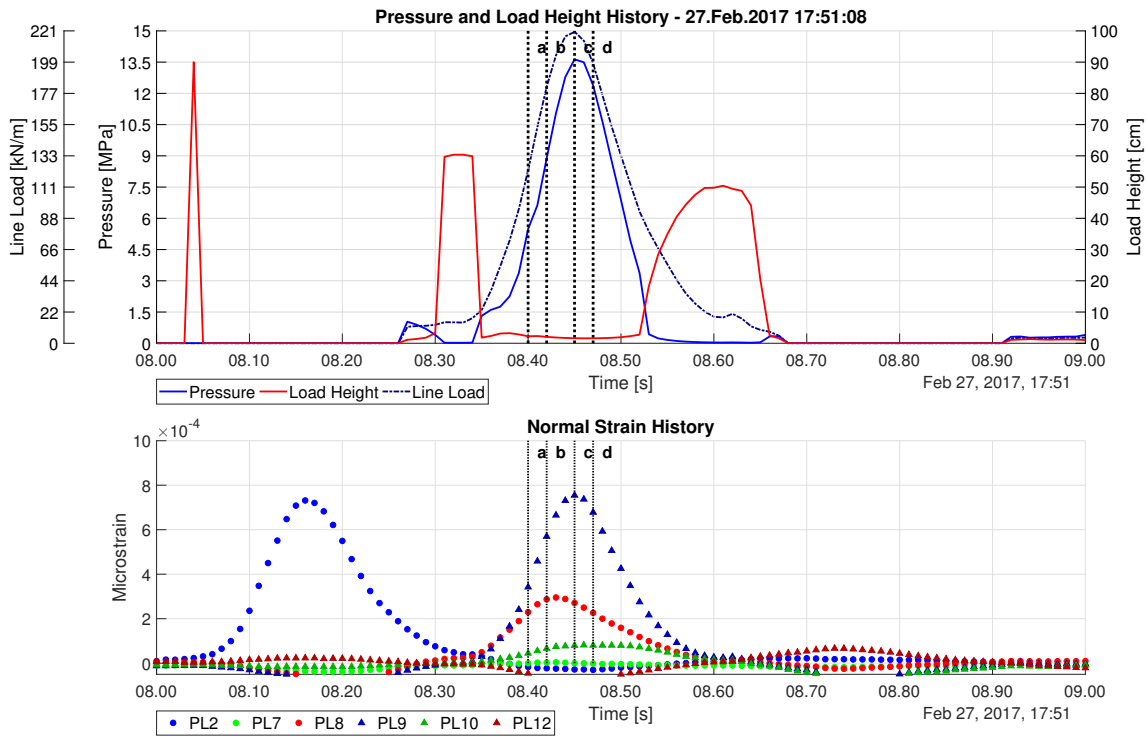


Figure A2.20: Relevant time histories for Loading Event 51

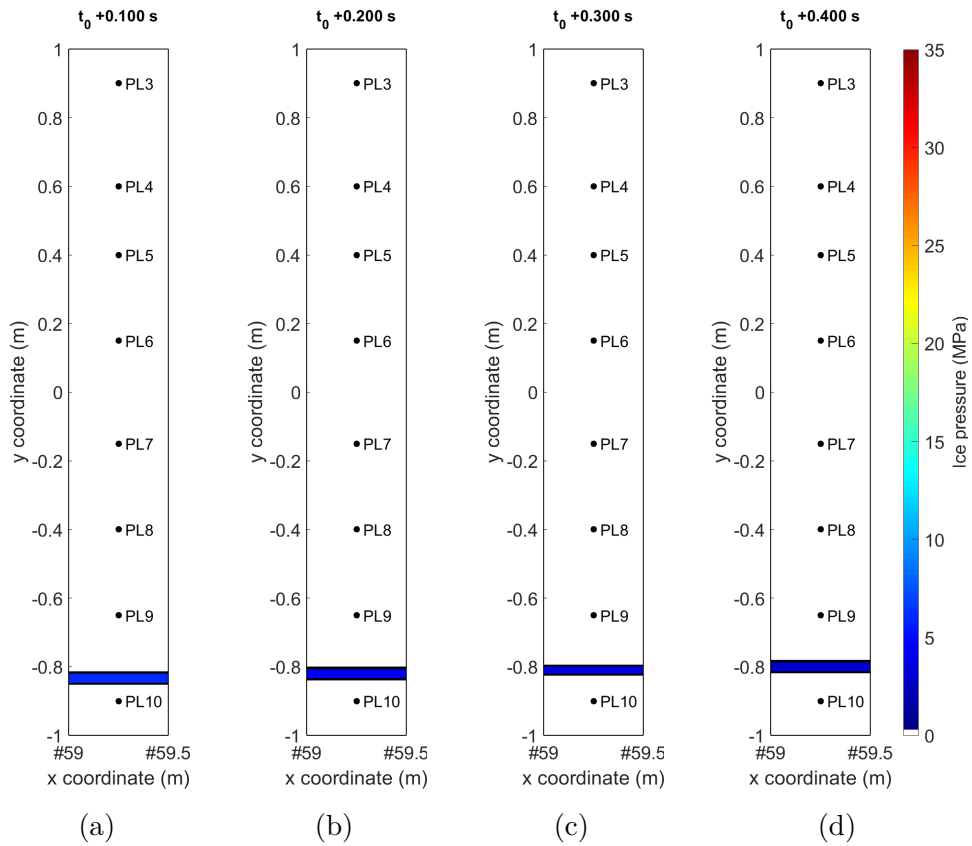


Figure A2.21: Sample load patches for Loading Event 64

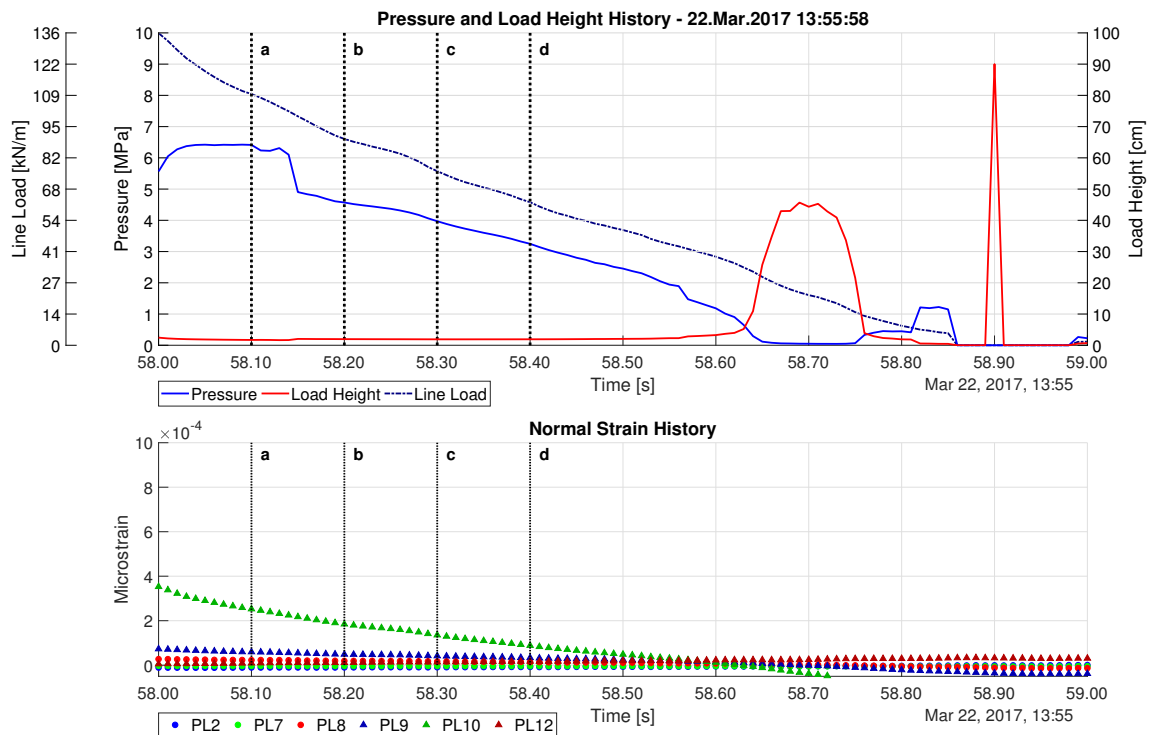


Figure A2.22: Relevant time histories for Loading Event 64

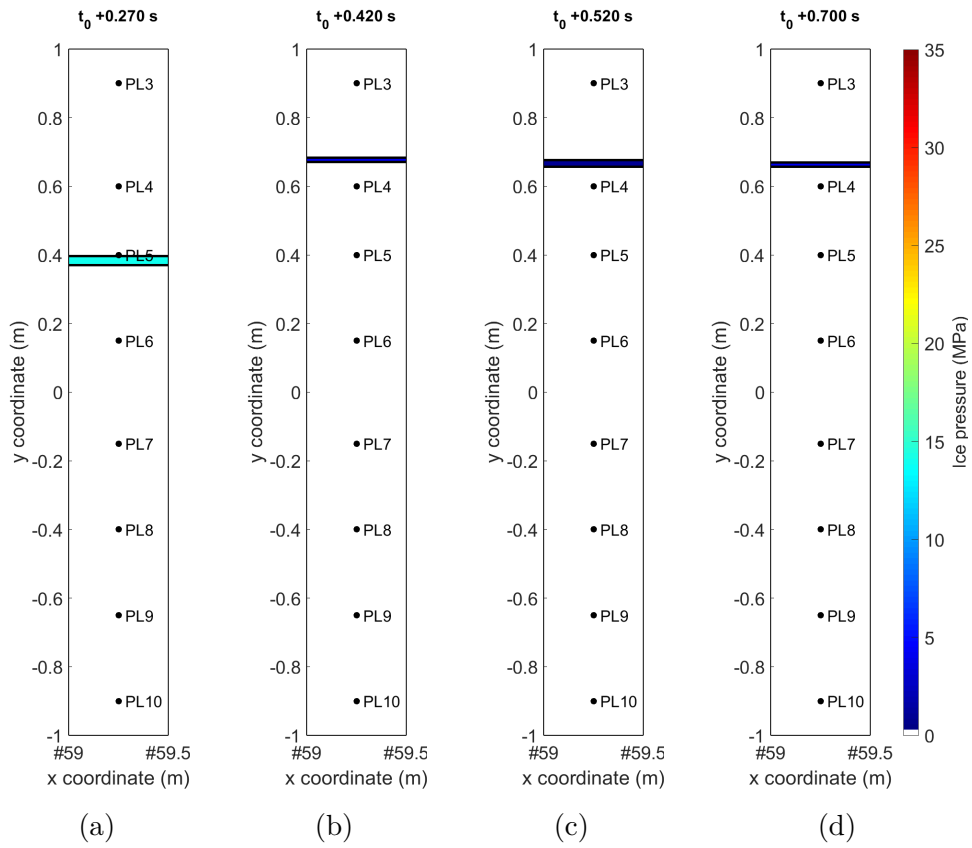


Figure A2.23: Sample load patches for Loading Event 69

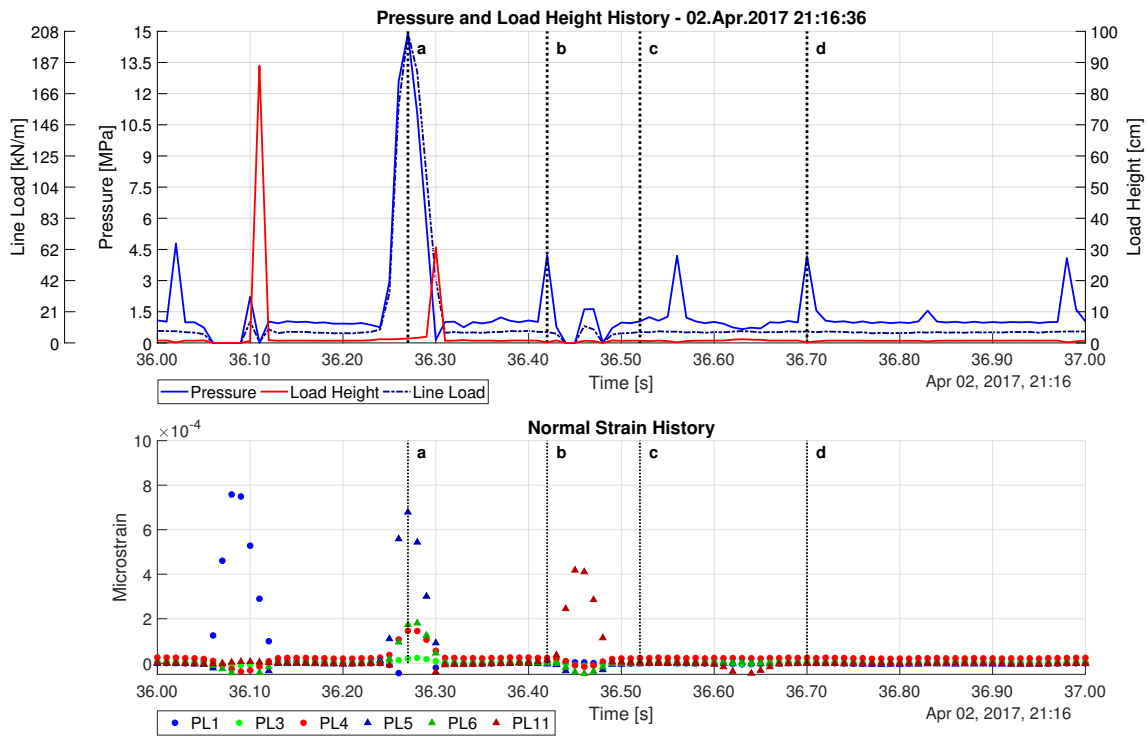


Figure A2.24: Relevant time histories for Loading Event 69

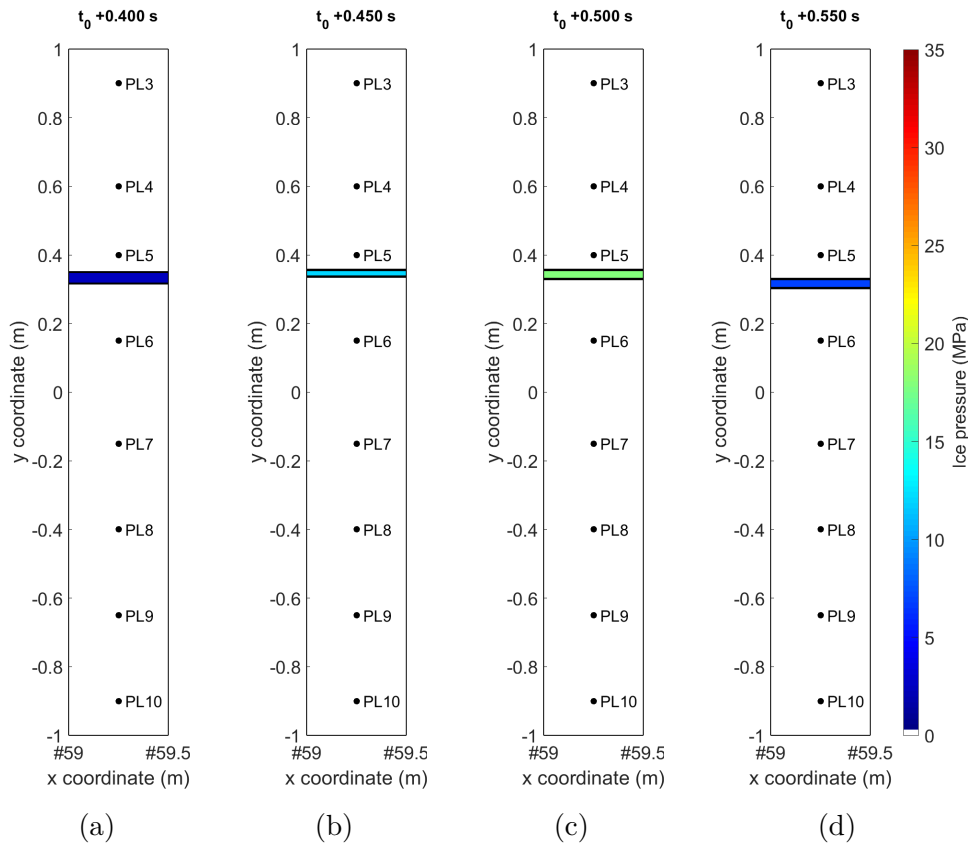


Figure A2.25: Sample load patches for Loading Event 71

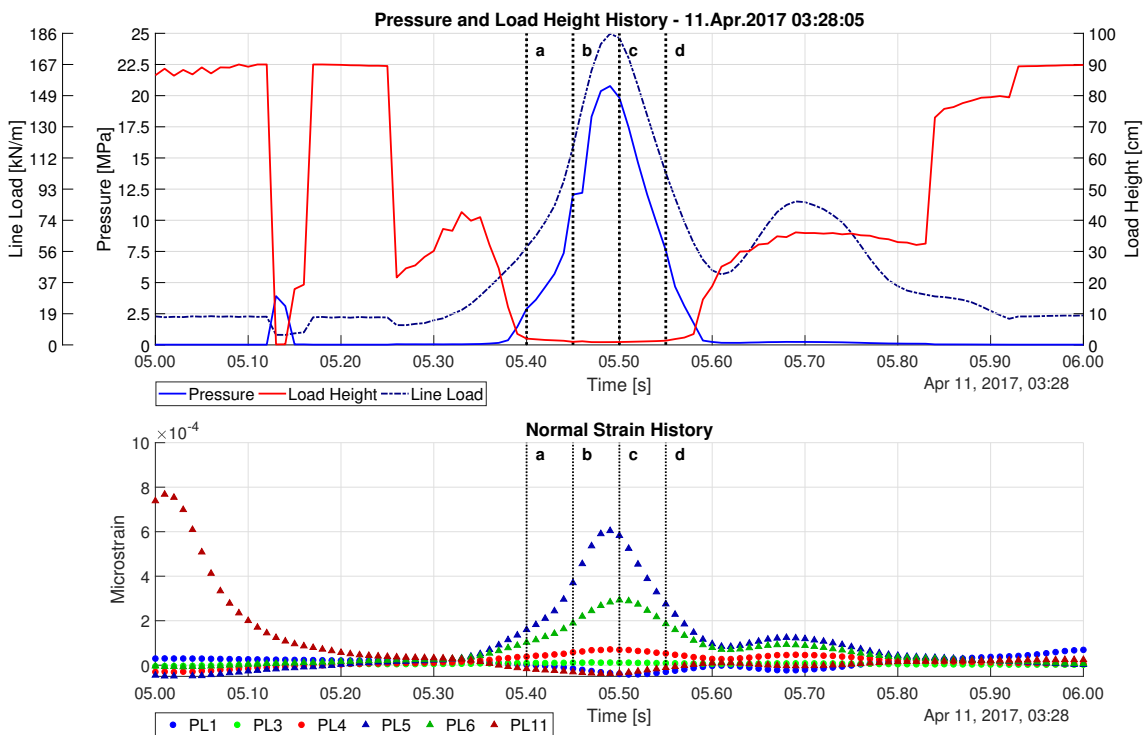


Figure A2.26: Relevant time histories for Loading Event 71

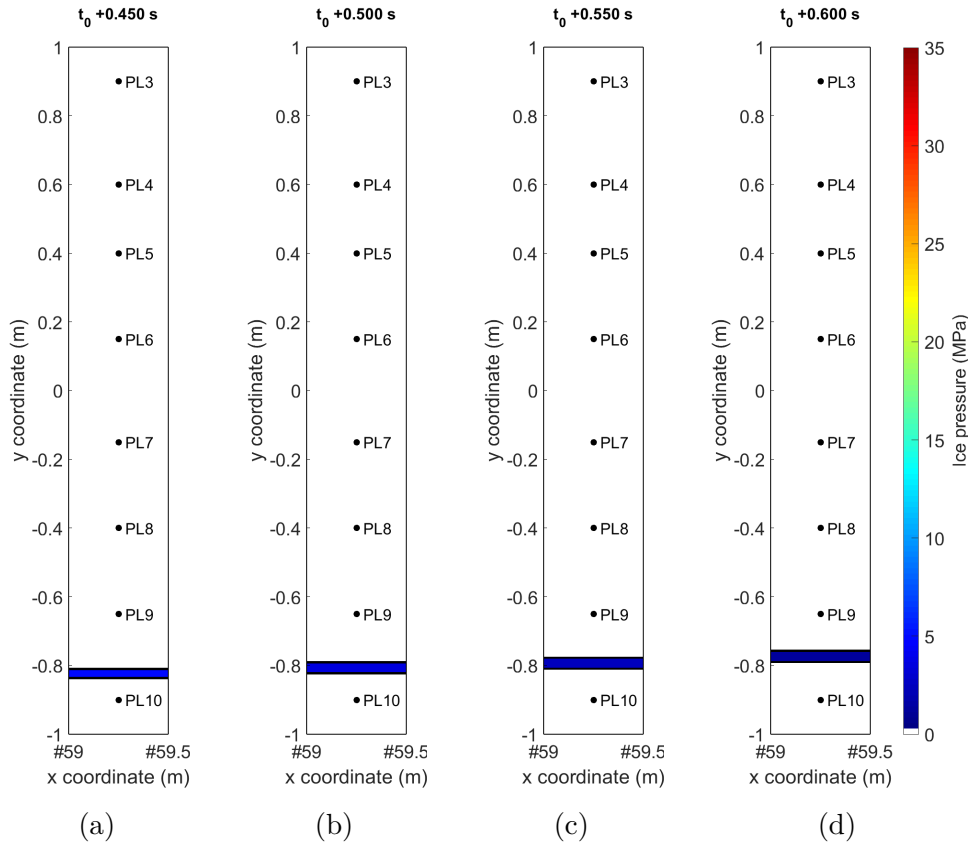


Figure A2.27: Sample load patches for Loading Event 79

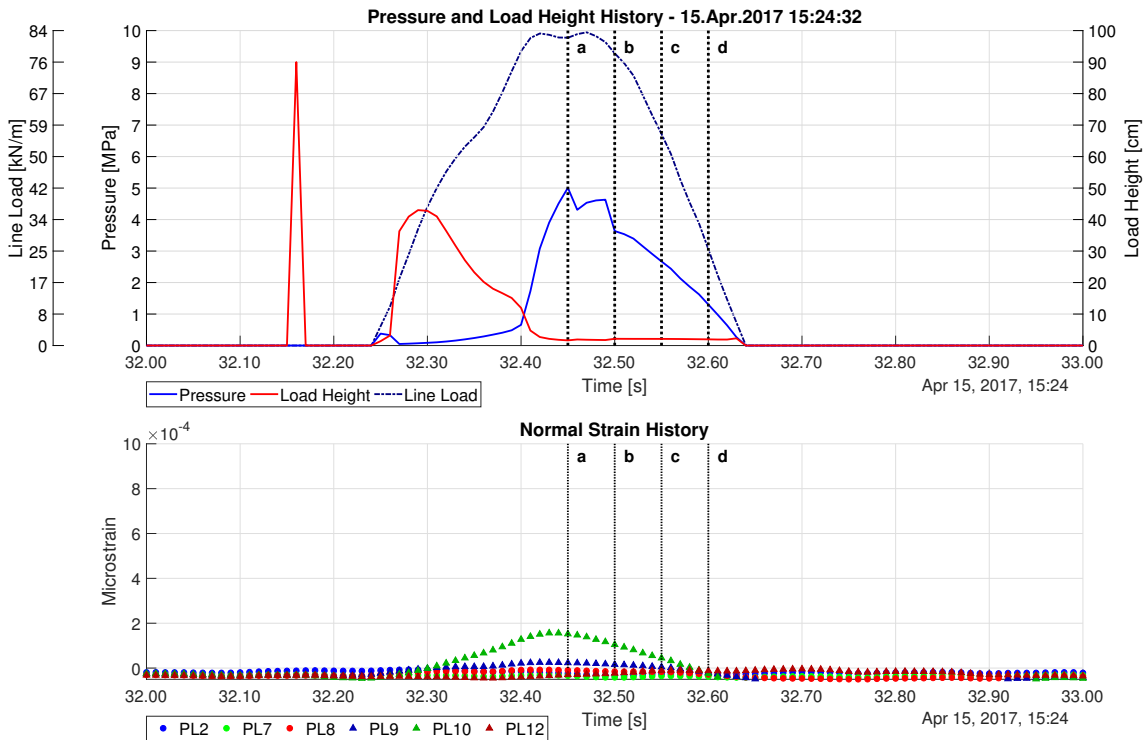


Figure A2.28: Relevant time histories for Loading Event 79

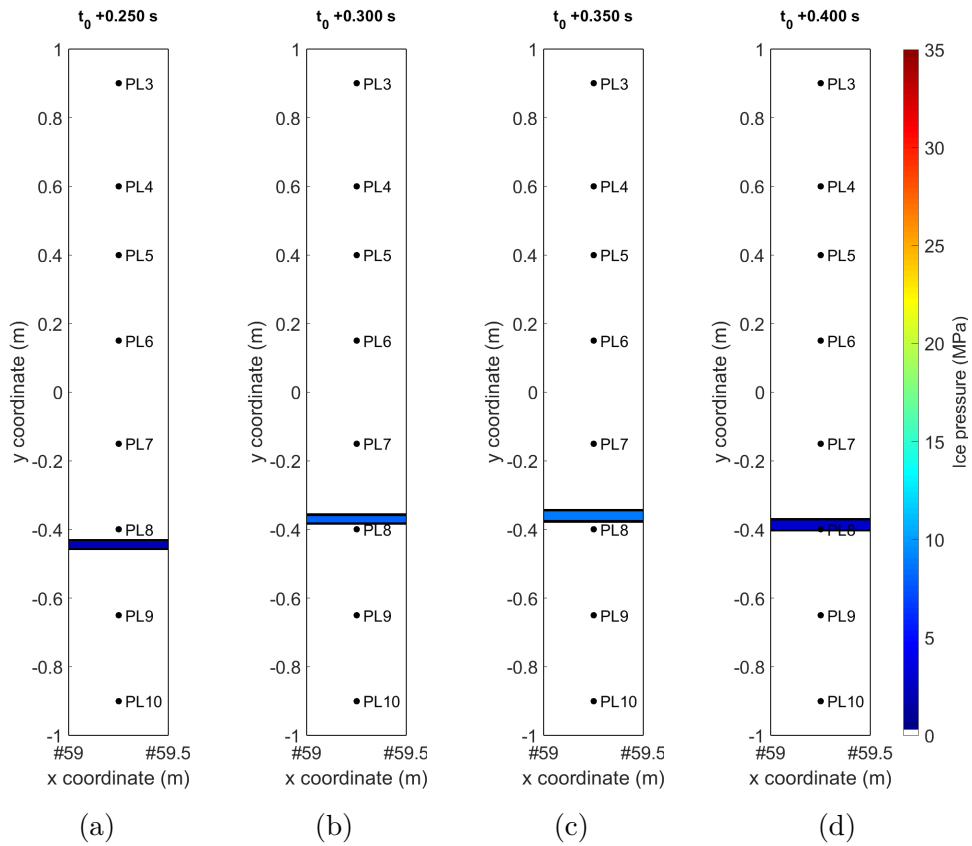


Figure A2.29: Sample load patches for Loading Event 80

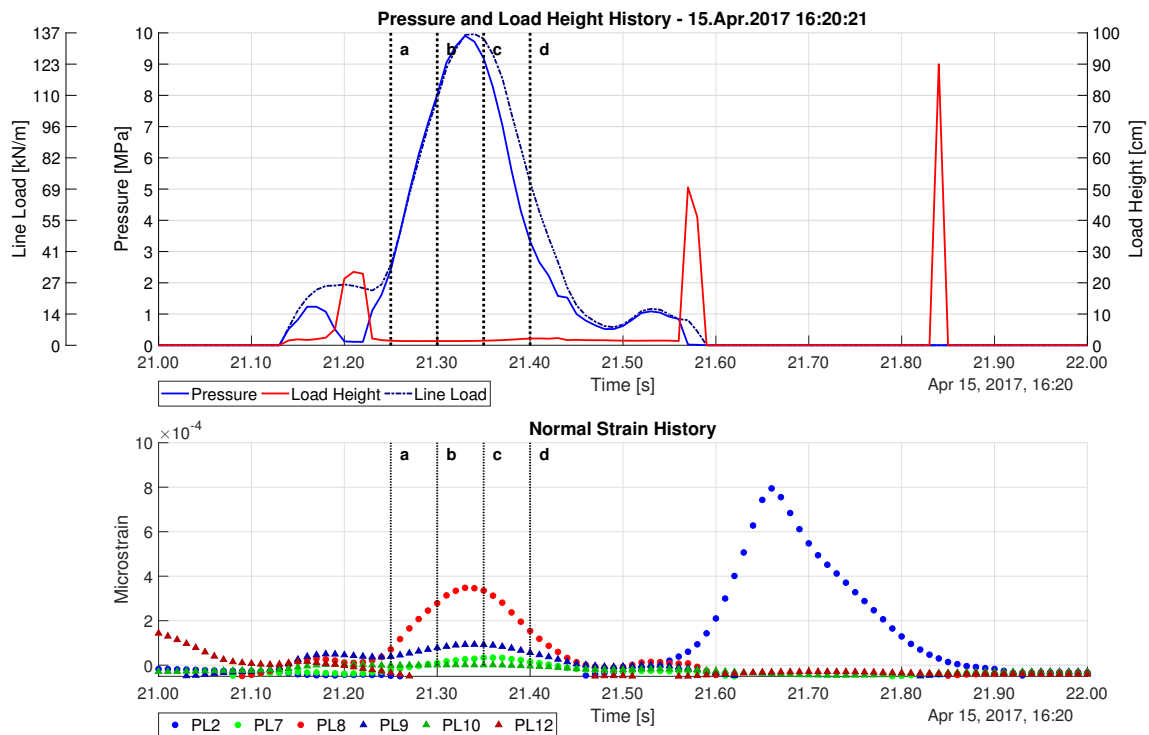


Figure A2.30: Relevant time histories for Loading Event 80

Appendix 3: Additional Line Load Comparisons

List of Figures in Appendix 3

| | |
|--|-----|
| Figure A3.1: Line load estimation comparison for Event 5 | II |
| Figure A3.2: Line load estimation comparison for Event 14 | II |
| Figure A3.3: Line load estimation comparison for Event 19 | II |
| Figure A3.4: Line load estimation comparison for Event 23 | III |
| Figure A3.5: Line load estimation comparison for Event 26 | III |
| Figure A3.6: Line load estimation comparison for Event 28 | III |
| Figure A3.7: Line load estimation comparison for Event 38 | IV |
| Figure A3.8: Line load estimation comparison for Event 40 | IV |
| Figure A3.9: Line load estimation comparison for Event 46 | IV |
| Figure A3.10: Line load estimation comparison for Event 51 | V |
| Figure A3.11: Line load estimation comparison for Event 64 | V |
| Figure A3.12: Line load estimation comparison for Event 69 | V |
| Figure A3.13: Line load estimation comparison for Event 71 | VI |
| Figure A3.14: Line load estimation comparison for Event 79 | VI |
| Figure A3.15: Line load estimation comparison for Event 80 | VI |

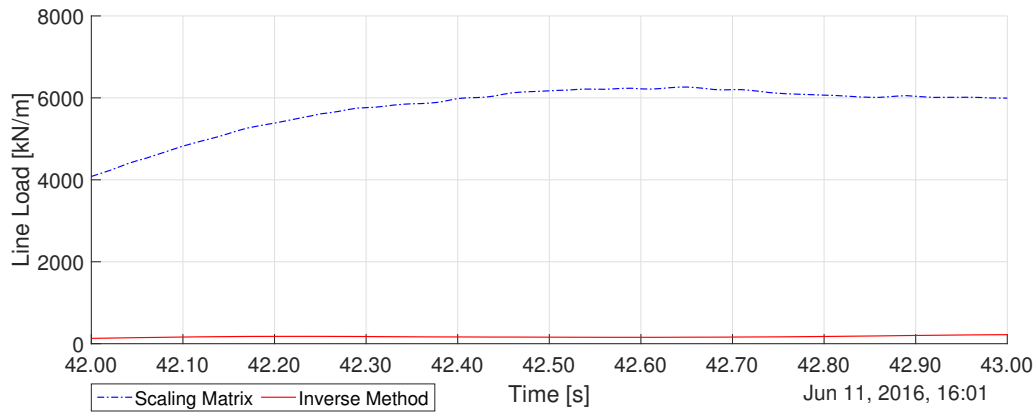


Figure A3.1: Line load estimation comparison for Event 5



Figure A3.2: Line load estimation comparison for Event 14

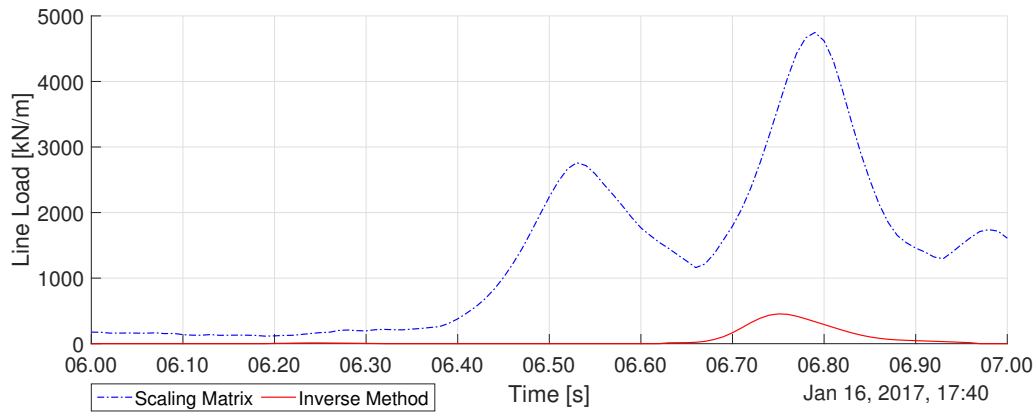


Figure A3.3: Line load estimation comparison for Event 19

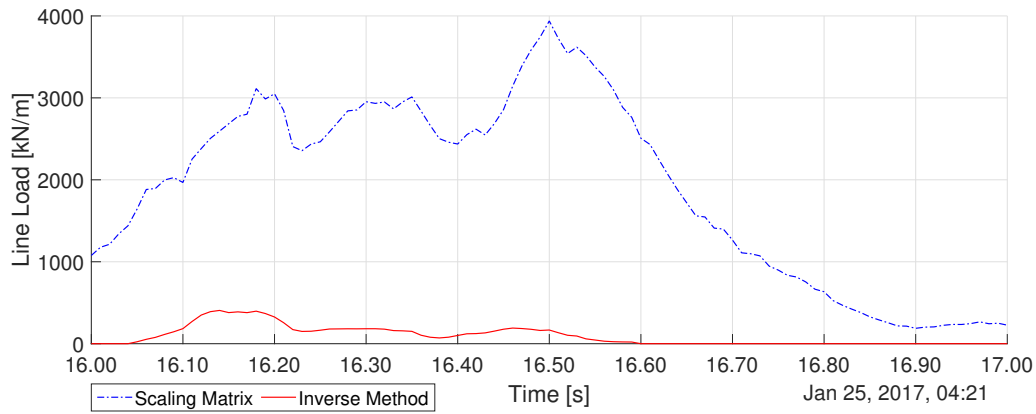


Figure A3.4: Line load estimation comparison for Event 23

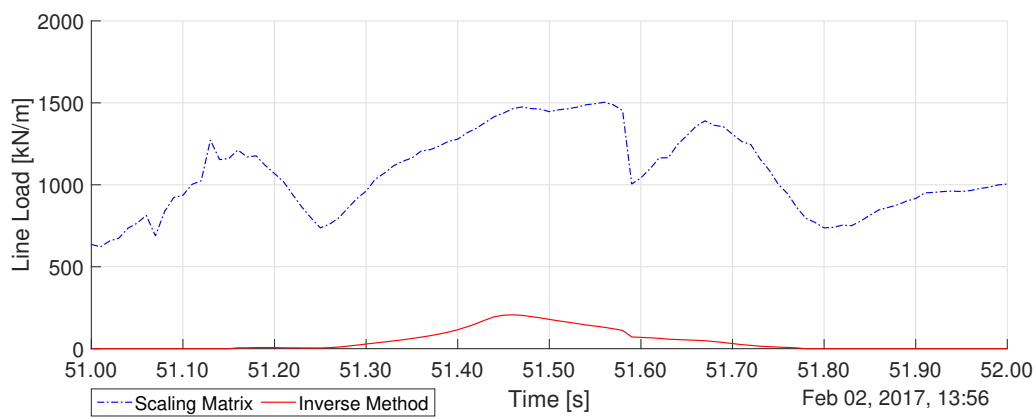


Figure A3.5: Line load estimation comparison for Event 26

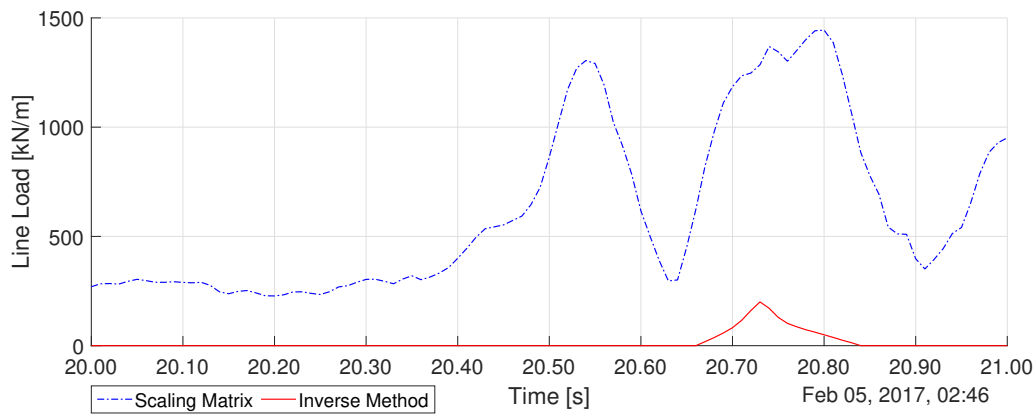


Figure A3.6: Line load estimation comparison for Event 28

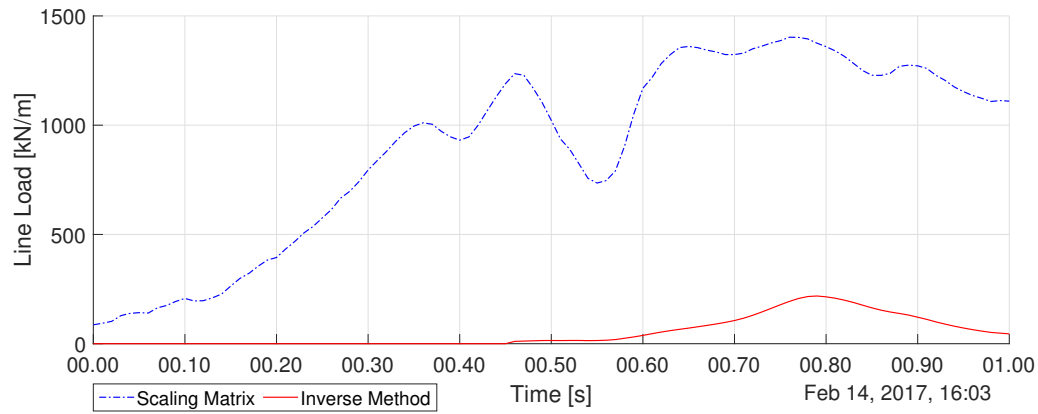


Figure A3.7: Line load estimation comparison for Event 38

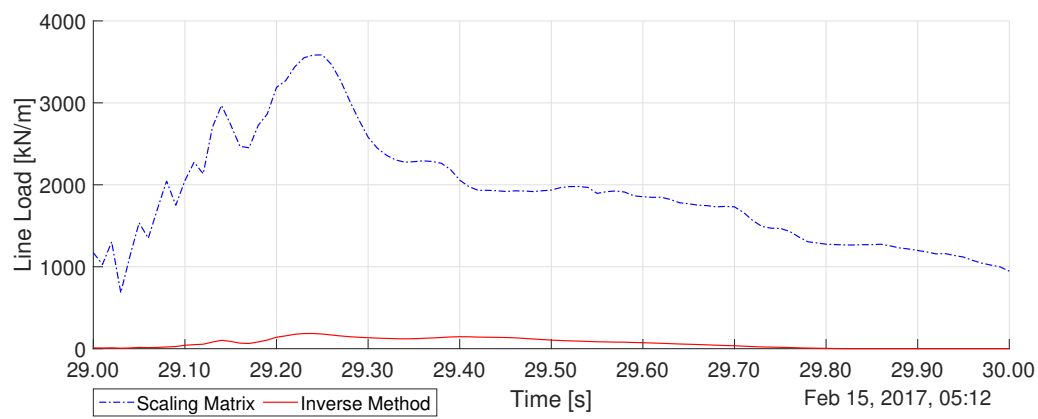


Figure A3.8: Line load estimation comparison for Event 40

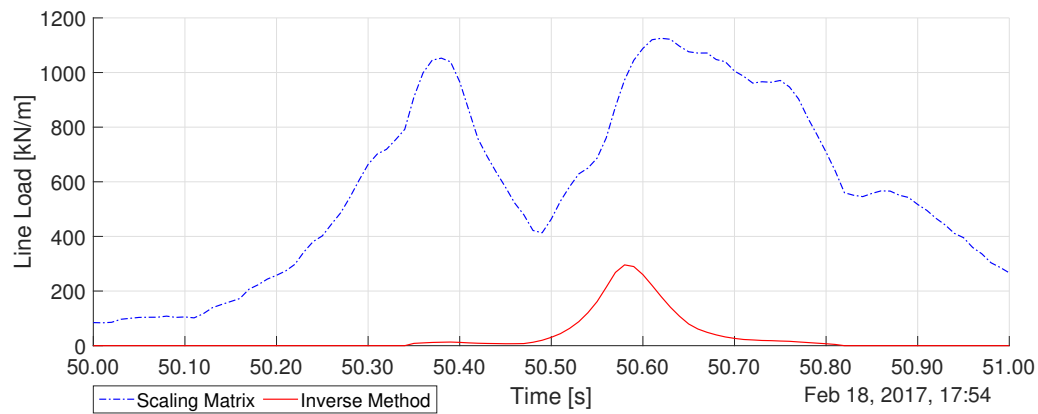


Figure A3.9: Line load estimation comparison for Event 46

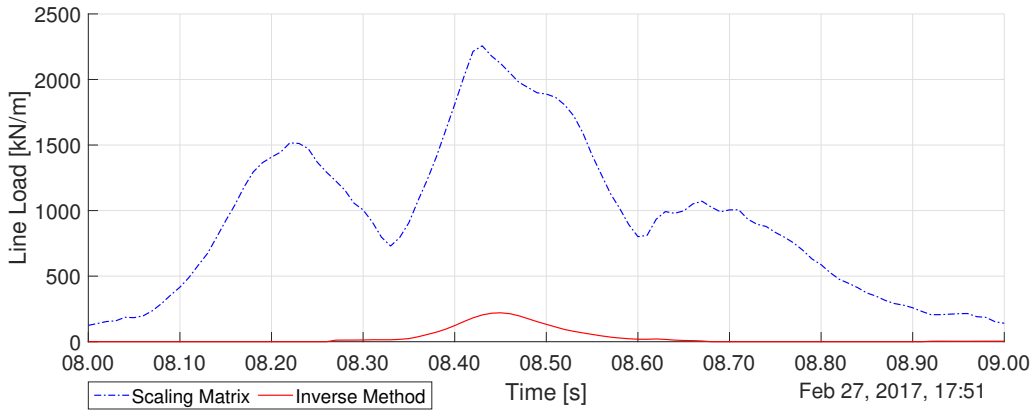


Figure A3.10: Line load estimation comparison for Event 51

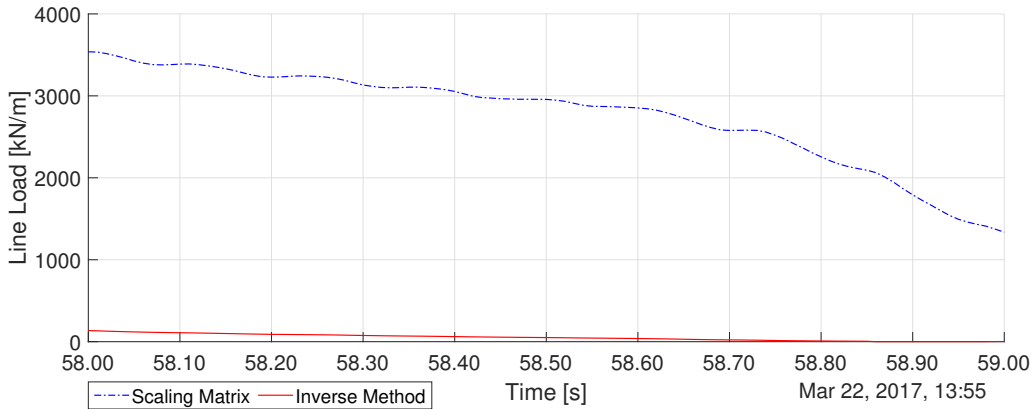


Figure A3.11: Line load estimation comparison for Event 64

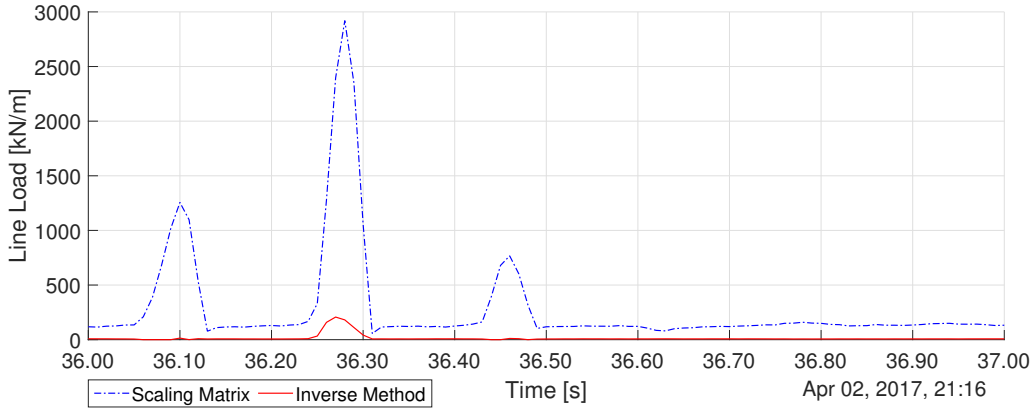


Figure A3.12: Line load estimation comparison for Event 69

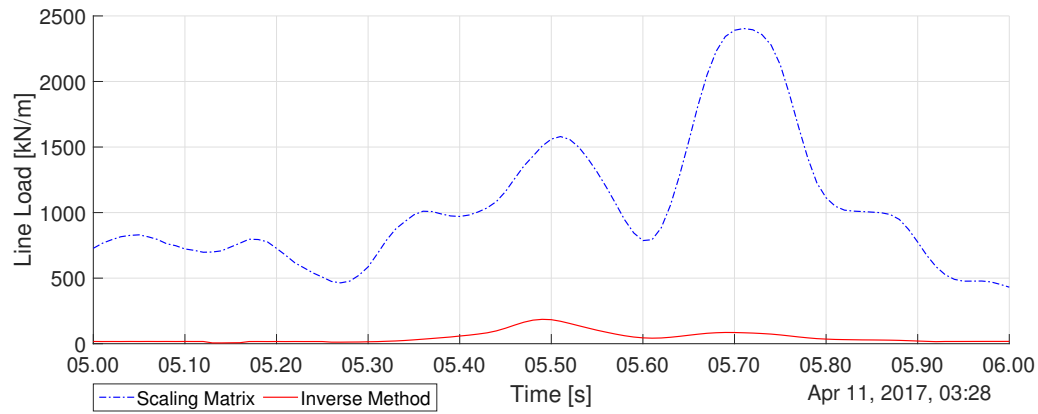


Figure A3.13: Line load estimation comparison for Event 71

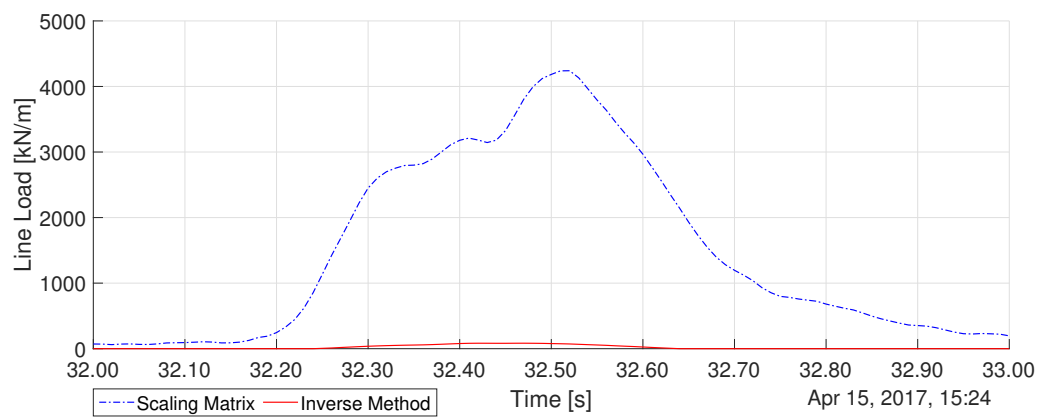


Figure A3.14: Line load estimation comparison for Event 79

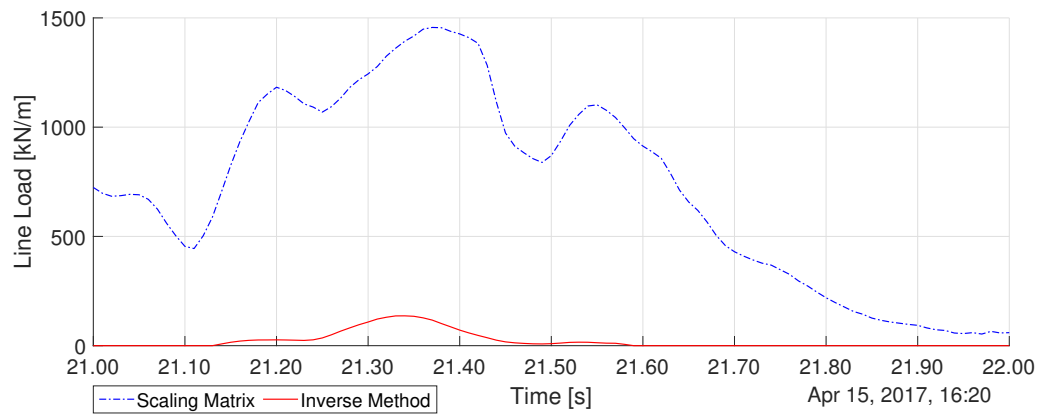


Figure A3.15: Line load estimation comparison for Event 80